# Experimental and Numerical Study of Mode II Delamination in Laminated Composite Beams

Anne Magnus

A thesis
submitted in partial fulfillment of the
requirements for the degree of

Master of Science in Civil Engineering

University of Washington

2019

Reading Committee:

Richard Wiebe, Chair

Paolo Calvi

Michael Motley

Program Authorized to Offer Degree:
Department of Civil and Environmental Engineering

University of Washington

## Abstract

## Experimental and Numerical Study of Mode II Delamination in Laminated Composite Beams

Anne Magnus

Chair of the Supervisory Committee:
Assistant Professor Richard Wiebe
Department of Civil and Environmental Engineering

The use of laminated composites is becoming increasingly ubiquitous in many industries as this material has a high strength-to-weight ratio, and offers customization and flexibility in design. However, delamination damage, which reduces the strength and stiffness of the material, is common and often difficult to detect during inspection. The integration of delamination failure considerations into the design and analysis process is of the utmost importance, and therefore necessitates experimental characterization of delamination, as well as structural-scale numerical models which accurately predict delamination behavior.

In this thesis the end loaded split (ELS) specimen was used to experimentally investigate mode II delamination, which is less well understood than mode I delamination. Force-displacement data was used to characterize the mode II critical strain energy release rate, as well as to study the capabilities of two crack growth models: the virtual crack closure technique (VCCT), and cohesive zone model (CZM). The numerical model results demonstrated good agreement with the experimental test data, however neither the experimentally determined mode II critical strain energy release rates, nor the crack growth simulations were free of size effects. In an effort to establish a more robust material model to characterize mode II delamination, through-thickness displacement field data was analyzed, but was found to lack the resolution necessary to accurately capture cracked, or even uncracked beam behavior.

# TABLE OF CONTENTS

Page

# LIST OF FIGURES

Figure Number Page

# LIST OF TABLES

Table Number Page

# LIST OF SYMBOLS

Unless explicitly stated otherwise, the following symbol definitions apply for the purposes of this thesis.

| | |
|---|---|
| $a$ | Delamination length; distance between the load application point and the tip of the crack (ELS); distance between a support roller and the tip of the crack (ENF) |
| $a_0$ | Delamination length at the beginning of a fracture test |
| $A$ | $y$-intercept of the linear $C$ vs. $a^3$ plot |
| $B$ | Width of the specimen |
| $C$ | Compliance (inverse of stiffness) of the specimen |
| $E$ | Elastic modulus |
| $E_1$ | Elastic modulus in the specimen local 1-direction; determined from the uncracked cantilever beam test (ELS); determined from the uncracked three-point bending test (ENF) |
| $G_{IIC}$ | Critical energy release rate for mode II delamination |
| $h$ | Thickness of each sublaminate for a specimen, total specimen thickness is $2h$ |
| $I$ | Moment of inertia ($Bh^3/12$) |
| $L$ | Free length of the specimen; distance between the load application point and the clamped end (ELS); distance between a support roller and the load application point (ENF) |

|  |  |
|---|---|
| $m$ | Slope of the linear $C$ vs. $a^3$ plot |
| $P$ | Force at the load application point for a specimen |
| $P_{max}$ | Maximum force during a fracture test |

# ACKNOWLEDGMENTS

I would like to extend my most sincere expression of gratitude to everyone who made the completion of this thesis possible. First and foremost, I must thank my advisor, committee chair, and professor Dr. Richard Wiebe. The guidance you've provided me throughout my research, the unwavering patience and support that you've shown toward me, and your infectious energy and passion for engineering are invaluable.

I would like to thank Han-Gyu Kim for his tremendous support of my work on this thesis. I truly appreciate all of your help and advice, especially in regard to the experimental testing portion of my research. I would also like to extend my thanks to Miguel González Montijo, Bill Kuykendall, Alec Yeutter, and Phil Yu for their assistance with my experimental testing, and Tom Lin for his support with my numerical modeling. I would like to recognize my professors Dr. Michael Motley, Dr. Paolo Calvi, Dr. Peter Mackenzie-Helnwein, and Dr. Jinkyu Yang for their fantastic instruction which provided a strong foundation for my research.

To my classmates and friends Sarah Bergquist, Gloria de Zamacona, Andrew Yang, Mitchell Gordon, and Kelsey Martin — I would not have gotten through this program without you. To my dear friends Isha Naidu, Cayla Moritz, Erin Harper, Kim Kyanka, Claire Nulty, and Hridaya Rao — I would not get through life without you. I must also thank my office mates (past and present) and friends Alec Yeutter, Jakob Sumearll, and Tasha Tardieu for the excellent company and for keeping me sane. Thank you to my brother John Magnus, and to my parents — I owe you everything.

# Chapter 1

# INTRODUCTION

## *1.1 Motivation and Objectives*

Delamination in laminated composites is a form of damage in which separation of adjacent layers causes a loss of stiffness and strength. Delamination may easily escape detection since this form of damage is often embedded within the composite structure and is not visible from the surface [Tay, 2003]. Furthermore, laminated composites have seen increased usage in many industries, and therefore understanding delamination behavior, and integrating delamination failure considerations into the laminated composite design and analysis process is of the utmost importance. Specifically, mode II delamination (the in-plane shearing mode) is the focus of this thesis as its behavior is less well understood compared to mode I delamination (the opening mode). Mode II delamination is also a common form of damage in thin plates and beams, which are frequently used in aerospace structures.

An investigation of mode II delamination in unidirectional composite beams was undertaken for this thesis through the use of a cantilever beam with a mid-plane crack, called the end loaded split (ELS) specimen. This thesis seeks to characterize mode II delamination behavior, and establish mode II fracture material parameters through experimental testing of ELS specimens of three different geometries. To integrate mode II delamination failure considerations into the structural design and analysis process, there is a need for structural-scale numerical models which accurately represent this delamination behavior. Therefore, two crack growth models were investigated: (1) the virtual crack closure technique (VCCT), and (2) cohesive zone model (CZM). This thesis is organized such that relevant background information is presented first, then the experimental tests and numerical models are described, and finally the experimental test and numerical model results are presented and compared, and the significance of the analysis findings is discussed.

This chapter provides information relevant to establishing a baseline understanding of laminated composites and their uses, as well as laminated composite mechanics and failure mechanisms. A definition for laminated composite materials as it pertains to the scope of this thesis is provided, and the advantages that this material offers, to which it owes its increasingly ubiquitous usage, are briefly discussed. An overview of classical laminate theory (CLT) is provided, along with a discussion on how the theory is used to analyze laminated composite plates. Other failure mechanisms in laminated composites are introduced, but the focus of this chapter is on discussing important and relevant fracture mechanics theories which are used to analyze delamination.

Chapter 2 discusses the ELS specimen selection, and describes the experimental testing methodology. This includes providing the specimen fabrication process, and a description of the testing equipment, setup, and procedure. Chapter 3 provides a theoretical overview of the two crack growth models, and describes how each numerical model was created using Abaqus software. The experimental test and numerical model results are then discussed over the course of Chapters 4, 5, and 6. Chapter 4 describes the determination of mechanical and fracture material properties, which are used as inputs for the numerical models. This includes an analysis of the experimental force-displacement data for determining specific material parameters. Chapter 5 provides the numerical model force-displacement results, and comparisons with the experimental test data are discussed in regard to each of the two crack growth model capabilities. Finally, Chapter 6 discusses the analysis of the through-thickness displacement field data, and the applicability of these results for characterizing mode II delamination behavior.

## *1.2 Introduction to Composites*

A composite is defined as a combination of two or more different materials with distinct interfaces to achieve desirable properties not possessed by any of the components acting alone [Yang, 2018]. For example, in the context of civil structures, composite materials include wood, concrete, and steel reinforced concrete, among others. This thesis details the investigation of laminated matrix-fiber composites, which are occasionally used in civil engineering, however the focus is on thin composite beams and plates which are more common in aerospace structures.

Laminated composites are composed of a fiber embedded in a matrix. Fibers are typically strong and stiff, but brittle, while the matrix is typically weak and soft, but with a large failure strain. Types of fiber include graphite, glass, Kevlar, and boron; while types of matrix include epoxy, polyester, metals, and ceramics. The resulting composite material has superior mechanical properties to either the fiber or the matrix acting alone. As it pertains to this thesis, a lamina is defined as a single ply or layer of the composite material where the fibers are all oriented in one direction, and a laminate is composed of multiple plies stacked on top of one another. While matrix-fiber composites do not require this layering, it streamlines manufacturing, and various orientation angles in the stacking sequence can permit tailoring to meet certain design requirements. This layering and angling of plies is illustrated schematically in Figure 1.1. The laminated composites used in this thesis are all unidirectional laminates (unidirectional lamina laid up at identical orientation angles).

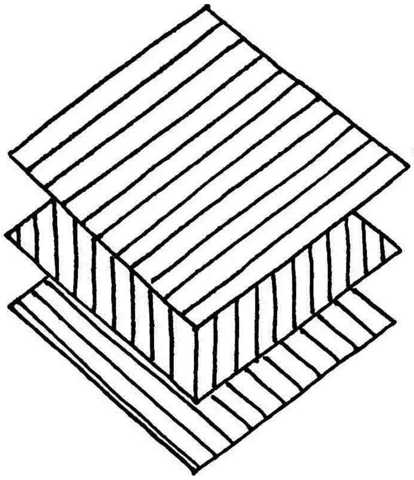

Figure 1.1: Laminated composite layup with various ply orientation angles

However, not all laminated composites are composed of plies with distinct and uniform fiber orientation angles; other types of composites include woven fabric, particulate, braided, stitched, and chopped fiber composites, to name a few [Yang, 2018].

Composites offer several advantages over other materials including good fatigue and corrosion resistance, and lighter weight. Design benefits include greater flexibility in design, and allowing for larger, more integrated designs. Production and manufacturing benefits include fewer parts, quicker assembly, and reduction of production flow time. Owing to these benefits, laminated composites have seen increased usage in the aerospace, wind, oil and gas, automotive, marine, and sporting goods sectors, among others [Yang, 2018]. This increased use of composites has resulted in a growing demand for engineers versed in the design of structures made of fiber-reinforced composite materials [Kollar and Springer, 2003].

### *1.3 Classical Laminate Theory*

Prior to investigating how delamination causes failure in composites, the behavior of undamaged composites must first be understood. This section introduces classical laminate theory, which provides tools for the analysis of composite plates. CLT relates in-plane forces and bending moments to in-plane strains and curvatures through a laminate stiffness matrix called the ABD matrix. This relationship is

$$\begin{Bmatrix} \mathbf{N} \\ \mathbf{M} \end{Bmatrix} = \begin{bmatrix} \mathbf{A} & \mathbf{B} \\ \mathbf{B} & \mathbf{D} \end{bmatrix} \begin{Bmatrix} \boldsymbol{\varepsilon}^{\mathbf{0}} \\ \boldsymbol{\kappa} \end{Bmatrix} \quad \rightarrow \quad \begin{Bmatrix} N_x \\ N_y \\ N_{xy} \\ M_x \\ M_y \\ M_{xy} \end{Bmatrix} = \begin{bmatrix} A_{11} & A_{12} & A_{16} & B_{11} & B_{12} & B_{16} \\ A_{12} & A_{22} & A_{26} & B_{12} & B_{22} & B_{26} \\ A_{16} & A_{26} & A_{66} & B_{16} & B_{26} & B_{66} \\ B_{11} & B_{12} & B_{16} & D_{11} & D_{12} & D_{16} \\ B_{12} & B_{22} & B_{26} & D_{12} & D_{22} & D_{26} \\ B_{16} & B_{26} & B_{66} & D_{16} & D_{26} & D_{66} \end{bmatrix} \begin{Bmatrix} \varepsilon_x^0 \\ \varepsilon_y^0 \\ \gamma_{xy}^0 \\ \kappa_x \\ \kappa_y \\ \kappa_{xy} \end{Bmatrix}$$

where **N** and **M** are the in-plane forces and moments, **A** is the extensional stiffness, **B** is the in-plane, out-of-plane coupling stiffness, **D** is the bending stiffness, and $\boldsymbol{\varepsilon}^{\mathbf{0}}$ and $\boldsymbol{\kappa}$ are the mid-plane strains and curvatures [Kollar and Springer, 2003]. **A**, **B**, and **D** are defined as

$$\left[\,\mathbf{A}\,\right] = \int_{-h_b}^{h_t} \left[\,\overline{\mathbf{Q}}\,\right] dz,$$

$$\left[\,\mathbf{B}\,\right] = \int_{-h_b}^{h_t} z \left[\,\overline{\mathbf{Q}}\,\right] dz,$$

$$\left[\,\mathbf{D}\,\right] = \int_{-h_b}^{h_t} z^2 \left[\,\overline{\mathbf{Q}}\,\right] dz$$

where $h_b$ and $h_t$ are the distance from the laminate reference plane (mid-plane) to the bottom and the top of the laminate, respectively [Kollar and Springer, 2003]. The ABD matrix accounts for both the orientation angles and stacking sequence of the laminate.

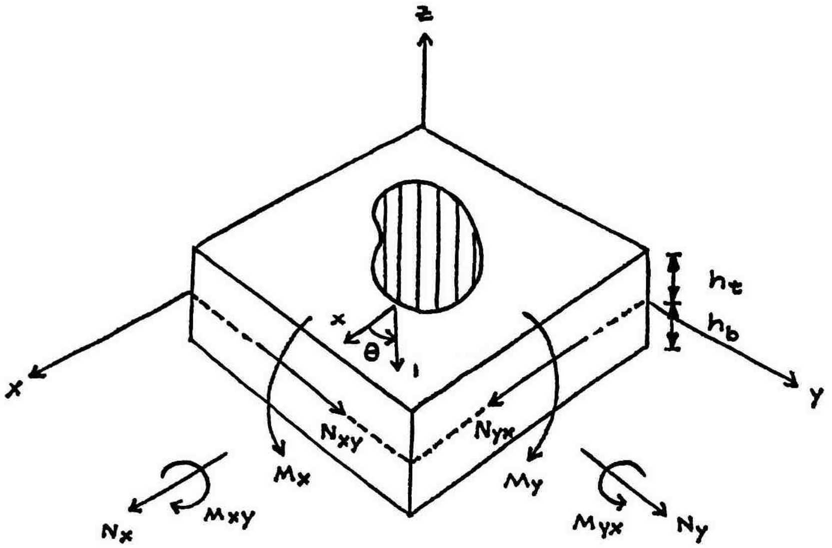

Figure 1.2: Laminate subjected to in-plane forces and moments

The ply stiffness matrix in global coordinates $\overline{\mathbf{Q}}$ is related to the ply stiffness matrix in local coordinates $\mathbf{Q}$ through the ply orientation angle. The relationship between $\mathbf{Q}$ and $\overline{\mathbf{Q}}$ is

$$\begin{bmatrix} \overline{Q}_{11} & \overline{Q}_{12} & \overline{Q}_{16} \\ \overline{Q}_{12} & \overline{Q}_{22} & \overline{Q}_{26} \\ \overline{Q}_{16} & \overline{Q}_{26} & \overline{Q}_{66} \end{bmatrix} = \begin{bmatrix} c^2 & s^2 & 2cs \\ s^2 & c^2 & -2cs \\ -cs & cs & c^2-s^2 \end{bmatrix}^{-1} \begin{bmatrix} Q_{11} & Q_{12} & Q_{16} \\ Q_{12} & Q_{22} & Q_{26} \\ Q_{16} & Q_{26} & Q_{66} \end{bmatrix} \begin{bmatrix} c^2 & s^2 & cs \\ s^2 & c^2 & -cs \\ -2cs & 2cs & c^2-s^2 \end{bmatrix}$$

where $c = \cos\theta$, $s = \sin\theta$, and $\theta$ is the ply orientation angle defined as the angle from the global $x$-axis to the local 1-axis, as illustrated in Figure 1.2 [Kollar and Springer, 2003]. For an orthotropic material

$$\begin{bmatrix} Q_{11} & Q_{12} & Q_{16} \\ Q_{12} & Q_{22} & Q_{26} \\ Q_{16} & Q_{26} & Q_{66} \end{bmatrix} = \begin{bmatrix} \frac{E_1}{D} & \frac{\nu_{12}E_2}{D} & 0 \\ \frac{\nu_{12}E_2}{D} & \frac{E_2}{D} & 0 \\ 0 & 0 & G_{12} \end{bmatrix} \quad \text{where} \quad D = 1 - \frac{E_2}{E_1}\nu_{12}^2 .$$

Observing the definitions for the ABD matrix and $\mathbf{Q}$, a unidirectional laminate composed of multiple identical lamina may be treated as a single ply whose total thickness is the thickness of the entire laminate.

The through-thickness strain and stress distributions for the laminate may also be obtained from

$$\left\{ \boldsymbol{\varepsilon} \right\} = \left\{ \boldsymbol{\varepsilon^0} \right\} + z \left\{ \boldsymbol{\kappa} \right\} \quad \rightarrow \quad \begin{Bmatrix} \varepsilon_x \\ \varepsilon_y \\ \gamma_{xy} \end{Bmatrix} = \begin{Bmatrix} \varepsilon_x^0 \\ \varepsilon_y^0 \\ \gamma_{xy}^0 \end{Bmatrix} + z \begin{Bmatrix} \kappa_x \\ \kappa_y \\ \kappa_{xy} \end{Bmatrix},$$

$$\left\{ \boldsymbol{\sigma} \right\} = \left[ \overline{\mathbf{Q}} \right] \left\{ \boldsymbol{\varepsilon} \right\} \quad \rightarrow \quad \begin{Bmatrix} \sigma_x \\ \sigma_y \\ \tau_{xy} \end{Bmatrix} = \begin{bmatrix} \overline{Q}_{11} & \overline{Q}_{12} & \overline{Q}_{16} \\ \overline{Q}_{12} & \overline{Q}_{22} & \overline{Q}_{26} \\ \overline{Q}_{16} & \overline{Q}_{26} & \overline{Q}_{66} \end{bmatrix} \begin{Bmatrix} \varepsilon_x \\ \varepsilon_y \\ \gamma_{xy} \end{Bmatrix}.$$

Classical laminate theory uses the Kirchhoff-Love plate theory, a generalization of Euler-Bernoulli beam theory, which is based on several limiting assumptions including a linear elastic material response, the plane stress condition in the thickness direction, and perfect bonding between plies, however, these are all reasonable assumptions for thin composite plates, except near delaminations.

## *1.4 Composite Failure Overview*

Composite failure may be caused by fiber buckling, fiber breaking, matrix cracking, delamination, or by a combination of these factors [Kollar and Springer, 2003]. When fiber buckling occurs, the surrounding matrix supports the fibers, but the compressive stiffness and strength of the laminate are reduced. During fiber breaking, the load is transmitted around the failed fiber by the surrounding matrix which acts as a bridge around the break, and hence this phenomenon is called fiber bridging. Matrix cracking facilitates moisture absorption into the composite, reduces the matrix-dominated stiffness (load carrying capability orthogonal to the fiber orientation) of the laminate, and may propagate into the interface between adjacent plies and lead to delamination.

Delamination is a common failure mode in laminated composites, and is the focus of this thesis. Delamination is a separation of adjacent layers that may be introduced either during manufacturing, or subsequently by loads applied to the laminate. Delamination reduces the bending stiffness and strength of the laminate, as well as the load carrying capability under compression. Under loading, the delamination may reach a critical size at which the growth of the delamination becomes unstable, leading to a rapid loss in strength [Kollar and Springer, 2003]. There are three modes of delamination: (1) mode I, the opening mode, (2) mode II, the shearing mode, and (3) mode III, the tearing mode. These modes are illustrated in Figure 1.3.

Commonly, ply stress-based failure theories are used to analyze composite failure, where failure is taken to occur when any one of the plies fails (first-ply failure). First-ply failure theories include quadratic (this criteria and some of its forms are variously referred to as Tsai-Wu and Tsai-Hill), maximum stress, and maximum strain failure criteria [Kollar and Springer, 2003]. The definitions for these criteria are provided below for orthotropic and transversely isotropic materials under the plane stress condition. The quadratic failure

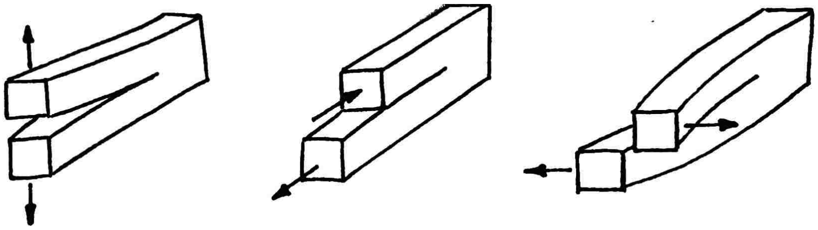

Figure 1.3: Three delamination modes: mode I (left), mode II (center), and mode III (right)

criteria is

$$F_1\sigma_1 + F_2\sigma_2 + F_{11}\sigma_1^2 + F_{22}\sigma_2^2 + F_{66}\tau_{12}^2 + 2F_{12}\sigma_1\sigma_2 < 1$$

where

$$\begin{aligned} F_1 &= \frac{1}{s_1^+} - \frac{1}{s_1^-}, & F_2 &= \frac{1}{s_2^+} - \frac{1}{s_2^-}, \\ F_{11} &= \frac{1}{s_1^+ s_1^-}, & F_{22} &= \frac{1}{s_2^+ s_2^-}, \\ & & F_{66} = \frac{1}{(s_{12})^2}. \end{aligned}$$

The maximum stress failure criteria is

$$-s_1^- < \sigma_1 < s_1^+, \qquad -s_2^- < \sigma_2 < s_2^+, \qquad |\tau_{12}| < s_{12}.$$

The maximum strain failure criteria is

$$-\eta_1^- < \varepsilon_1 < \eta_1^+, \qquad -\eta_2^- < \varepsilon_2 < \eta_2^+, \qquad |\gamma_{12}| < \eta_{12}.$$

The $s_i^+$ and $s_i^-$ are the tensile and compressive strengths in the $i$-direction, and $s_{ij}$ are the shear strengths in the $ij$-planes. Likewise, the $\eta_i^+$ and $\eta_i^-$ are the allowable tensile and compressive strains in the $i$-direction, and $\eta_{ij}$ are the allowable shear strains in the $ij$-planes.

Classical laminate theory allows for implementation of first-ply failure theories in the design process, but the assumption of perfect bonding between plies is limiting in that CLT alone is not sufficient for analyzing delamination in plates. Ideally, mechanism-based failure theories, which are more representative of real failure, would be considered during design. Therefore, to extend composite failure considerations to delamination, an introduction of fracture mechanics theories is necessary.

## ***1.5 Fracture Mechanics***

The fracture behavior investigated for this thesis is characterized primarily by a material property called the critical strain energy release rate $G_C$. Subsequent chapters will discuss how this material property is determined from the experimental test data, and how this material property is used in the numerical models. However, the theory used to establish a definition for the strain energy release rate is not the only avenue through which to characterize fracture, and therefore this section introduces several other important fracture mechanics theories and quantities including the stress intensity factor $K$, and the J-integral $J$. This section also discusses how these properties are related, and the other insights these theories provide, including crack growth stability and plastic zone size considerations.

Due to the scope of this thesis, the discussion of concepts in this section is limited to information relevant to establishing a baseline understanding of fracture mechanics for the purpose of the ELS specimen. This includes an effort to limit the discussion to mode II fracture with the assumptions of plane stress and linear elasticity. Certain derivations are presented for mode I fracture, but in such cases similar logic is used to develop the theory for mode II. Isotropy and material homogeneity are invariable assumptions throughout this section, but the concepts can be extended to transversely isotropic composite materials.

### *1.5.1 Strain Energy Release Rate (G)*

The strain energy release rate $G$ represents the energy released as a result of crack extension per unit of newly created crack surface. The critical strain energy release rate $G_C$ is considered to be a material property, as well as a fracture initiation criterion such that a crack will propagate when $G \geq G_C$ [Mamidala, 2018]. As mentioned previously, $G_{IIC}$ is the material property used to characterize fracture for this thesis, and is determined for the ELS specimen using

$$G_{II} = \frac{9P^2a^2}{4EB^2h^3} \tag{1.1}$$

(see Chapter 2 for a description of the ELS specimen). Chapters 4 and 5 will discuss further how this material property is determined from the experimental test data, and how it is used in the numerical models. Therefore, this section focuses on providing the underlying theory for, and derivation of this quantity.

The energy release rate is found through the energy approach first presented by Griffith. Critical to Griffith's derivation is the assumption of linear elasticity. This theory states that the energy for a cracked system is

$$U = U_0 + U_s + \Gamma - U_e \tag{1.2}$$

where $U$ is the total system energy, $U_0$ is the elastic strain energy of the uncracked system, $U_s$ is the change in elastic strain energy caused by the introduction of the initial crack to the system, $\Gamma$ is the change in elastic surface strain energy caused by the formation of crack surfaces, and $U_e$ is the work performed on the system by external forces. These values are illustrated in Figure 1.4, where the energy of the top beam is described by $U_0$ and $U_e$, $U_s$ is the change in energy between the top and middle beams, and $\Gamma$ is the change in energy between the middle and bottom beams, i.e. the energy dissipated as a result of crack extension. p

Griffith identified the condition for sustained crack growth as

$$\frac{\partial U}{\partial A} \geq 0$$

where $A$ is the cracked surface area. The critical condition for the onset of crack growth is the lower bound of this relation [Sanford, 2003]

$$\frac{\partial U}{\partial A} = 0. \tag{1.3}$$

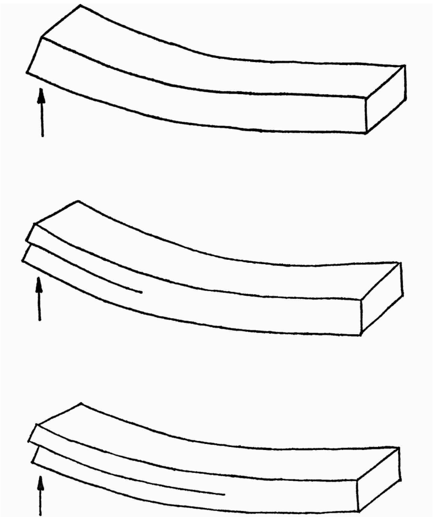

Figure 1.4: A loaded and uncracked system (top), a crack introduced to the loaded system (middle), and the crack extended for the loaded system (bottom)

Plugging equation (1.2) into equation (1.3) gives

$$\frac{\partial(U_0 + U_s + \Gamma - U_e)}{\partial(aB)} = 0.$$

$U_0$ is constant, and $B$ is assumed to be constant, giving

$$\frac{1}{B}\frac{\partial(U_s + \Gamma - U_e)}{\partial a} = 0.$$

Here, the strain energy release rate $G$ is defined such that

$$G = \frac{\partial \Gamma}{\partial A}.$$

Therefore,

$$G = \frac{\partial \Gamma}{\partial A} = \frac{1}{B}\frac{\partial(U_e - U_s)}{\partial a} = \frac{1}{B}\left(\frac{\partial U_e}{\partial a} - \frac{\partial U_s}{\partial a}\right).$$

Due to the scope of this thesis, only the mode II strain energy release rate $G_{II}$ will be derived, but $G_I$ and $G_{III}$ are obtained in a similar manner.

The energy release rate may be obtained experimentally, where in practice various methods may be used, such as force or displacement controlled loading. Consider the pure mode II ELS specimen under ***force control***. In this case

$$U_e = Pv, \qquad U_s = \frac{1}{2}Pv$$

where $P$ and $v$ are the load and the vertical displacement at the load application point, respectively, and therefore

$$G_{II} \;=\; \frac{1}{B}\frac{\partial(Pv - \frac{1}{2}Pv)}{\partial a} \;=\; \frac{P}{2B}\frac{\partial v}{\partial a}.$$

The relationship between force $P$, displacement $v$, and compliance $C$ is

$$v = CP,$$

and therefore

$$G_{II} = \frac{P}{2B}\frac{\partial (CP)}{\partial a},$$

$$G_{II} = \frac{P^2}{2B}\frac{\partial C}{\partial a}. \tag{1.4}$$

Now, consider the pure mode II ELS specimen under ***displacement control***. In this case

$$U_e = 0, \qquad U_s = \frac{1}{2}Pv,$$

and therefore

$$G_{II} \;=\; \frac{1}{B}\frac{\partial(0 - \frac{1}{2}Pv)}{\partial a} \;=\; -\frac{v}{2B}\frac{\partial P}{\partial a}. \tag{1.5}$$

Recalling the force-displacement-compliance relationship from above

$$\frac{\partial P}{\partial a} \;=\; \frac{\partial(\frac{v}{C})}{\partial a} \;=\; v\frac{\partial(C^{-1})}{\partial a} \;=\; \frac{-v}{C^2}\frac{\partial C}{\partial a}. \tag{1.6}$$

Plugging equation (1.6) into equation (1.5) gives the same result as equation (1.4).

Thus, both the force and the displacement controlled loading scenarios have the same definition for mode II strain energy release rate, as defined by equation (1.4). The compliance of the end loaded split specimen is (see Appendix A)

$$C = \frac{3a^3 + L^3}{24EI},$$

and therefore

$$\frac{\partial C}{\partial a} = \frac{3a^2}{8EI}.$$

Plugging these into equation (1.4) gives the definition for the strain energy release rate of the ELS specimen provided in equation (1.1). Note that Williams offers an alternative derivation of $G_{II}$ for the ELS specimen that does not require explicitly finding the beam's compliance; his approach is based on solving moment equilibrium about the crack tip [Williams, 1988].

### *1.5.2 Stress Intensity Factor (K)*

An alternative to the energy approach of characterizing fracture is the stress-based approach, which yields another important physical quantity called the stress intensity factor $K$. The stress at an ideally sharp crack tip in a perfectly brittle material is singular. Thus, rather than directly describing the stress field, it is useful to define a stress intensity factor $K$ to serve as a scaling factor to define the magnitude of the crack tip stress field. The critical value $K_C$ is called the fracture toughness, or the critical stress intensity factor. Fracture toughness is considered to be a material property in linear elastic fracture mechanics, and serves as a fracture initiation criterion such that a crack will propagate when $K \geq K_C$ [Sanford, 2003]. The assumption of linear elasticity in the vicinity of a crack tip is incorrect for many real materials, however the exploration of this assumption yields significant results which will be discussed.

An expression for $K$ can be derived through crack tip stress analysis. To solve two dimensional elasticity problems, the approach presented by Airy is introduced. His approach uses an auxiliary function which is biharmonic, and therefore automatically satisfies equilibrium and compatibility (see Appendix C). Furthermore, the introduction of complex functions to two dimensional elasticity ensures that the biharmonic equation is satisfied [Sanford, 2003]. Westergaard first proposed the complex stress function approach in 1939 [Westergaard, 1939]. His method is limited to straight crack problems in infinite bodies with uniform remote boundary conditions. Others have since modified his method, but nevertheless the understanding of this initial approach provides a good baseline on which to understand the definition for $K$.

To develop an expression for the stress intensity factor $K$, Westergaard proposed an Airy stress function for mode II ($\Phi_{II}$), which is related to the Westergaard stress function for mode II ($Z_{II}$) by

$$\Phi_{II} \;=\; -\,y\,\mathrm{Re}(\overline{Z}_{II}) \tag{1.7}$$

where

$$\overline{Z} = \frac{d\overline{\overline{Z}}}{dz}, \qquad Z = \frac{d\overline{Z}}{dz}, \qquad Z' = \frac{dZ}{dz},$$

and $Z$ is the Westergaard stress function specific to modes I, II, and III, and $z$ is $x+iy$. This notation is useful because although $\Phi_{II}$ is a function of $\overline{Z}$, the stress components $\sigma_x$, $\sigma_y$, and $\tau_{xy}$ are functions only of $Z$ and $Z'$, as shown later. Therefore, the definitions for $\overline{\overline{Z}}$ and $\overline{Z}$ are not necessary. The Westergaard stress function $Z$ must either be an analytic function, or it must satisfy the Cauchy-Reimann condition [Mamidala, 2018]. The Cauchy-Reimann equations are

$$\mathrm{Re}\left(\frac{dZ}{dz}\right) \;=\; \frac{\partial \mathrm{Re}(Z)}{\partial x} \;=\; \frac{\partial \mathrm{Im}(Z)}{\partial y},$$

$$\mathrm{Im}\left(\frac{dZ}{dz}\right) \;=\; \frac{\partial \mathrm{Im}(Z)}{\partial x} \;=\; -\,\frac{\partial \mathrm{Re}(Z)}{\partial y}$$

which leads to

$$\frac{dZ}{dz} \;=\; \mathrm{Re}\left(\frac{dZ}{dz}\right) \;+\; i\;\mathrm{Im}\left(\frac{dZ}{dz}\right),$$

$$
\begin{aligned}
&= \frac{\partial \mathrm{Re}(Z)}{\partial x} + i\,\frac{\partial \mathrm{Im}(Z)}{\partial x}, \\
&= \frac{\partial \mathrm{Im}(Z)}{\partial y} - i\,\frac{\partial \mathrm{Re}(Z)}{\partial y}.
\end{aligned}
$$

Due to the scope of this thesis, only the mode II derivation will be presented, but the mode I and mode III stress intensity factors are obtained in a similar fashion. Combining the Airy stress function definitions (see Appendix C) with Westergaard's mode II stress function, using the Cauchy-Reimann equations, and the definitions of $\overline{Z}$, $Z$, and $Z'$ results in the following stress definitions for mode II

$$\sigma_x = 2\,\mathrm{Im}(Z) + y\,\mathrm{Re}(Z'), \tag{1.8}$$

$$\sigma_y = -\,y\,\mathrm{Re}(Z'), \tag{1.9}$$

$$\tau_{xy} = \mathrm{Re}(Z) - y\,\mathrm{Im}(Z'). \tag{1.10}$$

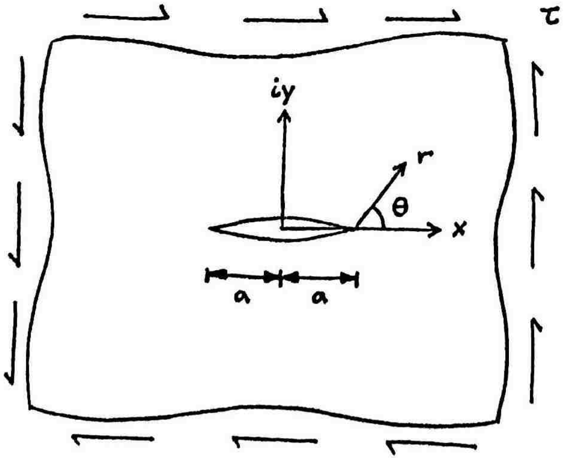

Figure 1.5: Straight, ideally sharp, through-thickness crack in an infinite structure subjected to uniform remote boundary conditions which induce stress

Consider the structure in Figure 1.5 with a crack of length $2a$ subjected to a remote fixed displacement causing the shear stress $\tau$. Critical to the development of the definition for $K_{II}$ are the assumptions that the material is homogeneous, isotropic, and linear elastic, the crack tip is ideally sharp, and the crack is through-thickness in an infinite domain. The mode II stress function $Z_{II}$ proposed by Westergaard is

$$Z_{II} = \frac{\tau z}{\sqrt{(z-a)(z+a)}}.$$

Polar coordinates are used at the crack tip such that $z$ is $a + \xi$, and $\xi$ is $re^{i\theta}$. Substitution of $a + \xi$ for $z$ gives

$$Z_{II} = \frac{\tau(\xi + a)}{\sqrt{\xi(\xi + 2a)}}. \tag{1.11}$$

Very close to the crack tip, $\xi \ll a$ and $Z_{II}$ becomes

$$Z_{II} \;=\; \frac{\tau a}{\sqrt{2\xi a}} \;=\; \frac{\tau\sqrt{\pi a}}{\sqrt{2\pi\xi}}.$$

Here, the relationship between the mode II stress intensity factor $K_{II}$ and the remotely applied load $\tau$ is defined such that

$$Z_{II} = \frac{K_{II}}{\sqrt{2\pi\xi}}.$$

Substitution of $re^{i\theta}$ for $\xi$, and recalling that $z$ is $a + \xi$ gives

$$Z_{II} \;=\; \frac{K_{II}}{\sqrt{2\pi r e^{i\theta}}} \;=\; \frac{K_{II}}{\sqrt{2\pi r}} e^{-\frac{i\theta}{2}} \;=\; \frac{K_{II}}{\sqrt{2\pi r}}\left(\cos\frac{\theta}{2} - i\sin\frac{\theta}{2}\right),$$

$$Z'_{II} \;=\; \frac{d}{dz}\left(\frac{K_{II}}{\sqrt{2\pi\xi}}\right) \;=\; -\frac{K_{II}}{2\sqrt{2\pi}\xi^{\frac{3}{2}}} \;=\; -\frac{K_{II}}{2r\sqrt{2\pi r}} e^{-\frac{3i\theta}{2}} \;=\; \frac{K_{II}}{2r\sqrt{2\pi r}}\left(-\cos\frac{3\theta}{2} + i\sin\frac{3\theta}{2}\right).$$

Substitution of these two equations into equations (1.8), (1.9) and (1.10), and recalling that $y$ is $r\sin\theta$ gives

$$\sigma_x = 0, \qquad \sigma_y = 0, \qquad \tau_{xy} = \frac{K_{II}}{\sqrt{2\pi r}}$$

when $\theta$ is 0 and $r \geq 0$. Therefore, the relationships between mode II stress intensity factor $K_{II}$, remotely applied load $\tau$, and near crack tip stress $\tau_{xy}$ are given by

$$K_{II} \;=\; \tau_{xy}\sqrt{2\pi r} \;=\; \tau\sqrt{\pi a}. \tag{1.12}$$

This definition of $K_{II}$ is only valid in the vicinity of the crack tip, and describes a singular stress at the crack tip, but a stress that approaches zero far from the crack tip. The actual stress distribution is given by equation (1.11), which describes the stress singularity at the crack tip, as well as the constant far-field stress $\tau$. Although more accurate, equation (1.11) is less convenient than equation (1.12). These stress distributions are illustrated in Figure 1.6.

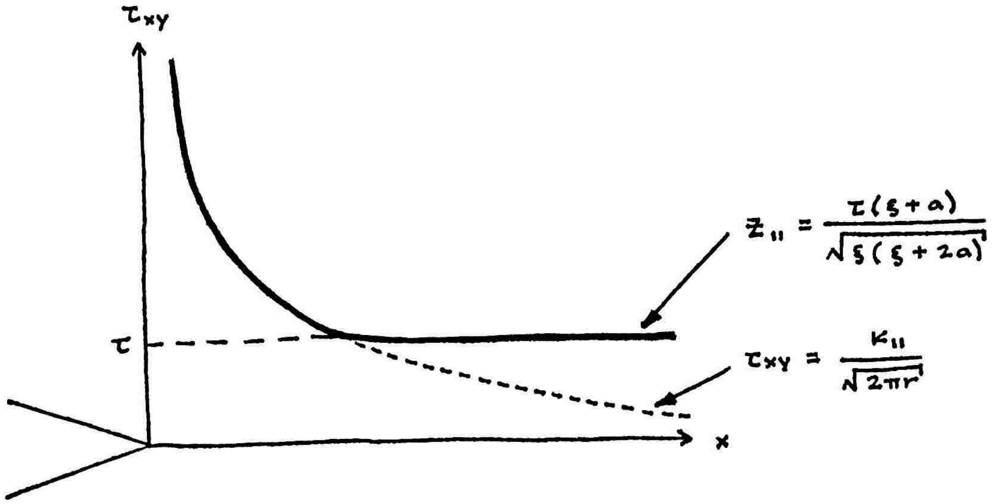

Figure 1.6: Stress distribution at an ideally sharp crack tip in a perfectly brittle material

As previously mentioned, these definitions of $K$ are restricted to straight crack, infinite body, uniform remote boundary condition problems. Regardless of modifications to Westergaard's approach, and of variations in geometry and loading, all relations between stress intensity factor and crack tip stress follow the same general form

$$\sigma_{ij} = \frac{K}{\sqrt{2\pi r}} f_{ij}$$

where $f_{ij}$ is a dimensionless factor which depends on geometry and loading [Sanford, 2003]. Furthermore, the relation between stress intensity factor and remotely applied load follow the general form

$$K = \sigma_{ij}\sqrt{\pi a}\;Y$$

where $Y$ is a dimensionless factor which contains information about the influences of finite geometry [Sanford, 2003].

### *1.5.3 J-Integral (J)*

An alternative expression for the strain energy release rate is the J-integral $J$. The J-integral is a path-independent (see Appendix D) line integral whose evaluation represents the energy released as a result of crack extension per unit of newly created crack surface for linear elastic or nonlinear elastic materials [Mamidala, 2018]. The nonlinear elastic material behavior can also be extended to elastic-plastic material behavior where the nonlinear elastic material exhibits linear behavior within a yield surface, and a nonlinear hardening response for stress states beyond yield [Rice, 1968]. This comparison of material models is illustrated in Figure 1.7. For the extension from linear elastic to elastic-plastic materials, the J-integral is defined assuming that there is no unloading [Mamidala, 2018].

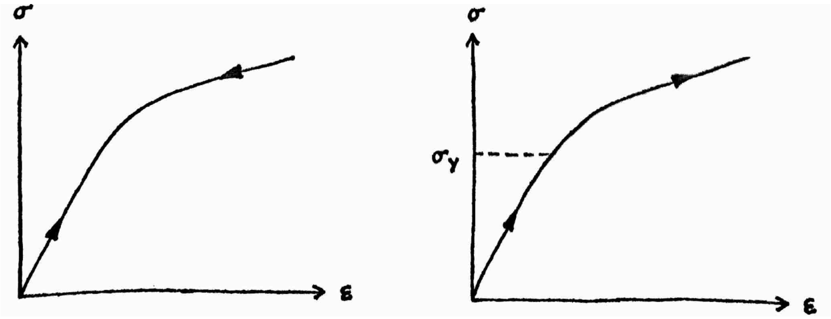

Figure 1.7: Nonlinear elastic material with loading and unloading (left), and elastic-plastic material with post-yield stiffness and with loading only (right)

Consider the structure in Figure 1.8 composed of homogeneous material subjected to a two-dimensional displacement field. A straight crack is a limiting case, i.e. the crack is limited to a plane parallel to the $x$-axis. Rice defines the J-integral as

$$J = \int_{\Gamma} \left( W dy - \mathbf{T} \cdot \frac{\partial \mathbf{u}}{\partial x} ds \right) \tag{1.13}$$

where $\Gamma$ is the curve surrounding the notch tip (which could be sharp or otherwise) to be integrated along in a counterclockwise fashion, $W$ is the strain energy density

$$W = \int_{0}^{\varepsilon_{ij}} \sigma_{ij} \; d\varepsilon_{ij},$$

$\mathbf{T}$ is the traction vector defined according to the outward normal along $\Gamma$

$$T_i = \sigma_{ij} n_j,$$

$\mathbf{u}$ is the displacement vector, and $ds$ is an element of arc along $\Gamma$.

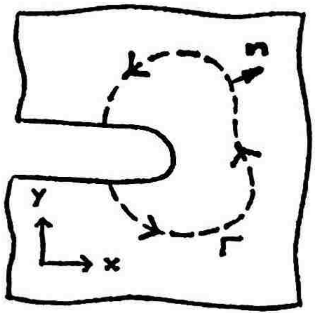

Figure 1.8: Flat surfaced notch in two-dimensional deformation field

Equation (1.13) gives the strain energy release rate for linear elastic and elastic-plastic materials, while equation (1.4) gives the strain energy release rate for only linear elastic materials. In other words, $J$ is the strain energy release rate for brittle and ductile materials, while $G$ is the strain energy release rate for only brittle materials. Therefore, $G = J$ for brittle materials.

### *1.5.4 Relating G, K, and J*

The relationship between $G$ and $K$ can be derived from work done by several individuals in the first half of the 20th century. Inglis developed near crack stress component solutions for an elliptical crack passing through an infinite, homogeneous, isotropic plate of uniform thickness subjected to a remote fixed displacement causing a tensile stress normal to the crack orientation [Inglis, 1913]. Griffith used these stress solutions and assumed a narrow crack to develop the following equation which describes the elastic energy due to the presence of the crack for the system under displacement controlled loading

$$U_s \;=\; -\frac{(\kappa+1)\pi a^2\sigma^2}{8\mu}$$

where $\kappa$ is $(3-\nu)/(1+\nu)$ for the plane stress condition, $\nu$ is Poisson's ratio, $2a$ is the crack length (major axis of the ellipse), $\sigma$ is the stress induced by a remote fixed displacement, and $\mu$ is the shear modulus [Griffith, 1920]. Making the substitution for $\kappa$ and recalling that $E$ is $2\mu(1+\nu)$ for an isotropic material gives

$$U_s \;=\; -\frac{\pi a^2\sigma^2}{E}.$$

Griffith also defined the energy of the surface of the crack as

$$\Gamma \;=\; 4a\gamma_s$$

where $\gamma_s$ is surface tension. Plugging these definitions into the crack growth initiation criterion established in equation (1.3) gives

$$\frac{\partial U}{\partial a} \;=\; 4\gamma_s - \frac{2\pi a\sigma^2}{E} \;=\; 0,$$

and solving for $\sigma$ gives

$$\sigma = \sqrt{\frac{2\gamma_s E}{\pi a}}.$$

This equation is valid for brittle materials, and Griffith verified his theory by testing glass. Irwin [1948] and Orowan [1949] independently hypothesized that the total surface energy must include a plastic portion $\gamma_p$, such that

$$\sigma = \sqrt{\frac{2(\gamma_s + \gamma_p)E}{\pi a}}.$$

This does not change the relationship established by Griffith, rather it extends the theory for brittle materials to ductile materials. Therefore, $\sigma$ may be expressed as

$$\sigma = \sqrt{\frac{2\gamma E}{\pi a}} \tag{1.14}$$

where $\gamma$ is the total surface tension, including both elastic and plastic portions. Recall from Section 1.5.1 the strain energy release rate $G$ is defined as the energy released as a result of crack extension per unit of newly created crack surface, and therefore

$$G = 2\gamma.$$

Substituting $G$ into equation (1.14) gives

$$\sigma = \sqrt{\frac{GE}{\pi a}}. \tag{1.15}$$

From Section 1.5.2 the stress intensity factor $K$ is $\sigma\sqrt{\pi a}$. Substituting this into equation (1.15) establishes the relationship between stress intensity factor $K$ and strain energy release rate $G$ as

$$K^2 = GE. \tag{1.16}$$

The derivation presented above is for mode I, but similar logic may be used to establish the relationship for other fracture modes. The relation between $G$ and $K$ for mode II is [Mamidala, 2018]

$$G_{II} = \frac{K_{II}^2}{E}. \tag{1.17}$$

The relation between $K$ and $J$ can be derived by considering a body composed of elastic-plastic material with a narrow notch and small scale yielding such that the yield zone near the crack tip is small compared to the geometric dimensions. The finite scenario may be reasonably approximated with a semi-infinite notch in an infinite body where the stresses in the vicinity of the crack tip are known as (see Section 1.5.2)

$$\sigma_{ij} = \frac{K}{\sqrt{2\pi r}} f_{ij}.$$

Utilizing this definition of stress, and evaluating $J$ for a circular $\Gamma$ with radius $r$ gives

$$J = \frac{K^2}{E}$$

for the plane stress condition [Rice, 1968]. The fact that $J$ is path independent (see Appendix D) means that this relationship holds for any $\Gamma$ surrounding the notch. Therefore, the relation between $J$ and $K$ for mode II is

$$J_{II} = \frac{K_{II}^2}{E}. \tag{1.18}$$

Noticing similitude between equations (1.17) and (1.18) provides the final relation between $J$ and $G$ (for brittle materials)

$$J_{II} = G_{II}. \tag{1.19}$$

### 1.5.5 *Crack Growth Stability*

Cracks may grow gradually or suddenly when the critical state is reached. The stability of crack growth can be determined through the energy approach, and examination of the strain energy release rate $G$. The conditions for stable crack growth for a brittle material are [Mamidala, 2018]

$$G = G_C, \tag{1.20}$$

$$\frac{\partial G}{\partial a} < 0. \tag{1.21}$$

Recall that $G$ is the first derivative of energy with respect to $a$, and therefore $\partial G/\partial a$ is the second derivative of energy. Hence, the condition $G = G_C$ identifies equilibrium, while $\partial G/\partial a < 0$ indicates stability.

The mode II fracture testing done in fulfillment of this thesis was carried out under displacement control. Taking this into consideration and differentiating equation (1.4) once with respect to $a$ gives

$$\frac{\partial G}{\partial a} = \frac{v^2}{2B}\left[\frac{1}{C^2}\frac{\partial^2 C}{\partial a^2} - \frac{2}{C^3}\left(\frac{\partial C}{\partial a}\right)^2\right]. \tag{1.22}$$

Plugging (1.22) into (1.21), and with some rearranging, gives

$$\frac{1}{2}\frac{(C)(\frac{\partial^2 C}{\partial a^2})}{(\frac{\partial C}{\partial a})^2} < 1 \tag{1.23}$$

as the condition for stable crack growth.

For brittle materials, $G_C$ is a material property and therefore remains constant with change in crack length $a$. However, observed in some real materials is a disparity between the initiation value of $G_C$ and the propagation values of $G_C$ in that the propagation values increase with increasing $a$. This relationship between $G_C$ and $a$ has been called the $R$-curve, where ductile materials exhibit a rising $R$-curve and brittle materials exhibit a flat $R$-curve.

$R$ describes the resistance of the material to crack extension, or conversely to $G$, it describes the energy absorbed due to the formation of new crack surfaces, and an increasing fracture process zone size. With this adjustment, the conditions for stable crack growth become [Mamidala, 2018]

$$G = R,$$
$$\frac{\partial G}{\partial a} < \frac{\partial R}{\partial a}.$$

### *1.5.6 Plastic Zone Size*

The stress-based fracture theory used to define the stress intensity factor $K$ from Section 1.5.2 describes a singular stress at an ideally sharp crack tip in a perfectly brittle material. Real materials cannot carry infinite stress, consequently the theory must be adjusted to account for material yielding.

By limiting the stress to the yield stress $\tau_y$, an estimate for the yield zone size $r_y$ is obtained by substituting $\tau_y$ and $r_y$ into equation (1.12) and rearranging

$$r_y = \frac{1}{2\pi}\left(\frac{K_{II}}{\tau_y}\right)^2.$$

This does not account for the redistribution of stress caused by yielding (the shaded area in Figure 1.9), therefore equilibrium must be maintained by translating the stress distribution to the right, where the equilibrium radius is defined as the plastic zone size $r_p$ (shown in Figure 1.10 on the left) [Sanford, 2003]. The force balance is given by

$$\tau_y r_p \; = \; \int_0^{r_y} \tau_{xy} dr \; = \; \int_0^{r_y} \frac{K_{II}}{\sqrt{2\pi r}} dr \; = \; \frac{K_{II}}{\sqrt{2\pi}} 2\sqrt{r_y},$$

and is illustrated in Figure 1.10 on the right, where $r_p$ is defined such that the shaded areas $A$ and $B$ are equal. Substitution of the equation for $r_y$ from above into the force balance

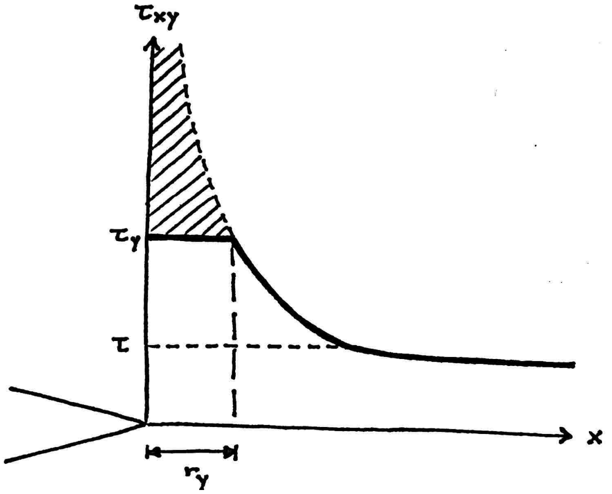

Figure 1.9: Estimate for yield zone size $r_y$

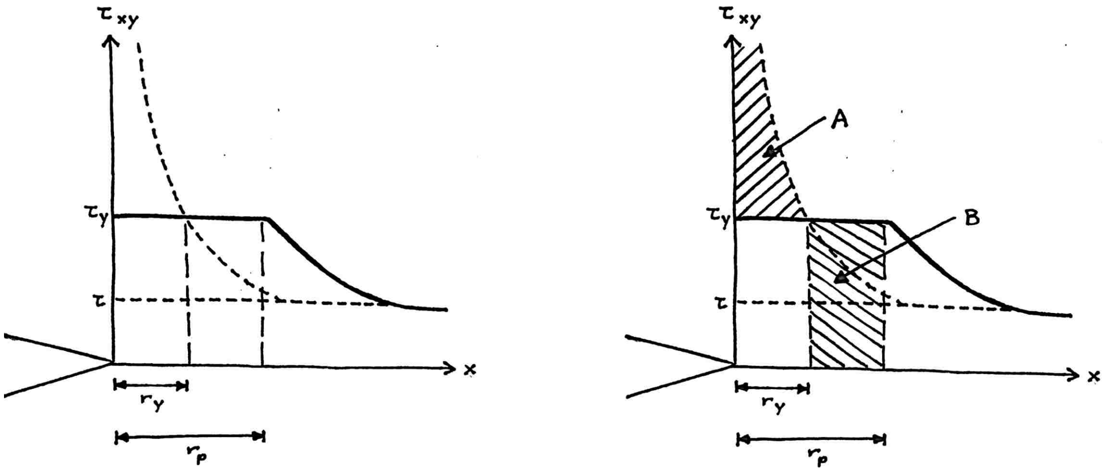

Figure 1.10: Estimate for plastic zone size $r_p$ (left), and force balance (right)

gives

$$\tau_y r_p \;=\; \frac{2K_{II}}{\sqrt{2\pi}}\frac{1}{\sqrt{2\pi}}\frac{K_{II}}{\tau_y} \;=\; \frac{2K_{II}^2}{2\pi\tau_y}.$$

Therefore, the estimate for the plastic zone size is

$$r_p = \frac{1}{\pi}\left(\frac{K_{II}}{\tau_y}\right)^2.$$

This definition assumes plane stress and elastic-perfectly plastic material behavior. This approach yields only an estimate for the plastic zone size. In reality, the plastic deformation invalidates the assumptions which are used to derive this stress field.

This estimation for the plastic zone size, despite its limiting assumptions, is critical to the extension of linear elastic fracture mechanics to materials that exhibit localized yielding [Sanford, 2003]. Alternate models have been proposed and are summarized in Table 1.1 [Turon et al., 2007].

Table 1.1: Plastic Zone Size Estimates

| Model | $r_p$ |
|---|---|
| Irwin | $\frac{1}{\pi}(\frac{K_{II}}{\tau_y})^2$ |
| Dugdale, Barenblatt | $\frac{\pi}{8}(\frac{K_{II}}{\tau_y})^2$ |
| Rice | $\frac{9\pi}{32}(\frac{K_{II}}{\tau_y})^2$ |
| Hillerborg | $(\frac{K_{II}}{\tau_y})^2$ |

## Chapter 2

# EXPERIMENTAL TESTING

This chapter discusses the mode II specimen selection considerations, as well as the ELS specimen fabrication process, the testing equipment, and the testing procedure. The three-point bending end-notched flexure (ENF) specimen was standardized by ASTM in 2014, and is the only pure mode II fracture test that is standardized by ASTM. Despite this, the ELS specimen was selected for this thesis primarily due to its longer stable crack propagation span relative to the ENF specimen (as will be shown in Section 2.1), to serve as a comparison for previous ENF testing done within the research group, and for the prospect of fracture testing in a CT scanner. The ELS specimens were cut from the same composite plates as the ENF specimens, and hence the two specimens have identical fabrication procedures. The ELS and ENF specimens were also tested in the same machine, however, the test fixtures and procedures were modified for the ELS specimen tests. Since the ELS specimen is not standardized, the strategy for experimental testing was to incorporate both the ASTM standard for the ENF specimen, and an ELS protocol published by the European Structural Integrity Society (ESIS). Therefore, an effort is made in the following sections to not only outline the experimental testing procedure, but to discuss the reasoning behind the decisions made for the experimental testing protocol.

## *2.1 Mode II Protocol Selection*

Although not standardized, the four-point end-notched flexure (4ENF), and ELS specimens are popular alternatives to the ENF specimen. These three specimens are illustrated in Figure 2.1. The 4ENF specimen offers superior stability to the ENF specimen, has a relatively simple test fixture, and has straightforward data analysis [Brunner et al., 2008]. The ELS

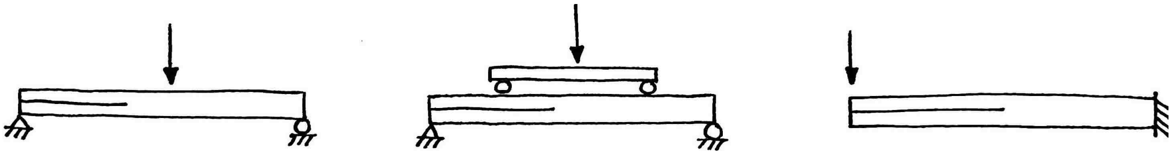

Figure 2.1: ENF specimen (left), 4ENF specimen (middle), and ELS specimen (right)

specimen offers similar advantages, but with the prospect of testing in a CT scanner, ELS was favored over 4ENF due to its longer unobstructed span for observing the crack front advance during delamination propagation.

To investigate the stability of the ENF and ELS specimens, consider the stability condition given by equation (1.23). The ***ELS specimen*** has a compliance given by (see Appendix A)

$$C = \frac{3a^3 + L^3}{24EI}.$$

Plugging this compliance into equation (1.23) gives

$$\frac{1}{2}\frac{\left(\frac{3a^3+L^3}{24EI}\right)\left(\frac{18a}{24EI}\right)}{\left(\frac{9a^2}{24EI}\right)^2} < 1,$$

and with some rearranging this relation becomes

$$\frac{a}{L} > \left(\frac{1}{6}\right)^3 \qquad \rightarrow \qquad \frac{a}{L} > 0.550.$$

Furthermore, the valid range for $a/L$ is $0 \leq a/L \leq 1$, therefore the requirement for stable crack growth for the ELS specimen is

$$0.550 < \frac{a}{L} \leq 1.$$

The compliance for the ***ENF specimen*** is

$$C = \frac{3a^3 + 2L^3}{96EI},$$

Plugging this compliance into equation (1.23) gives

$$\frac{1}{2}\frac{\left(\frac{3a^3+2L^3}{96EI}\right)\left(\frac{18a}{96EI}\right)}{\left(\frac{9a^2}{96EI}\right)^2} < 1 \qquad \rightarrow \qquad \frac{a}{L} > \left(\frac{1}{3}\right)^3 \qquad \rightarrow \qquad \frac{a}{L} > 0.693.$$

Therefore, the requirement for stable crack growth for the ENF specimen is

$$0.693 < \frac{a}{L} \leq 1.$$

This exercise shows that a smaller crack length to free length ratio is required to achieve stable crack growth, and hence a longer stable crack propagation span is attainable for the ELS specimen compared to the ENF specimen. Although the total ENF specimen length is $2L$, it is difficult to achieve continuous, stable crack growth beyond the load application point due to the change in sign of shear.

Despite the advantage of greater crack growth stability, the ELS specimen is more susceptible to large displacements, and the clamped end introduces uncertainty and variability as it is difficult to achieve perfect fixity, and identical clamping is difficult to repeat for different tests. Furthermore, lower values of the elastic modulus are measured with the ELS specimen compared to ENF, which is troublesome since the three-point bending test is standardized by ASTM for determining flexural modulus while the cantilever test is not [Blackman et al., 2006]. These disadvantages must be considered when moving forward with this specimen selection.

## *2.2 End Loaded Split (ELS) Specimen Fabrication*

The composite material used was P707AG-15 (AMS 3960) unidirectional prepreg. Prepreg is a composite material in which the fibers are embedded (pre-impregnated) with a resin, therefore to create a layup the prepreg layers were simply stacked directly on top of one another. Two different layups were used to create specimens of two different thicknesses: $[0_{26}]$ for specimens with a thickness of approximately 4 mm; and $[0_{52}]$ for specimens with a thickness of approximately 8 mm. These layups are consistent with ASTM which requires that laminates contain an even number of plies, and that laminates be unidirectional [ASTM, 2014].

A Teflon insert was used to seed delamination. A double layer of 01-14840 non-porous Teflon coated release fabric was placed at the mid-plane of the layup and oriented such that the delamination front would advance in the 0° direction in accordance with ASTM. The double layer was used in the hopes that it would facilitate the removal of the Teflon after curing, but it was found during ENF testing that efforts to remove the Teflon caused uncertainty of the inner unbonded surfaces of the laminate.

After the layup was created, the composite plate was placed inside a vacuum bag, then inside an autoclave; the autoclave at the University of Washington's Mechanical Engineering Composite Shop was used for this thesis. An autoclave is a pressurized oven in which compressed air, in combination with a vacuum bag, helps force air out of the composite to ensure a high quality final product. The curing cycle used is shown in Figure 2.2. First, 22 inches Hg minimum pressure was applied to the vacuum bag assembly, and leakage was checked for compliance with the maximum allowable leak rate of 2.0 inches Hg over 5 minutes.

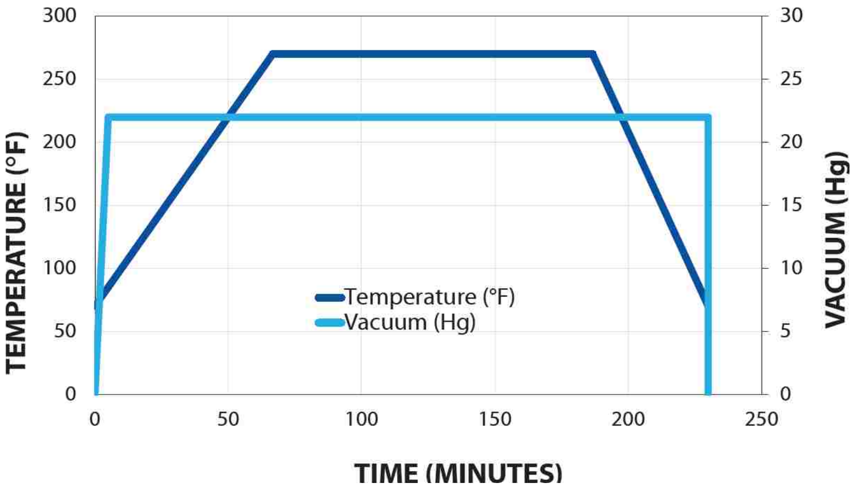

Figure 2.2: Cure cycle [Toray Composites America, Inc., 2018a]

Then, a temperature ramp was applied from ambient to $270 \pm 10$°F at a rate of $3.0 \pm 1.0$°F per minute. The cure temperature was maintained at $270 \pm 10$°F for 120-150 minutes. Then, the temperature was cooled to 170°F or lower at a rate of $4.5 \pm 0.5$°F per minute before removing the pressure. Finally, the bagged laminates were removed from the autoclave, and the laminates were removed from the vacuum bags for inspection. This material is specifically formulated for out-of-autoclave processing. The manufacturer's data sheet recommends oven curing, but despite this, the autoclave curing cycle used for these composite plates is identical in pressure and temperature to the oven curing cycle recommended by the manufacturer [Toray Composites America, Inc., 2018a].

This thesis seeks to characterize mode II fracture behavior through material parameters which should be independent of geometry. Therefore, different types of specimens, as well as the influences of width, length, and thickness should be evaluated [Davies et al., 2001]. Three different geometry ELS specimens were tested for this thesis, and are detailed in Table 2.1. The ELS dimensions were designed to be similar to the ENF specimens previously tested, whose dimensions are detailed in Table 2.2. Both the ENF and ELS specimens were cut from the same composite plates (after curing) using a table saw.

ESIS recommends a free length of 100 mm, and an initial crack length of 60 mm for ELS, while ASTM requires a free length of 50 mm, and an initial crack length of 30 mm for ENF. The length of the entire specimen is longer than this to accommodate for multiple tests on one specimen. For specimen width, ASTM requires between 19-26 mm, while ESIS recommends 20 mm, although other widths may be used so long as they fall within 15-30 mm. ASTM has no thickness requirement, but ESIS recommends a 3 mm thickness for 60% by volume carbon fiber reinforced composites (the material used for this thesis has a fiber volume fraction of 54.4%). The specimen dimensions for both the ELS and ENF specimens generally meet the suggestions and requirements from ASTM and ESIS.

Specimens were labeled such that they were distinct from each other, and the location of each specimen on the original plate was recorded. ASTM requires that the beam width be measured at 3 points which are the contact locations of the three rollers, and that the

Table 2.1: ELS Specimen Intended Geometries

| Thickness [mm] | Free Length [mm] | Initial Crack Length [mm] | Width [in] |
|---|---|---|---|
| 8 | 100 | 60 | 1 |
| 4 | 100 | 60 | 1 |
| 4 | 50 | 30 | 1 |

Table 2.2: ENF Specimen Intended Geometries

| Thickness [mm] | Free Length [mm] | Initial Crack Length [mm] | Width [in] |
|---|---|---|---|
| 8 | 100 | 60 | 1 |
| 4 | 50 | 30 | 1 |

thickness be measured at 6 points, with two thickness measurements at each of the 3 points where the width was measured, on the left and right sides of the beam. ESIS suggests that the width and thickness be measured at 5 points on the beam (quarter, center, three-quarters, and 10 mm from each end). In an effort to incorporate both ASTM and ESIS, the width and thickness of each specimen were measured at 1 inch (25.4 mm) intervals along the length, where the width was measured once per interval, and the thickness was measured twice per interval, on the left and right sides of the beam. For experimental data analysis, and for inputs to the Abaqus simulations, these width and thickness values were averaged to obtain one width and one thickness value for each specimen, and are shown in Table 2.3.

ASTM and ESIS both require that at least 5 specimens are tested per test condition, but due to the interest in testing multiple geometries to investigate size effects, as well as the timeline for this thesis, the 5 specimen requirement was not reached for ELS. Rather, two specimens were tested for each of the approximately 8 mm thick and 100 mm long, and 4 mm thick and 50 mm long specimens, and one specimen was tested for the approximately 4 mm thick and 100 mm long specimen.

Table 2.3: ELS Specimen Widths and Thicknesses

| Specimen Number | Average Width [mm] | Average Thickness [mm] |
|---|---|---|
| 2 | 23.48 | 7.79 |
| 3 | 23.47 | 7.75 |
| 6 | 22.88 | 3.65 |
| 1 | 22.42 | 3.81 |
| 3 | 22.86 | 3.66 |

Finally, specimen preparation included painting the specimens such that a digital image correlation (DIC) system could be used to collect displacement field data during testing. One through-thickness face of every specimen was painted first with a white background, then with a black speckle on top of the white, as shown in Figure 2.3. The DIC system uses cameras to observe motion of the speckle to provide the displacement field data, where the dots in the speckle discretize the face of the specimen in a similar way to the nodes of a finite element model. The paints used for this thesis were the black and white colored spray paints by Montana Black. First, the white paint was applied for a solid background, then was left to dry for at least two days. Then, the black paint was applied lightly as to just barely allow the end of the spray stream to touch the beam, and this was left to dry for at least one day.

## *2.3 Test Setup*

The ESIS suggested test setup is shown in Figure 2.4. This configuration would be difficult to manufacture given the resources available for this thesis, and the adhering of the loading block to the specimen complicates the process of adjusting the specimen in the test fixture to allow for multiple tests on one specimen. For these reasons, the configuration shown in Figure 2.5 was used, which uses a loading roller like that used for the ENF specimen, and an

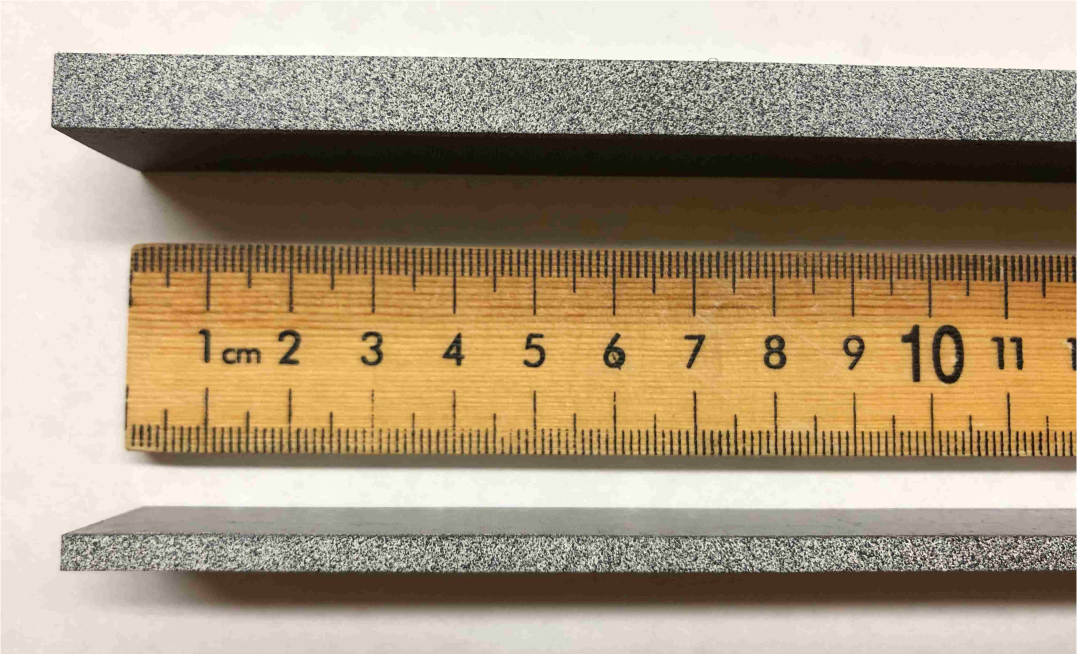

Figure 2.3: Beam speckle shown on an approximately 8 mm thick specimen (top), and on an approximately 4 mm thick specimen (bottom)

immobile clamped end. The roller radius used was 6.34 mm, which is the same radius used for the ENF tests (ASTM requires that the loading roller have a radius in the range 4.7-9.6 mm). The displacement controlled loading was applied to the specimens via the Instron 5585H with a 250 kN load cell in the University of Washington's Mechanical Test Lab. The clamped end was created by sandwiching the specimen between two aluminum plates. The dimensions of the aluminum plates were designed such that when bolted to the Instron base plate, the 50 mm and 100 mm beam free lengths could be attained. Data collection devices for these tests included the Instron for load and displacement data from the load application point, and the DIC system for the through-thickness displacement field of the beam. The experimental test setup is shown in Figure 2.6, where the specimen is placed in the clamped fixture, the Instron actuator moves down or up to load or unload the beam, and the cameras and lights are pointed at the beam to collect images for the DIC system. The overhang of the beam extending past the load application point does not affect the beam behavior.

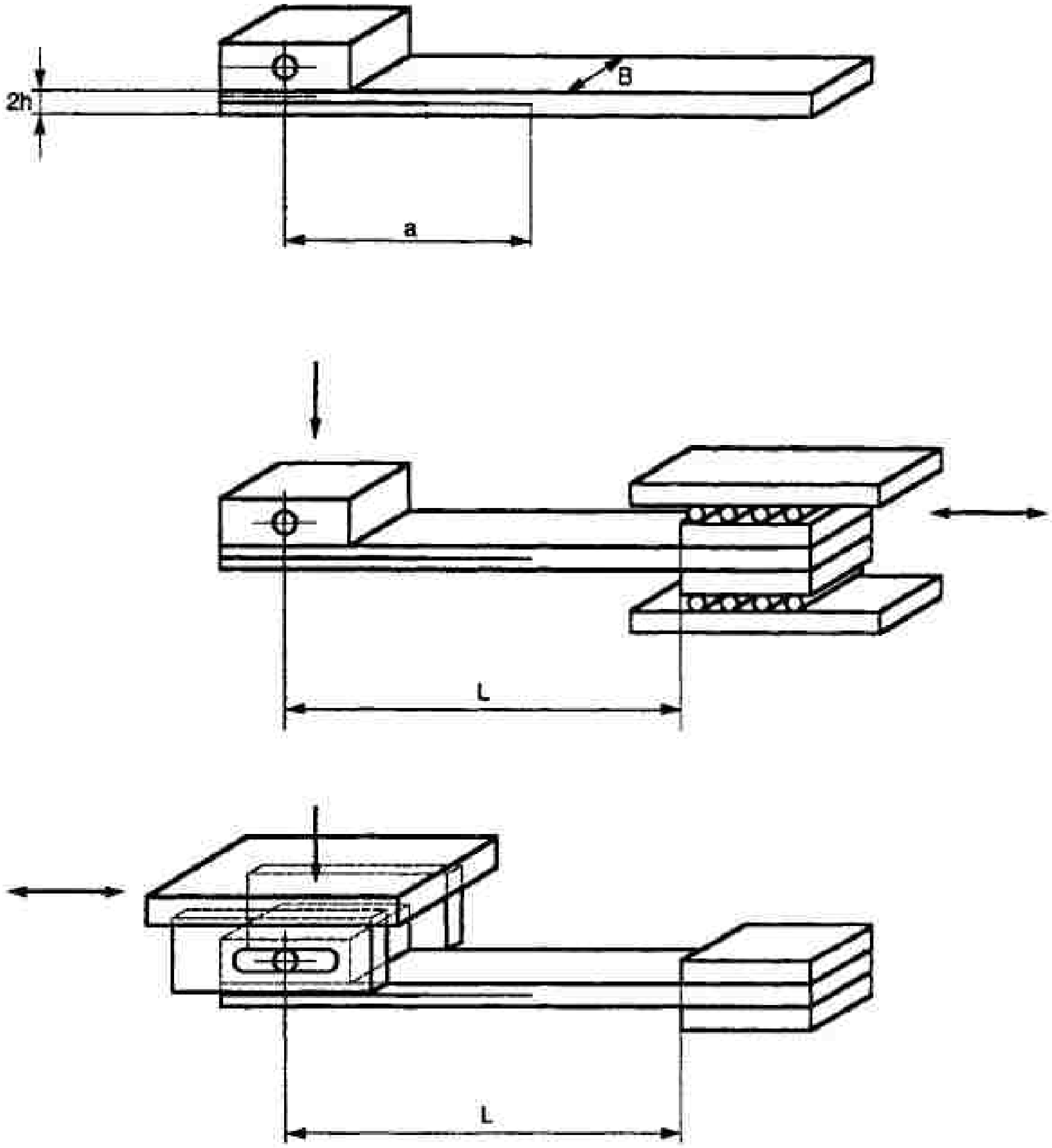

Figure 2.4: ESIS proposed ELS specimen with load block (top), clamping arrangement free to slide with fixed load point (middle), and fixed clamping arrangement with load point free to slide (bottom) [Davies et al., 2001]

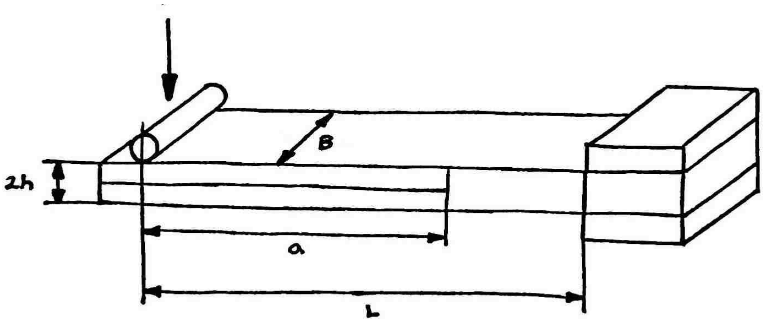

Figure 2.5: Schematic of the ELS specimen and test fixtures used for this thesis

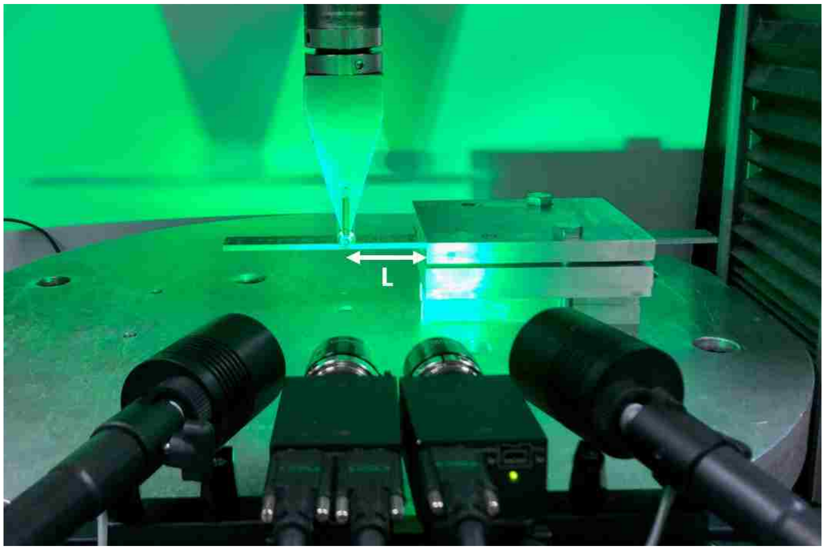

Figure 2.6: Experimental testing setup, with the cameras and lights in the foreground pointed at the specimen, and the Instron actuator with the loading roller contacting the specimen in the clamped fixture

### 2.4 Test Procedure

ASTM considers the compliance calibration method as the only acceptable method for data reduction for the ENF test. ESIS offers the compliance calibration method, as well as a beam theory method for the ELS test. The compliance calibration method (for both ENF and ELS) uses

$$G_{IIC} = \frac{3mP_{max}^2 a_0^2}{2B}$$

to calculate the mode II critical strain energy release rate $G_{IIC}$, while the beam theory method (for ELS) uses

$$G_{IIC} = \frac{9P_{max}^2 a_0^2}{4EB^2h^3}.$$

The compliance calibration method requires finding a linear $C$ vs. $a^3$ relationship given by $C = ma^3 + A$, while the beam theory method requires finding $E$. The compliance of the ELS specimen (see Appendix A)

$$C = \frac{3a^3 + L^3}{24EI}$$

is analogous to $C = ma^3 + A$, therefore solving for $m$ by differentiating the ELS compliance once with respect to $a^3$ gives

$$m \;=\; \frac{3}{24EI} \;=\; \frac{1}{8EI}.$$

Plugging this $m$ into the compliance calibration equation for $G_{IIC}$ shows that the compliance calibration method and beam theory equations for $G_{IIC}$ are theoretically identical

$$G_{IIC} \;=\; \frac{3\left(\frac{1}{8EI}\right)P_{max}^2 a_0^2}{2B} \;=\; \frac{(3)(12)P_{max}^2 a_0^2}{16EB^2h^3} \;=\; \frac{9P_{max}^2 a_0^2}{4EB^2h^3},$$

however differences may be observed between the $G_{IIC}$ values calculated using these two methods as the data is used in different ways. Both the compliance calibration method, and the beam theory method were used for data reduction for this thesis, therefore both the $C$ vs. $a^3$ relationship, and $E$ were determined during testing.

At the start of each day of testing, the DIC system was calibrated according to the testing guide [Correlated Solutions, 2016]. The Instron did not require calibration. To start each test, both the Instron and the DIC were zeroed, the data recording was started, then the loading was started. After each test was completed (the specimen was completely unloaded) the data recording was stopped, and the data was saved.

For each specimen, one pristine test, one non-precracked (NPC) fracture test, and at least one precracked (PC) fracture test were performed. The pristine test was done by placing the crack in the clamping fixture such that the free length tested did not contain a crack, and the force-displacement data was used to determine $E$ (which is discussed in Chapter 4). The NPC fracture test propagates the delamination from the Teflon insert, while the PC fracture test propagates the delamination from the mode II precrack created from the NPC test. For each NPC and PC test, the linear $C$ vs. $a^3$ relationship was determined by following an identical procedure. Three different crack lengths were tested, where the two "compliance calibration" crack lengths are shorter and longer than the "fracture" crack length. Each of the compliance calibration tests was done such that the peak force achieved during the test was 50% of the expected value of the critical force for that particular crack length, consistent with ASTM. Since ENF tests had already been performed with the same material, the peak forces were estimated based on the data from these tests under the assumption that $G_{IIC}$ is a material property, and would therefore be similar between the ENF and ELS tests. The fracture tests were carried out such that the specimens were loaded until the crack reached maximum length, which was identified when the force-displacement curve reaches a constant positive slope after the decrease in force due to crack propagation during displacement controlled loading. The crack lengths tested in order are 20 mm and 40 mm for compliance calibration, and 30 mm for fracture for the specimens with a 50 mm free length; and 40 mm and 80 mm for compliance calibration, and 60 mm for fracture for the specimens with a 100 mm free length. The reproducibility and tightness of the clamping is crucial in this test [Davies et al., 2001]. Therefore, in an effort to maintain consistency the same person adjusted the specimen in the test fixture for the different crack lengths for every test.

After a fracture test was completed, the final crack length $a_{calc}$ was determined using the compliance calibration method

$$a_{calc} = \left(\frac{C_u - A}{m}\right)^{1/3} \tag{2.1}$$

where $C_u$ is the compliance of the unloading curve from the fracture test. This new crack length was used to determine the new compliance calibration, and fracture crack lengths.

To determine the linear $C$ vs. $a^3$ relationship, the compliances were obtained using a linear least squares regression analysis of the force-displacement data, and the crack lengths were assumed to be the initial crack lengths provided in Table 2.1. ASTM requires that the compliance of the two "compliance calibration" tests be obtained through a linear least squares regression analysis of the force-displacement data in the range where the force is greater than or equal to 90 N, up to the maximum force. For the compliance of the "fracture" test, the linear least squares regression analysis should include data in the range where the force is greater than or equal to 90 N, and less than or equal to 50% of the maximum force. This lower limit of 90 N is imposed such that the curve fits exclude data affected by the initial nonlinearity of the force-displacement curve due to the supports [ASTM, 2014]. These data ranges were used for the analysis of the ELS specimen data, with the exception of specimen 6 (4 mm approximate thickness and 100 mm free length) for which the lower bound of the range was modified to 40 N since the maximum load from these tests was lower than for the other specimen geometries.

For ENF, ASTM suggests that displacement controlled loading be applied at a rate of 0.5 mm/min, although rates between 0.10-0.80 mm/min are also acceptable, while for ELS, ESIS suggests that displacement controlled loading be applied at a rate between 1-5 mm/min. The actual loading rates used were variable for each specimen, as the disparate geometries required varying maximum displacements, and are shown in Table 2.4.

The Instron force-displacement results are used to determine material parameters as discussed in Chapter 4, and are compared to the numerical modeling results as discussed in

Chapter 5. The DIC system through-thickness displacement field analysis and results are discussed in Chapter 6.

Table 2.4: ELS Specimen Loading Rates for Fracture Testing

| Specimen Number | Test | Loading Rate [mm/min] |
|---|---|---|
| 2 (8 mm thick) | NPC | 1.0 |
| | PC1 | 1.0 |
| | PC2 | 0.2 |
| | PC3 | 0.2 |
| 3 (8 mm thick) | NPC | 1.0 |
| | PC1 | 1.0 |
| | PC2 | 0.2 |
| | PC3 | 0.2 |
| 6 (4 mm thick) | NPC | 1.0 |
| | PC1 | 1.5 |
| | PC2 | 1.0 |
| 1 (4 mm thick) | NPC | 0.5 |
| | PC1 | 0.5 |
| | PC2 | 0.1 |
| 3 (4 mm thick) | NPC | 0.5 |
| | PC1 | 0.5 |
| | PC2 | 0.1 |

## Chapter 3

# NUMERICAL MODELING

In Chapter 5, the experimental test data is compared to the numerical model results of two crack growth models: (1) the virtual crack closure technique (VCCT), and (2) the cohesive zone model (CZM). This chapter provides a brief overview of the theories used to establish each of these two modeling techniques, and describes the model creation procedure for both crack growth models. There are many different ways that models can be created and analyzed using Abaqus software depending on modeling needs, and user preferences, among other factors. Therefore, the procedures outlined in the following sections are simply this user's methodology, and should not be considered as the only or best ways to use VCCT and CZM in Abaqus, however they will be shown to demonstrate good agreement with the experimental data. Both of these crack growth models are commonly used in finite element model (FEM) predictions of crack growth, but both are also known to suffer errors due to size effects, which is also investigated in subsequent chapters.

This chapter describes model creation in the context of Abaqus/CAE, which is facilitated through the use of several different modules which are each described in their own subsection. To demonstrate size effects, ELS specimens with three different geometries were modeled using each of the two crack growth models, therefore this chapter focuses on describing the general model creation procedure, and specimen specific geometric and material parameters are omitted. Unless stated otherwise, all Abaqus defaults were kept. Furthermore, Abaqus is unitless, therefore it is the user's duty to maintain consistent units throughout the model. The units used for this thesis are SI (mm): length in $mm$, force in $N$, stress in $N/mm^2$, and energy in $N \cdot mm$.

### *3.1 Virtual Crack Closure Technique (VCCT) Overview*

The virtual crack closure technique uses principles of linear elastic fracture mechanics (LEFM) to study the onset and propagation of cracking [Abaqus, 2014]. It is appropriate for quasi-static problems in which brittle crack propagation occurs along predefined surfaces. Therefore, VCCT is reasonable for modeling the fracture testing done for this thesis since composites exhibit little material nonlinearity, and the delamination propagates from a seeded crack between plies in the ELS specimen. However, errors due to size effects will be shown to occur.

The virtual crack closure technique is based on the assumption that the strain energy released when a crack is extended by a certain amount is equal to the work required to close the crack by that same amount. Consider Figure 3.1 where a delamination is modeled using four-node shell elements. For VCCT, the mode I, mode II, and mode III components of the strain energy release rate must be calculated, where for the shell element formulation these are defined by Krueger [2004] as

$$\begin{aligned} G_I &= -\frac{1}{2\Delta A}\, Z_{Li}(w_{L\ell} - w_{L\ell^*}), \\ G_{II} &= -\frac{1}{2\Delta A}\, X_{Li}(u_{L\ell} - u_{L\ell^*}), \\ G_{III} &= -\frac{1}{2\Delta A}\, Y_{Li}(v_{L\ell} - v_{L\ell^*}) \end{aligned}$$

where $\Delta A = \Delta a(b_1 + b_2)/2$ is the crack surface area as highlighted in the bottom image in Figure 3.1, $X_{Li}$, $Y_{Li}$, and $Z_{Li}$ are the forces at the $Li$ nodal location, $u_{L\ell}$, $v_{L\ell}$, and $w_{L\ell}$ are the displacements at the $L\ell$ nodal location ($\ell$ corresponds to the top surface of the delamination), and $u_{L\ell^*}, v_{L\ell^*}$, and $w_{L\ell^*}$ are the displacements at the $L\ell^*$ nodal location ($\ell^*$ corresponds to the bottom surface of the delamination). These three components are then used to calculate the total strain energy release rate $G_{equiv}$, and are compared to the critical strain energy release rate components ($G_{IC}$, $G_{IIC}$, and $G_{IIIC}$) through a quasi-static mixed-mode fracture criterion. Failure is expected when, for a given mixed-mode ratio, the calculated total energy release rate $G_{equiv}$ exceeds the critical energy release rate $G_{equiv,C}$ [Krueger, 2004].

Abaqus offers several fracture criteria for mixed mode behavior. The choice of fracture criterion is not always clear for any given problem, and the best model is chosen empirically [Abaqus, 2014]. Since the tests done for this thesis were pure mode II, only the mode II critical strain energy release rate could be obtained from the experiments. The critical strain energy release rate for mode I was set to a value smaller than that for mode II, and the mode III critical strain energy release rate was set equal to that of mode II (Section 4.2 discusses further the determination of these material properties). Taking these critical strain energy release rates into consideration, the Benzeggagh-Kenane (BK) fracture criterion was selected for this thesis, for both VCCT and CZM (which is discussed later in Sections 3.3 and 3.4), because it is useful when the critical fracture energies along the first and second shear directions ($G_{IIC}$ and $G_{IIIC}$) are identical [Abaqus, 2014]. The BK law is defined by

$$G_{equiv,C} = G_{IC} + (G_{IIC} - G_{IC})\left(\frac{G_{II} + G_{III}}{G_I + G_{II} + G_{III}}\right)^{\eta} \tag{3.1}$$

where $\eta$ is a cohesive property parameter.

Since VCCT is based on LEFM, and requires only the critical strain energy release rates as inputs, its applicability is limited to brittle materials, and it does not address size effects. The effects of geometry is evident when the far-field assumptions used in the strain energy release rate derivation are violated, and when the plastic zone size is not small relative to the size of the structure. The ELS specimens used for this thesis have finite dimensions, and therefore size effects were observed and are discussed in Sections 4.3 and 5.2.3. Furthermore, VCCT cannot model crack initiation from a surface that is not already cracked, and hence requires a pre-existing flaw at the front of the crack surface [Abaqus, 2014]. Nevertheless, VCCT is a commonly used and widely accepted method for modeling delamination propagation, and will serve as a comparison for the CZM performance.

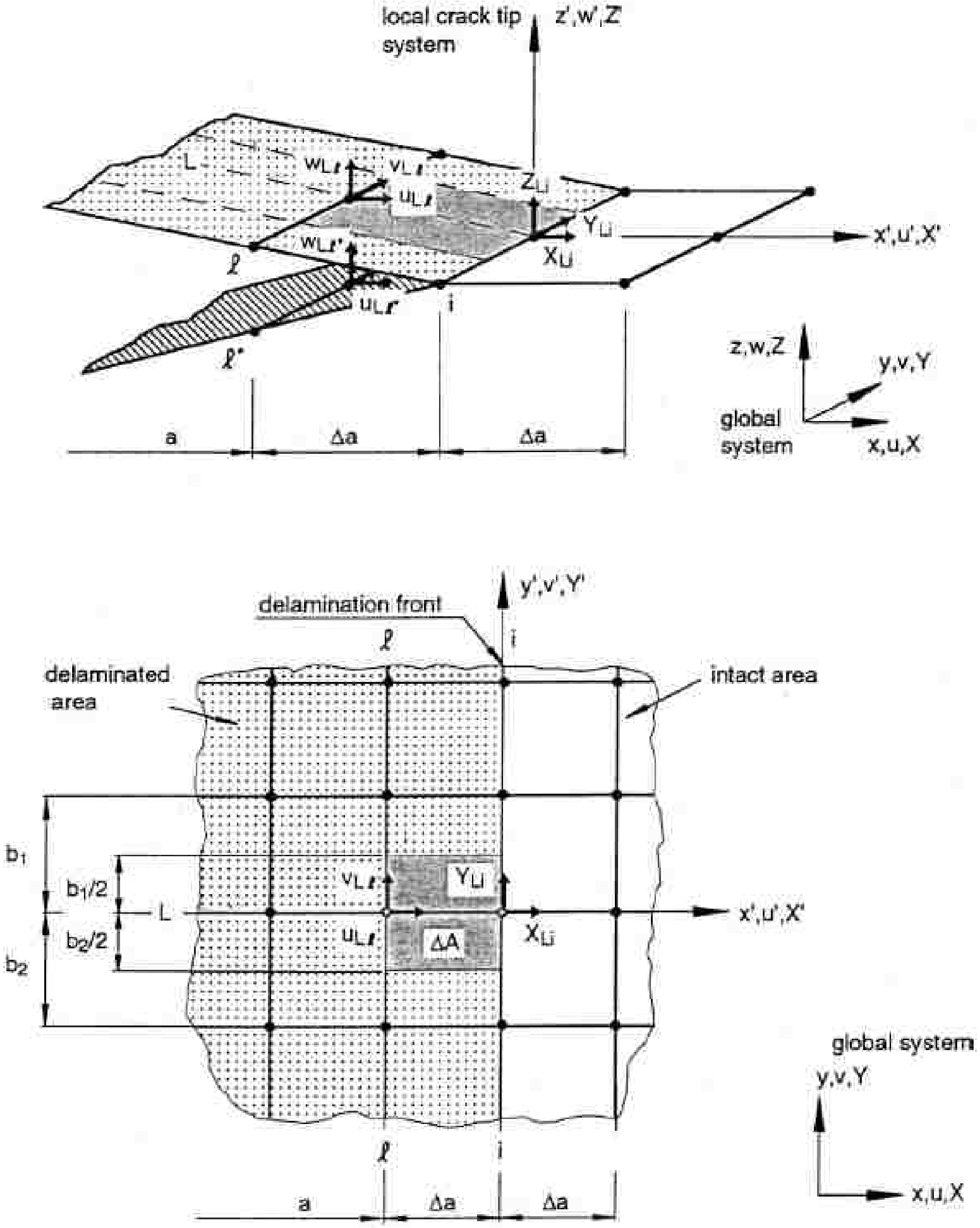

Figure 3.1: VCCT for a delamination modeled using four-node shell elements: a 3D view (top), and a 2D view looking from the top down (bottom) [Krueger, 2004]

## *3.2 Creating a VCCT Model Using Abaqus/CAE*

The modules used for the VCCT model were: part, property, assembly, step, mesh, interaction, and load. Although these modules are useful for visualizing the model during creation, they are somewhat limited in that it is not possible to implement VCCT linear scaling, or to change the allowed number of attempts per increment for convergence through the use of these modules. Therefore it was also necessary to implement keyword changes. This section discusses both how these keyword changes were made, and how each of the modules were used.

### *3.2.1 Part*

There are three ways to model composites in Abaqus: (1) with conventional shell elements, (2) with continuum shell elements, and (3) with solid elements [Abaqus, 2014]. The two-dimensional conventional shell is the most computationally efficient, and although simpler than the three-dimensional elements, it was used since it offers sufficient accuracy for the purposes of this thesis. With the use of the two-dimensional conventional shell element, a two-dimensional part was created to represent the geometry of the composite. The ELS beam is composed of two identical sublaminates (above and below the crack plane), therefore each sublaminate can be represented by one part. One part was created where the modeling space was "3D," the type was "Deformable," and the base features were the "Shell" shape and "Planar" type. Then, a rectangle was drawn whose length and width matched that of the specimen. Note that the sublaminate thickness was assigned in the property module, as described in Section 3.2.2. This created a part where the rectangle defined by the length and width of the specimen laid in the $xy$-plane. Finally, the material orientation was assigned such that the normal direction was in the $z$-direction (the thickness direction of the sublaminate).

### *3.2.2 Property*

For the sublaminate, only the elastic properties were needed. The specimens used for this thesis were all transversely isotropic, so the elastic properties were entered using the “Lamina” type, although either the “Engineering Constants” or “Orthotropic” types would also have been appropriate. Only the $E_1$ material property could be obtained from the experimental tests, and the remaining material properties were obtained from the manufacturer’s data sheet. Section 4.1 discusses the determination of material properties, and provides the values used for the numerical models.

The sublaminate material can be assigned to the sublaminate part in two ways: (1) with section creation and section assignment, and (2) with the composite layup tool. The two methods for assigning the material to the part give the same result, but the second method uses only one tool while the first method requires the use of two tools, consequently the second method was used for this thesis.

A new composite layup was created where the element type was set to “Conventional Shell.” The specimens used for this thesis were all unidirectional with identical plies, therefore according to CLT (see Section 1.3) only one ply needed to be defined where the assigned material was set to the sublaminate material created previously, the orientation angle was set to 0, and the thickness was set to the thickness of the entire sublaminate (half the total ELS beam thickness). The layup orientation was defined in the “Part global” coordinate system, where the normal direction was set to “Axis 3,” which was the axis which pointed in the thickness direction of the part. Finally, this layup was assigned to the sublaminate part by selecting the sublaminate part as the region from the viewport, and the shell offset was assigned as the “Top surface,” although the “Bottom surface” would also have been appropriate.

### *3.2.3 Assembly*

The assembly of the specimen was done by creating two instances of the sublaminate part with the “Independent” mesh option. Since the shell offset direction was set as the “Top surface” in the property module, the two sublaminate instances had the same thickness extrusion direction when first created from the sublaminate part. Therefore, one of the instances was translated and rotated such that the two sublaminate instances were stacked on top of one another with the thicknesses extruding in opposite directions. Furthermore, the sublaminates were arranged such that they laid in the $xy$-plane (the thickness extrusions pointed in the positive and negative $z$-directions). This assembly is shown in Figure 3.2.

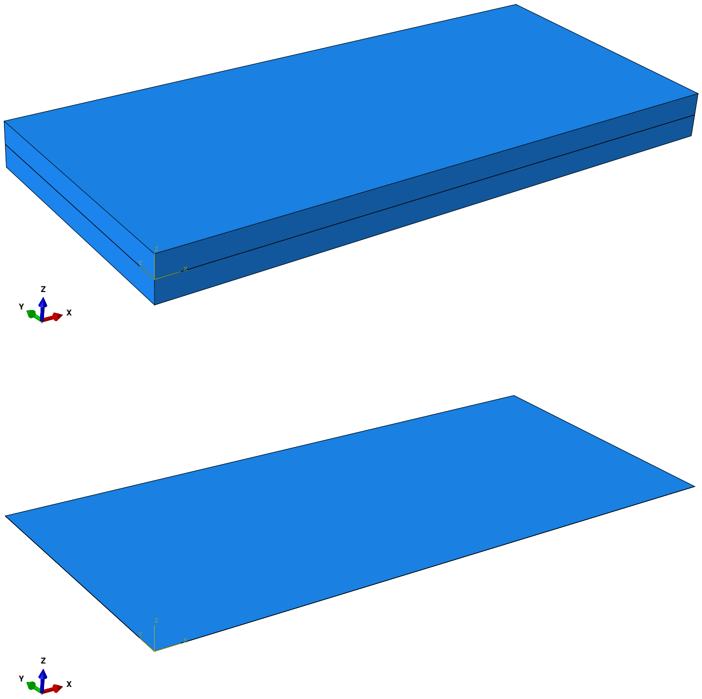

Figure 3.2: Sublaminate assembly with shell thickness rendered which shows the thicknesses extruding upward and downward for the top and bottom sublaminates, respectively (top), and without shell thickness rendered, where the two sublaminate instances are coincident in the $xy$-plane (bottom)

The sublaminate instances were then partitioned at the location of the crack tip to ensure that there would be a line of nodes at the initial crack tip location. This is important since the VCCT analysis requires the identification of a set of bonded nodes. This bonded relationship was established in the interaction module, which is discussed later in Section 3.2.6.

### *3.2.4 Step*

Although a static FEM analysis cannot accurately capture the complete dynamic progression of a fracture test, the fracture testing done for this thesis was quasi-static, therefore a static analysis is sufficient for the purposes of capturing the peak load and the post-dynamic fracture growth. One static step was created after the initial step with a procedure type of "Static, General." A large-displacement formulation was used by setting "Nlgeom" (nonlinear geometry) to "On." For a VCCT analysis, many small increments are required to obtain a solution for the entire step [Abaqus, 2014]. Therefore, the maximum number of increments was set to $10^6$, the minimum increment size was set to $10^{-300}$, and the initial and maximum increment sizes were set to 0.1. The minimum increment size was set to this arbitrary small number to essentially not impose a lower bound on the increment size.

The FEM and experimental test results compared in Chapter 5 include force and displacement at the load application point. The history output requests were modified to include the reaction force in the $z$-direction (the RF3 variable), and the displacement in the $z$-direction (the U3 variable) along the free end of the specimen. Since the free end of the specimen contains two edges (from the top and bottom sublaminates), care was taken to select only the free edge from the bottom sublaminate (the displacement controlled loading was applied to the bottom sublaminate in the positive $z$-direction, as discussed later in Section 3.2.7). A "bond state" (the BDSTAT variable) for the entire model was also added to the field output requests to allow for visualization of the crack front advance. All other output requests were kept as the Abaqus defaults.

### *3.2.5 Mesh*

Both sublaminates should have identical meshes to maximize the accuracy of the debonding simulation [Abaqus, 2014]. Therefore, the sublaminate instances were first seeded identically, then were meshed, and the element type was set to “S4,” the four-node shell element with linear shape functions and full integration. The reduced integration “S4R” element was not used because its reduced stiffness can cause spurious deformation, and lead to a scenario in which nodes that should have debonded do not debond during the VCCT analysis [Lin, 2017]. Finally, a set of bonded nodes was created by selecting all the nodes in the area where the two sublaminates were initially bonded together.

### *3.2.6 Interaction*

Two interactions were needed to determine the relationship between the sublaminates: (1) the cohesive interaction which represents the bond between the two sublaminates, and (2) the hard interaction which represents the contact between the unbonded faces of the two sublaminates. In general, interaction creation involves two steps, first creating interaction properties, then assigning the properties to an interaction.

For the cohesive interaction, an interaction property of type “Contact” was created. Then, a “Fracture Criterion” property was added, where the type was set to “VCCT,” and the direction of crack growth relative to the local 1-direction was set to “Parallel.” The BK fracture criterion was selected, and the three critical strain energy release rates were entered accordingly. The BK exponent was set to 1, as was done by [Lin, 2017]. Finally, the tolerance was set to 0.0001, and the tolerance for unstable crack propagation was turned on, keeping the default parameter. The default value for unstable crack propagation is infinite; this simply allows multiple nodes at and ahead of the crack tip to debond in one increment until the fracture criterion is satisfied, rather than cutting back the increment size to satisfy the fracture criterion for one node at the crack tip [Abaqus, 2014]. This may lead to faster crack propagation than the real dynamic progression.

After the cohesive property was created, an interaction was created to which this property was assigned. An interaction of type "Surface-to-surface contact" was created, and the step was set to "Initial." Creating the interaction in the initial step propagates the interaction to the static step that was created in the step module. One of the sublaminate inner surfaces was set as the master surface, and the other as the slave surface; since the sublaminates are identical in geometry and properties it does not matter which is which. The "Small sliding" formulation with the "Node to surface" discretization method was selected, and a $10^{-8}$ clearance was added as a "Uniform value across slave surface" to help eliminate unnecessary severe discontinuity iterations during incrementation as the crack propagated [Abaqus, 2014]. The limiting of bonding to slave nodes in a subset was turned on, and the set of bonded nodes created in the mesh module was selected as the subset. The cohesive property previously created was selected as the contact interaction property.

To complete the cohesive interaction, a crack of type "Debond using VCCT" was created. The initiation step was set as the static step created in the step module, and the contact pair interaction was set as the cohesive interaction previously created. Finally, the "Ramp" debonding force was used. The "Ramp" option releases the traction gradually during succeeding increments that follow debonding where the reduction of the magnitude of the debonding force is governed by the critical strain energy release rate, while the "Step" option releases the traction during the increment that immediately follows debonding [Abaqus, 2014]. Consequently the "Ramp" debonding force was chosen to avoid a sudden loss of stability [Abaqus, 2014]. The difference between the "Ramp" and "Step" options may be observed in the force-displacement curve were the "Ramp" option gives a smooth force-displacement curve during crack propagation, and the "Step" option gives a jagged force-displacement response where a sudden loss in stiffness occurs when nodes debond [Bisagni et al., 2013].

The hard interaction represents the contact between the unbonded faces of the two sublaminates by preventing the interpenetration of the two sublaminates, and allowing separation after contact. An interaction property of type "Contact" was created, and a "Normal Behavior" property was added, leaving the defaults. Then, an interaction of type "General contact" was created in the initial step, and the hard property was selected as the global property assignment.

### *3.2.7 Load*

The fracture testing done for this thesis used displacement control, therefore two boundary conditions were created: (1) the boundary conditions from the experimental test, i.e. a fixed end for the ELS specimen, and (2) the displacement control at the load application point.

For the cantilever boundary condition, a boundary condition of type "Symmetry / Antisymmetry / Encastre" was created in the initial step. Next, the region over which to apply the boundary condition was selected as the two edges of the top and bottom sublaminate instances that were on the fixed end (as determined by the placement of the crack front partition created in the assembly module). Then, the "ENCASTRE" option was chosen to constrain the displacements and rotations in all directions.

For the displacement controlled loading, a boundary condition of type "Displacement / Rotation" was created in the static step. Next, the region over which to apply the boundary condition was selected as the edge of the bottom sublaminate at the free end. Finally, the displacement in the $z$-direction (the U3 variable) was set to the maximum displacement achieved during the experimental test. The bottom edge of the beam was selected and assigned a displacement controlled loading in the positive $z$-direction so that both the displacement and reaction force output variables would have positive values, similar to the experimental results. These models only simulated loading, and did not simulate unloading.

### *3.2.8 Keyword Changes*

For debonding with VCCT, the analysis often requires more attempts for convergence than the Abaqus default value allots. To increase the number of attempts per increment (called cutbacks in the Abaqus manual) beyond the default value of 5, the keyword change shown below was implemented in the step section of the keywords editor. The value used for this thesis was 100.

```
*CONTROLS, TYPE=TIME INCREMENTATION
,,,,,,,100
```

To minimize the analysis time, VCCT linear scaling was implemented. For most crack propagation simulations using VCCT, the deformation can be nearly linear up to the point of the onset of crack growth, and past this point the analysis becomes very nonlinear. Prior to crack propagation, linear scaling can be used to effectively reduce the solution time to reach the onset of crack growth [Abaqus, 2014]. The VCCT linear scaling technique uses an algorithm to quickly converge to the critical load where incrementation is controlled by

$$\Delta t_{i+1} = \left(\beta\sqrt{\frac{G_{equiv,C}}{G_{equiv}}} - 1\right)t_i,$$

and $\beta$ is set between 0.7 and 0.9 depending on the degree of nonlinearity [Abaqus, 2014]. Once the exact critical load is reached, and the first nodes at the crack tip are debonded, the linear scaling calculations are no longer valid and the time incrementation reverts back to the default [Abaqus, 2014]. To activate linear scaling, the keyword change shown below was implemented in the step section of the keywords editor. A value for $\beta$ must be assigned, where the value used for this thesis was the default value of 0.9.

```
*CONTROLS, TYPE=VCCT LINEAR SCALING
0.9
```

## 3.3 *Cohesive Zone Model (CZM) Overview*

The cohesive zone model, a common alternative to the VCCT approach, uses cohesive elements to represent the bond between plies in a laminated composite. The constitutive response of the cohesive element is described by a traction-separation law for each of the three modes of fracture. For the opening mode (mode I), the traction-separation law is defined by the relationship between normal stress and crack opening displacement, while for the shearing (mode II) and tearing (mode III) modes, the traction-separation law is defined by the relationship between shear stress and crack sliding displacement. The traction-separation law is illustrated schematically in Figure 3.3 for a shearing mode, where the constitutive behavior of each element is governed by an identical traction-separation law, and the loading and deformation of each element dictates the damage evolution of that element according to the traction-separation law.

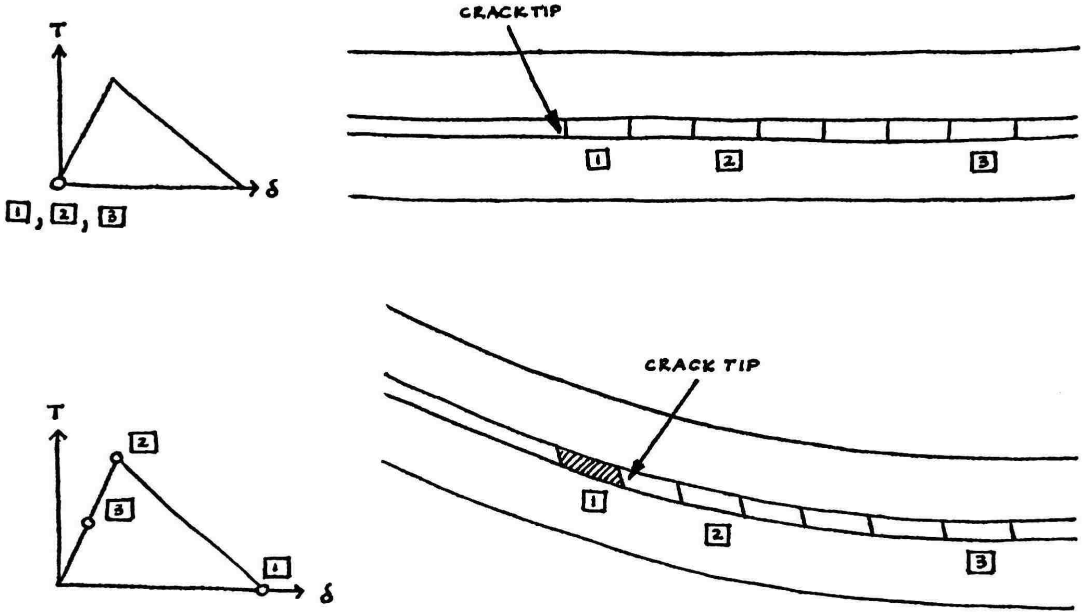

Figure 3.3: Cohesive elements at cracked interface prior to loading where all three labeled elements have zero traction and crack sliding displacement (top), and during loading where element 1 has failed, element 3 is far from the crack tip, and element 2 is near the crack tip (bottom) with the traction-separation law shown to the left

There are various ways to describe the traction-separation law, but for this thesis the traction-separation law is determined by an initially linear elastic regime described by the penalty stiffnesses ($K$ in Figure 3.4); a damage initiation point determined by the interface strengths ($T^\circ$ in Figure 3.4) and a damage initiation criterion (described later in this section); and a damage evolution law defined by the critical strain energy release rates ($G_C$, the area enclosed by the traction-separation curve, in Figure 3.4) and a fracture criterion (described later in this section). The initially linear elastic response is defined by

$$\left\{\, \mathbf{T} \,\right\} = \left[\, \mathbf{K} \,\right] \left\{\, \boldsymbol{\delta} \,\right\} \quad \rightarrow \quad \begin{Bmatrix} T_n \\ T_s \\ T_t \end{Bmatrix} = \begin{bmatrix} K_{nn} & K_{ns} & K_{nt} \\ K_{ns} & K_{ss} & K_{st} \\ K_{nt} & K_{st} & K_{tt} \end{bmatrix} \begin{Bmatrix} \delta_n \\ \delta_s \\ \delta_t \end{Bmatrix}$$

where $\mathbf{T}$ is the traction vector, $\mathbf{K}$ is the penalty stiffness matrix, $\boldsymbol{\delta}$ is the separation vector, $n$, $s$, and $t$ correspond to modes I, II, and III, and for uncoupled traction-separation behavior, only $K_{nn}$, $K_{ss}$, and $K_{tt}$ are defined. The damage initiation point was defined for this thesis using the quadratic stress damage initiation criterion which is given by

$$\left(\frac{T_n}{T_n^\circ}\right)^2 + \left(\frac{T_s}{T_s^\circ}\right)^2 + \left(\frac{T_t}{T_t^\circ}\right)^2 = 1$$

where $T_i^\circ$ are the interface strengths, and for $T_n$ a compressive displacement or stress state does not initiate damage. Finally, the damage evolution for this thesis was defined by the BK law, as discussed in Section 3.1. The damage evolution for this thesis was assumed to be linear, and Abaqus ensures during analysis that both the BK law described by equation (3.1), and the linear damage evolution requirement are met [Abaqus, 2014].

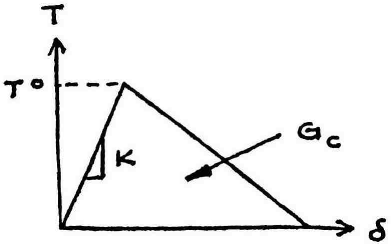

Figure 3.4: Traction-separation law with Abaqus inputs identified

The CZM is appropriate for simulating brittle or ductile fracture, and can model crack initiation from initially uncracked surfaces. Like VCCT, the CZM simulates crack propagation along a known crack surface. Furthermore, the additional model parameters (interface strengths and penalty stiffnesses in the case of this thesis, or other definitions for the traction-separation law) better equip the model to handle size effects compared to VCCT, however these parameters can be difficult to determine. The CZM is a commonly used method for predicting delamination propagation, and the advantages that the CZM offers will serve as a useful comparison for the VCCT performance, as discussed in Chapter 5.

## *3.4 Creating a CZM Using Abaqus/CAE*

The modules used for the CZM were: part, property, assembly, step, interaction, load, and mesh. These are the same modules that were used for the VCCT model, but in a different order. The mesh module was saved for last since the meshing is more complex for the CZM than for the VCCT model. Unlike the VCCT model, the CZM does not require the implementation of keyword changes.

### *3.4.1 Part*

Unlike the VCCT model where the bond between the sublaminates is established by selecting a set of nodes on the sublaminates, and assigning fracture properties and criterion to govern the relationship between the nodes, the bond for the CZM is represented through the use of cohesive elements which are placed between the sublaminates, and to which the fracture properties and criterion are assigned. Consequently, two parts were created for the CZM: (1) for the top and bottom sublaminates, and (2) for the bond. The sublaminate parts were created in the same way as the VCCT model (see Section 3.2.1). The cohesive elements used for this thesis were three-dimensional, therefore a three-dimensional part was created to represent the geometry of the bond. A part was created where the modeling space was "3D," the type was "Deformable," and the base features were the "Solid" shape and the "Extrusion" type. First, a rectangle was drawn whose length and width matched that of the bond, then the thickness of the bond was assigned by entering 0.1 for the depth parameter. When assigning the thickness, a value no smaller than $10^{-4}$ should be used to help avoid numerical errors [Abaqus, 2014]. When assuming that the delamination has no spatial extent, as was also assumed with VCCT, the thickness that should be used for the bond is 0. The thickness of the actual cohesive elements was manually set to 0 in the mesh module (see Section 3.4.7), but the part thickness was set to 0.1 such that the the thickness was visible in the viewer to aid in specimen assembly, which is described in Section 3.4.3.

### *3.4.2 Property*

For the sublaminate, the material properties were created and assigned to the sublaminate part in the same way as the VCCT model (see Section 3.2.2). For the bond, the constitutive response is defined using a traction-separation description. This definition of constitutive response is appropriate for bonded interfaces where the interface thickness is negligibly small, and as such it is appropriate for modeling delamination at interfaces in composites [Abaqus, 2014]. Abaqus offers alternate definitions for the constitutive response of cohesive elements which include a continuum description, and a uniaxial stress state. The continuum approach is appropriate for when the adhesive layer has a finite thickness and macroscopic properties, and the uniaxial stress state is appropriate for modeling things like gaskets or laterally unconstrained adhesive patches.

A material was created for the bond where "Elastic" material behavior was added with the type as "Traction," and the three penalty stiffnesses for the three modes of fracture were entered. The "Quads Damage" (quadratic stress failure criterion) was added, and the three interface strengths for the three modes of fracture were entered. The damage evolution was defined by selecting the type as "Energy," the softening as "Linear," the degradation as "Maximum," the mixed mode behavior as "BK," and the mode mix ratio as "Energy." The critical strain energy release rates were then entered for the three modes of fracture. The BK exponent was set to 1, as was done for the VCCT model and by [Lin, 2017].

To assign the traction-separation constitutive response to the bond part previously created, a section of type "Cohesive" was created. The traction-separation law was selected as the material, and the response was set to "Traction Separation." The analysis default was left for the initial thickness. The initial thickness is what Abaqus calls the constitutive thickness. Although the cohesive elements had zero thickness, the default value for constitutive thickness of 1.0 should be kept because this allows Abaqus to convert the traction-separation law into a stress-strain relationship. Finally, the cohesive section was assigned to the part by selecting the bond part as the region.

### *3.4.3 Assembly*

Similar to the VCCT model assembly (see Section 3.2.3), two instances of the sublaminate were created from the sublaminate part, but for the CZM the "Dependent" mesh option was used. One bond instance was created from the bond part, also with a "Dependent" mesh. The three instances were then translated and rotated such that the bond was sandwiched between the two sublaminate instances, and the sublaminates were arranged such that the thicknesses extruded outward from the bond, as shown in Figure 3.5. It was useful here to be able to see the thickness of the bond in the viewer. Like the VCCT model assembly, the three instances were arranged such that the sublaminate instances laid in the $xy$-plane, and the thicknesses extruded in the positive $z$-direction for the top sublaminate, and in the negative $z$-direction for the bottom sublaminate.

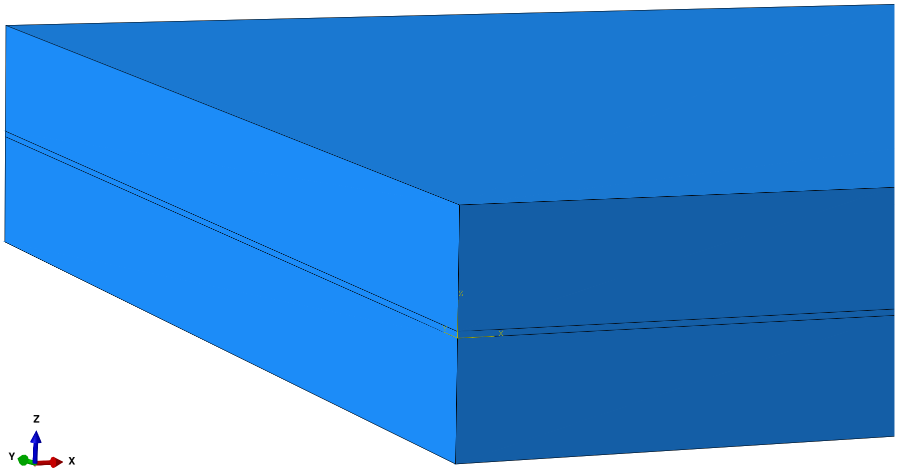

Figure 3.5: Sublaminate and bond assembly with shell thickness rendered

### *3.4.4 Step*

A static step was created similarly to Section 3.2.4. Again, a large-displacement formulation was used by turning the nonlinear geometry on, the maximum number of increments was set to $10^6$, the minimum increment size was set to $10^{-300}$, and the initial increment size and maximum increment size were set to 0.1. Problems with material nonlinearity are typically associated with nonsymmetric Jacobian matrices, therefore the unsymmetric matrix solver was turned on by selecting "Unsymmetric" for matrix storage. The force and displacement at the load application point were requested by modifying the history output requests in the same way to Section 3.2.4.

Materials that exhibit softening behavior, such as the traction-separation response used for this thesis, often have convergence difficulties [Abaqus, 2014]. Automatic stabilization is an option that Abaqus offers for assisting convergence on problems with material instability, and it is established in the step module. With automatic stabilization, when an increment exhibits instability a quasi-static procedure is triggered, where a damping factor is defined (either by the user or by Abaqus default), and viscous forces are added to the global equilibrium equations to achieve a converged solution, where the viscous forces ensure that accelerations are negligible. The automatic stabilization option was not chosen for this thesis; instead viscous regularization was used for stabilization, which is discussed in Section 3.4.7.

### *3.4.5 Interaction*

To represent the contact between the unbonded faces of the two sublaminates, a hard interaction was created in the same way to Section 3.2.6 to prevent the interpenetration of the two sublaminates.

For cohesive zone models, typically it is desirable for the bond to have a much finer mesh that the sublaminates. A relatively coarse mesh can be used for the sublaminates to obtain accurate simulation results in bending, while a relatively fine mesh is needed for the bond, both to more accurately capture the crack front advance, and to more accurately describe stresses at the crack front and at the interface between the two sublaminates. Due to these disparate meshing needs, constraints were created between the sublaminates and bond so that the meshes did not have to match. A constraint of type "Tie" was created for each of the sublaminate-bond surface pairs (the top surface of the bond and the inner surface of the top sublaminate, and the bottom surface of the bond and the inner surface of the bottom sublaminate). Each tie was created by selecting a sublaminate as the master surface, and the adjacent bond surface as the slave surface. The master surface should be larger and stiffer than the slave surface when considering this assignment, as the slave surfaces are restricted in their deformation according to the deformation of the master surface.

### *3.4.6 Load*

The displacement controlled loading and the fixed end boundary conditions were created similarly to the VCCT model (see Section 3.2.7), except when creating the fixed end boundary condition, care was taken to ensure that in addition to the two edges of the top and bottom sublaminates, the face of the bond instance at the fixed end was also included in the region over which to apply this boundary condition.

### *3.4.7 Mesh*

Similar to the VCCT model (see Section 3.2.5), the sublaminates should have identical meshes. Since the mesh was set to "Dependent" in the assembly module, this was achieved by meshing the sublaminate part, as opposed to the sublaminate instances. The part was seeded, then meshed, and the "S4" element was chosen. By meshing the part, both instances automatically had this same mesh since their mesh was dependent on the part.

The cohesive element orientation must be defined in the thickness direction. This was achieved by assigning mesh controls. The "Sweep" technique was used with the "Advancing front" algorithm, and the sweep path was defined such that the vector shown in the viewport pointed in the thickness direction of the bond (in the $z$-direction). The part was seeded, then meshed, and the eight-node three-dimensional cohesive element "COH3D8" was chosen.

As mentioned in the step module section (see Section 3.4.4), material models exhibiting softening cause serious convergence issues. This was addressed by using viscous regularization, which involves assigning a viscosity to the cohesive elements. The viscosity should be a small number such that the effect on the simulation results is negligible. Unlike automatic stabilization, which adds viscous forces to the global equilibrium equations, viscous regularization introduces localized damping to reach a converged solution [Abaqus, 2014]. The viscosity value used was $10^{-6}$, as this was found to have a negligible effect on results, where for values larger than this the force-displacement curve exhibited over-softening behavior.

At this point, the entire model was meshed, but the cohesive elements still had a thickness of 0.1 which matched the thickness of the bond part. The thickness was manually zeroed by first changing the instances from "Dependent" to "Independent" in the assembly module, then moving one of the sublaminate-bond pairs of nodes to match the other. The "Edit Mesh" tool was used with the "Edit" method and the "Node" category, and the nodes from the top sublaminate-bond pair were selected. The "Project to geometry" was turned off, and an offset of $-0.1$ in the $z$-direction was entered. The result of this mesh edit is shown in Figure 3.6.

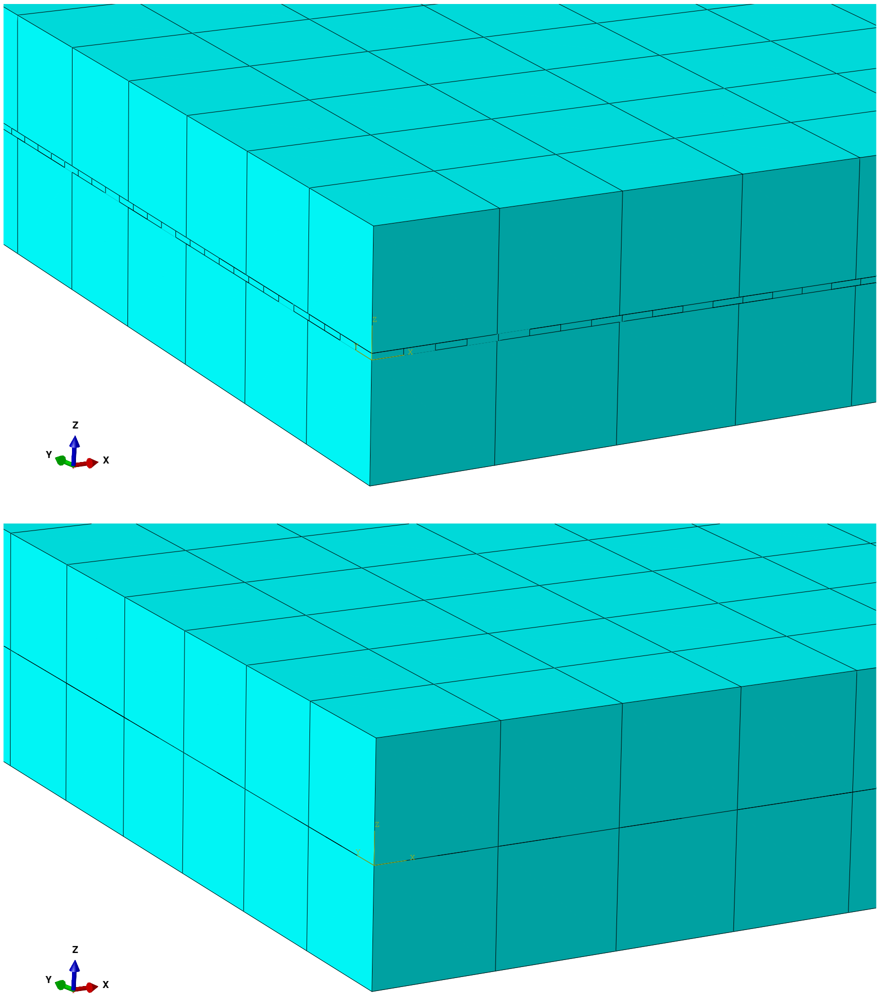

Figure 3.6: Mesh before zeroing cohesive element thickness (top), and after (bottom)

# Chapter 4

# DETERMINATION OF MATERIAL PROPERTIES

This chapter discusses the determination of the mechanical and fracture material parameters of the composite material used for this thesis, which are used in the Abaqus simulations. The experimental force-displacement data was used to directly determine $E_1$ as well as $G_{IIC}$, and the remaining material properties were either obtained from the manufacturer's data sheet, or were obtained empirically. There is currently no existing ASTM standard for determining the flexural modulus (which is assumed to be the same as $E_1$ for this thesis) from a cantilever beam test, therefore the same theory used in the ASTM standard for determining flexural modulus from the three-point bending test was used to determine the flexural modulus for the cantilever test. The mode II critical strain energy release rates were determined using the beam theory method, as discussed previously in Section 2.4. Furthermore, the mode II critical strain energy release rates are compared between different geometries and different specimens to investigate size effects. The $R$-curve is also established to investigate the crack growth initiation and propagation values of $G_{IIC}$, and the implications that these results have on the validity of the analyses done for this thesis are discussed.

## *4.1 Mechanical Properties*

Since the Abaqus models for this thesis used elements with a plane stress formulation to represent the sublaminates, and the material properties were entered using the "Lamina" option, the mechanical material properties needed were $E_1$, $E_2$, $\nu_{12}$, $G_{12}$, $G_{13}$, and $G_{23}$. From classical laminate theory, the plane stress condition requires only $E_1$, $E_2$, $\nu_{12}$, and $G_{12}$ to determine the constitutive law for a laminate, but $G_{13}$ and $G_{23}$ are included as they may be required for modeling transverse shear deformation in a shell element [Abaqus, 2014]. This section discusses how these material properties were determined.

### *4.1.1 Local 1-Direction Elastic Modulus*

The most critical mechanical material property is $E_1$, as it controls the deflection, and is used to determine $G_{IIC}$ as discussed later in Section 4.2.1. From the experimental tests done for this thesis, only the flexural modulus in the 1-direction could be calculated from the force-displacement data. Currently, the three-point bending test for determining the flexural modulus of polymer matrix composites is standardized by ASTM D7264, while the cantilever test is not standardized by ASTM. Furthermore, since the specimens tested for this thesis were unidirectional and transversely isotropic, it was assumed that the flexural modulus would correlate with the elastic modulus in the 1-direction. Therefore, the same theory was used to determine $E_1$ for the ELS specimens as was used in ASTM D7264.

The three-point bending standard offers two methods for calculating flexural modulus: (1) the flexural chord modulus of elasticity, and (2) the flexural secant modulus of elasticity. To determine the flexural chord modulus of elasticity, the flexural stress and strain are calculated by

$$\sigma = \frac{3PL}{2bh^2}, \qquad \varepsilon = \frac{6\delta h}{L^2}$$

where $P$ is the applied load at any point on the force-displacement curve, $\delta$ is the displacement at the load application point corresponding to $P$, $L$ is the total length of the beam (the distance between the two support points or rollers), $b$ is the width of the beam, and $h$ is the total thickness of the beam [ASTM, 2015]. These equations are derived using Euler-Bernoulli beam theory for the three-point bending test, and are the stress and strain at the extreme fibers. The stress and strain are then used to calculate the flexural chord modulus as

$$E_{chord} = \frac{\Delta\sigma}{\Delta\varepsilon}.$$

Alternatively, the flexural secant modulus is determined by

$$E_{secant} = \frac{L^3 m}{4bh^3}$$

where $m$ is the slope of the secant of the force-displacement curve, and $L$, $b$, and $h$ are defined as above [ASTM, 2015].

The same principles employed for these three-point bending modulus equations were used to derive the moduli for the cantilever test. For the flexural chord modulus, the maximum bending stress and strain of a cantilever beam are given by

$$\sigma \;=\; \frac{My}{I} \;=\; \frac{(PL)(\frac{h}{2})}{\frac{bh^3}{12}} \;=\; \frac{6PL}{bh^2},$$

$$\varepsilon \;=\; yv'' \;=\; \left(\frac{h}{2}\right)\left(\frac{M}{EI}\right) \;=\; \left(\frac{h}{2}\right)\left(\frac{PL}{EI}\right) \;=\; \left(\frac{h}{2}\right)\left(\frac{L}{EI}\right)\left(\frac{3EI\delta}{L^3}\right) \;=\; \frac{3\delta h}{2L^2}$$

where $L$ is the total length of the beam (the distance between the fixed end and the load application point), and $P$, $\delta$, $b$, and $h$ are defined as above. The flexural chord modulus is then calculated using the same equation as above. For the flexural secant modulus, the slope of the force-displacement curve for a cantilever beam is given by

$$m \;=\; \frac{dP}{d\delta} \;=\; \frac{3EI}{L^3}.$$

Therefore, the flexural secant modulus is calculated by

$$E_{secant} = \frac{4L^3 m}{bh^3}.$$

Notice that plugging $m$ into this equation gives

$$E_{secant} \;=\; \left(\frac{4L^3}{bh^3}\right)\left(\frac{3E(\frac{bh^3}{12})}{L^3}\right) \;=\; E.$$

The ASTM D7264 standard recommends using strain points in the range 0.001-0.003 for the flexural chord modulus, and the secant modulus is the same as the chord modulus except the initial strain point is zero. Due to the initial nonlinearity of the force-displacement curves from the cantilever pristine beam tests due to the imperfection of the clamped end, the last 20% of the force-displacement data was used to calculate the moduli instead of the ASTM recommended data ranges. Furthermore, a linear least squares fit was used for this data set rather than only the end points. When using the same data set, identical moduli are yielded for both the chord and secant modulus methods. The elastic moduli for the ELS specimens calculated using this procedure are shown in Table 4.1, and for the Abaqus results shown in Chapter 5 the modulus specific to each specimen was used for the modeling of that specimen.

Table 4.1: ELS Specimen Elastic Moduli

| Thickness [mm] | Free Length [mm] | Specimen Number | $E_1$ [N/mm$^2$] |
|---|---|---|---|
| 8 | 100 | 2 | 77100 |
| 8 | 100 | 3 | 79300 |
| 4 | 100 | 6 | 101000 |
| 4 | 50 | 1 | 76600 |
| 4 | 50 | 3 | 77600 |

To maintain consistency with the method used for the ELS specimen, the ENF specimen $E_1$ determination also used a linear least squares fit of the data, but with the last 25% of the data since the force-displacement curves exhibited less initial nonlinearity due to the supports. These elastic moduli are shown in Table 4.2.

As expected, as was mentioned in Section 2.1, the ELS specimen gives smaller values for elastic modulus than the ENF specimen, which matches the findings of Blackman et al. [2006]. Furthermore, even for the ENF specimen the modulus values were on average lower than the value given by the manufacturer's data sheet, which is 125000 N/mm$^2$. This could be due to the fact that the manufacturer used ASTM D3039 (the standard test method for

Table 4.2: ENF Specimen Elastic Moduli

| Thickness [mm] | Free Length [mm] | Specimen Number | $E_1$ [N/mm$^2$] |
|---|---|---|---|
| 8 | 100 | 4 | 121000 |
| 8 | 100 | 6 | 120000 |
| 8 | 100 | 5 | 119000 |
| 8 | 100 | 3 | 119000 |
| 8 | 100 | 2 | 118000 |
| 4 | 50 | 5 | 123000 |
| 4 | 50 | 6 | 135000 |
| 4 | 50 | 3 | 124000 |
| 4 | 50 | 1 | 127000 |
| 4 | 50 | 4 | 122000 |

tensile properties of polymer matrix composites) to determine the elastic modulus rather than ASTM D7264, the age of the composite, the storage conditions, the fabrication and curing process, or a combination of these factors. These $E_1$ results also reveal issues related to geometric irregularity and the repeatability of the clamped end for the cantilever test, where the ELS specimens with similar thickness to free length ratios (8 mm thickness and 100 mm free length, and 4 mm thickness and 50 mm free length) had similar $E_1$ values which were lower than the specimen with 4 mm thickness and 100 mm free length. Furthermore, the ENF specimens with 8 mm thickness and 100 mm free length had lower $E_1$ values than the specimens with 4 mm thickness and 50 mm free length.

### *4.1.2 Other Mechanical Properties*

For the remaining material properties required for Abaqus, the manufacturer's data sheet was used. The manufacturer's data sheet for the material used for this thesis lists several mechanical properties including the 0° tensile modulus ($E_{1t}$), the 0° compressive modulus ($E_{1c}$), the 90° tensile modulus ($E_{2t}$), the 90° compressive modulus ($E_{2c}$), the in-plane shear modulus ($G_{12}$), and Poisson's ratio ($\nu_{12}$), as shown in Table 4.3. For the Abaqus input $E_2$, the manufacturer's data sheet value for $E_{2t}$ was used. For the Abaqus inputs $G_{12}$ and $\nu_{12}$, the $G_{12}$ and $\nu_{12}$ values from the manufacturer's data sheet were used. Since it was assumed that the laminates were transversely isotropic, the $G_{12}$ value from the manufacturer's data sheet was used for the Abaqus input $G_{13}$. Finally, the $G_{12}$ value from the manufacturer's data sheet was also used for the Abaqus input $G_{23}$.

Table 4.3: Mechanical Properties of P707AG-15 [Toray Composites America, Inc., 2018a]

| Property | Value | Units |
|---|---|---|
| $E_{1t}$ | 125000 | N/mm$^2$ |
| $E_{1c}$ | 112000 | N/mm$^2$ |
| $E_{2t}$ | 8410 | N/mm$^2$ |
| $E_{2c}$ | 8480 | N/mm$^2$ |
| $G_{12}$ | 4230 | N/mm$^2$ |
| $\nu_{12}$ | 0.31 | – |

## *4.2 Fracture Properties*

Since both the VCCT and the CZM methods were used to simulate delamination propagation for this thesis, the required fracture properties were the critical strain energy release rates, the interfacial strengths, and the penalty stiffnesses for all three modes of fracture. From the experimental test data, only the mode II critical strain energy release rate could be directly determined. Therefore, this section discusses how the $G_{IIC}$ values were calculated, and how the remaining fracture material properties were determined.

### *4.2.1 Mode II Critical Strain Energy Release Rate ($G_{IIC}$)*

The first attempt to model the ELS specimens in Abaqus using the assumed crack lengths from Table 2.1, and the $G_{IIC}$ values obtained from the compliance calibration and beam theory methods, as described in Section 2.4, revealed a significant disparity between the force-displacement responses from the experimental tests and the numerical models. The most apparent disparity was the force-displacement response prior to crack propagation, where the compliance of the numerical models did not match the compliance of the experimental tests. The close match between the pristine beam force-displacement results in terms of compliance from the experimental tests and numerical models (see Section 5.1) suggested that there was an error in the assumed crack lengths, and hence an error in the calculated $G_{IIC}$ values from both the compliance calibration and beam theory methods. Furthermore, comparisons of the force-displacement curves for all tests for each specimen also revealed variation in the initial crack lengths during testing, as shown in Figure 4.1. This could have been caused by a misidentification of the exact location of the Teflon insert, or the crack length determined by equation (2.1) after the NPC test was inaccurate, or a combination of these factors. After the NPC tests, the crack calculations gave crack lengths that extended slightly past the fixed end for all the ELS specimens. During testing, it was assumed that this was an error, and that the actual crack tip was at the fixed end. Both the repeatability of the PC tests, and the reduced stiffnesses of the PC tests compared to the NPC tests for all ELS specimens, as shown in Figure 4.1, indicated that this assumption was incorrect. Therefore, it was necessary to recalculate the crack lengths, and the critical strain energy release rates, which was done using the beam theory method.

To solve the fracture crack length for the ELS specimen using the beam theory method, the compliance (see Appendix A) was rearranged to solve for the crack length

$$a_{ELS} = \left(\frac{24EIC - L^3}{3}\right)^{1/3} \tag{4.1}$$

where $E = E_1$, and $C$ is the loading compliance of the beam from the fracture test as

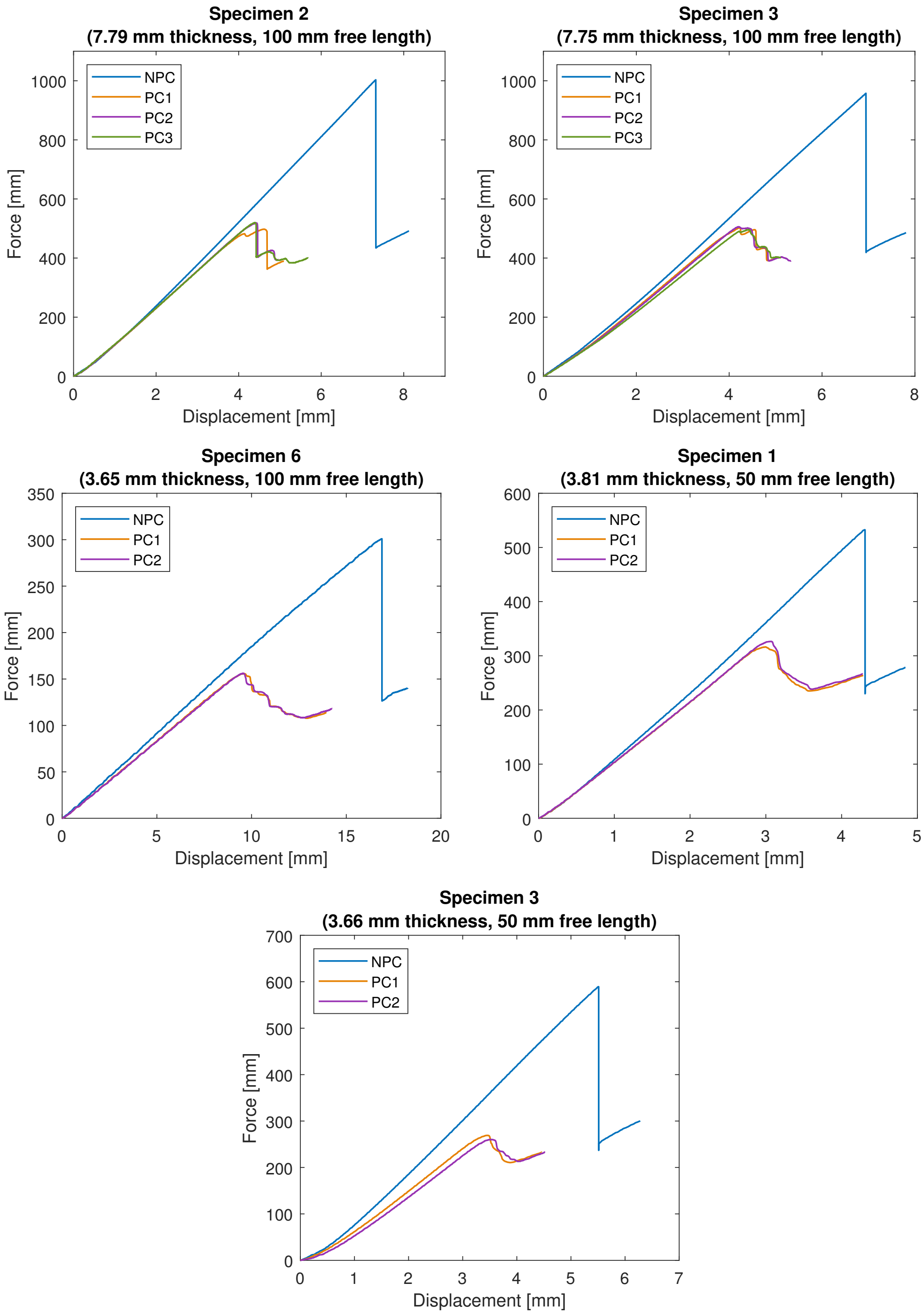

Specimen 2
(7.79 mm thickness, 100 mm free length)

Specimen 3
(7.75 mm thickness, 100 mm free length)

Specimen 6
(3.65 mm thickness, 100 mm free length)

Specimen 1
(3.81 mm thickness, 50 mm free length)

Specimen 3
(3.66 mm thickness, 50 mm free length)

Figure 4.1: Experimental force-displacement curves for the ELS specimens

described in Section 2.4. The mode II critical strain energy release rate was then calculated by

$$G_{IIC,ELS} = \frac{9P_{max}^2 a_{ELS}^2}{4EB^2h^3}. \tag{4.2}$$

Both the fracture crack length and the mode II critical strain energy release rates were calculated for each test for each specimen (one NPC test, and at least one PC test). Then, the initial fracture crack length and $G_{IIC}$ were averaged for the PC tests to obtain one value for crack length and one value for $G_{IIC}$ for both the NPC and PC tests for each specimen. The PC values were averaged for both the initial crack length and $G_{IIC}$ to serve as Abaqus inputs. These values are shown in Table 4.4.

Table 4.4: Fracture Crack Lengths ($a$), and Mode II Critical Strain Energy Release Rates ($G_{IIC}$) for the ELS Specimens

| Specimen Number | $a_{NPC}$ [mm] | $G_{IIC,NPC}$ $\left[\frac{\text{N}\cdot\text{mm}}{\text{mm}^2}\right]$ | $a_{PC}$ [mm] | $G_{IIC,PC}$ $\left[\frac{\text{N}\cdot\text{mm}}{\text{mm}^2}\right]$ |
|---|---|---|---|---|
| 2 | 56.78 | 2.904 | 62.46 | 0.916 |
| 3 | 57.46 | 2.680 | 63.55 | 0.898 |
| 6 | 54.93 | 1.914 | 60.14 | 0.615 |
| 1 | 28.36 | 1.929 | 30.98 | 0.838 |
| 3 | 28.16 | 2.494 | 34.66 | 0.761 |

A similar procedure was used for the beam theory method for the ENF specimen, where the fracture crack length was calculated by

$$a_{ENF} = \left(\frac{96EIC - 2L^3}{3}\right)^{1/3},$$

and the mode II critical strain energy release rate was calculated using

$$G_{IIC,ENF} = \frac{9P_{max}^2 a_{ENF}^2}{16EB^2h^3}.$$

These values are shown in Table 4.5.

The manufacturer's data sheet reports a $G_{IIC}$ of 0.998 N·mm/mm$^2$, which is higher than any $G_{IIC}$ obtained from the experimental tests done for this thesis. The manufacturer reports higher material property values for both $E_1$ and $G_{IIC}$ compared to the values obtained experimentally, and as discussed in Section 4.1.1, this could be due to a variety of factors including the test standard used to determine the material property, the age of the composite, the storage conditions, and the fabrication and curing process.

Table 4.5: Fracture Crack Lengths ($a$), and Mode II Critical Strain Energy Release Rates ($G_{IIC}$) for the ENF Specimens

| Specimen Number | $a_{NPC}$ [mm] | $G_{IIC,NPC}$ $\left[\frac{\text{N·mm}}{\text{mm}^2}\right]$ | $a_{PC}$ [mm] | $G_{IIC,PC}$ $\left[\frac{\text{N·mm}}{\text{mm}^2}\right]$ |
|---|---|---|---|---|
| 4 | 63.18 | 1.778 | 73.88 | 0.847 |
| 6 | 65.95 | 2.362 | 82.37 | 0.767 |
| 5 | 64.07 | 2.081 | 80.19 | 0.865 |
| 3 | 68.59 | 2.429 | 86.73 | 0.813 |
| 2 | 66.55 | 2.264 | 83.28 | 0.795 |
| 5 | 32.44 | 1.409 | 35.72 | 0.771 |
| 6 | 30.86 | 2.040 | 36.74 | 0.780 |
| 3 | 31.33 | 1.799 | 37.07 | 0.667 |
| 1 | 30.94 | 1.528 | 38.04 | 0.666 |
| 4 | 33.53 | 1.441 | 38.14 | 0.701 |

### *4.2.2 Mode I and Mode III Critical Strain Energy Release Rates*

For many composites, the mode II critical strain energy release rate is considerably higher than that of mode I [Tay, 2003]. The manufacturer's data sheet for the prepreg used for this thesis provides a $G_{IC}$ of 0.333 N·mm/mm$^2$, which is lower than both the $G_{IIC}$ value reported by the manufacturer and the values obtained from experimental testing [Toray Composites America, Inc., 2018b]. Consequently, this value was used for the mode I critical strain energy release rate. The mode III critical strain energy release rate value was set equal to mode II, as was done by Song et al. [2008] who used this $G_{IIIC}$ designation to simulate in Abaqus mode I fracture using a double cantilever beam (DCB) specimen model, mode II fracture using an ENF specimen model, and mixed-mode fracture using a mixed-mode bending (MMB) specimen model.

### *4.2.3 Interfacial Strength*

The manufacturer's data sheet provides a shear strength of 86.2 N/mm$^2$, which was determined using ASTM D2344, the standard for short-beam shear strength of polymer matrix composite materials. This standard uses a beam with a high thickness to length ratio to determine the shear strength of the material, where the mode of failure is mid-plane interlaminar failure [ASTM, 2016]. The ASTM D2344 standard was used by Zhu et al. [2007], Costa et al. [2001], and Tsenoglou et al. [2006] to determine the interlaminar shear strength of their fiber-matrix composite materials. Therefore, 86.2 N/mm$^2$ was accepted as the interfacial strength of the material used for this thesis, and was used for the numerical modeling of all specimens for all three modes of fracture.

To serve as a comparison to this manufacturer obtained value, a method for estimating the interface strength proposed by Turon et al. [2007] was explored. This method is based on the relationship between yield stress and plastic zone size, as described in Section 1.5.6. The plastic zone size estimates provided in Table 1.1 all follow the form

$$r_p = M\left(\frac{K_{IIC}}{\tau_y}\right)^2$$

where $r_p$ is the plastic zone size, $K_{IIC}$ is the mode II critical stress intensity factor, $\tau_y$ is the yield stress, and $M$ is the coefficient of the plastic zone size. For example, $M$ for Rice's model is $\frac{9\pi}{32}$, and for Hillerborg's model is 1. The cohesive zone size $l_{cz}$ is the same as the plastic zone size $r_p$, and Turon et al. [2007] defined $l_{cz} = N_e l_e$ where $N_e$ is the number of elements within the cohesive zone, and $l_e$ is the length of the cohesive elements. Therefore, by rearranging the plastic zone size equation to solve for the yield stress (interface strength), and recalling the relationship between $K_{IIC}$ and $G_{IIC}$ from Section 1.5.4, an estimate for the interface strength for mode II fracture is obtained by

$$T^{\circ} = \sqrt{\frac{MEG_{IIC}}{N_e l_e}}.$$

Song et al. [2008] and Turon et al. [2007] obtained reasonable force-displacement results using this method with $M = 1$ and $M = \frac{9\pi}{32}$, respectively, and $E = E_2$. For this thesis, three ELS specimens were modeled in Abaqus, and the interface strength values obtained for each specimen using this method with $M = 1$, $E = E_2$, $N_e = 5$, and $l_e = 0.5$ mm are presented in Table 4.6. These values are lower than the manufacturer provided value, and the numerical models using these interface strengths (assuming identical interface strengths for all three modes of fracture) underpredicted the peak force in the force-displacement response when compared to the experimental test data. Therefore, the numerical model results shown in Chapter 5 for these three specimens use the manufacturer provided value for interface strength.

Table 4.6: Interface Strengths ($T^{\circ}$) Obtained Using the Method Proposed by Turon et al. [2007]

| Thickness [mm] | Length [mm] | Specimen Number | $T^{\circ}$ [N/mm$^2$] |
|---|---|---|---|
| 8 | 100 | 3 | 54.96 |
| 4 | 100 | 6 | 45.48 |
| 4 | 50 | 1 | 53.09 |

### *4.2.4 Penalty Stiffness*

It was not possible to determine the penalty stiffness $K$ from the experimental test data, and $K$ is not provided by the manufacturer, therefore a method for estimating $K$ was tried, but ultimately the $K$ values used for numerical modeling results shown in Chapter 5 were determined empirically. A penalty stiffness that is too large could result in numerical problems that lead to convergence issues such as spurious oscillations of the tractions, therefore the stiffness should be large enough to provide a reasonable representation of the predamaged stiffness, but small enough to reduce the risk of numerical problems [Turon et al., 2007]. To meet this consideration, Turon et al. [2007] proposed a method for estimating the penalty stiffness for mode I fracture given by

$$K = \frac{\alpha E_3}{t}$$

where $\alpha$ is a parameter much larger than 1 ($\alpha$ values greater than 50 are sufficient for most problems), $E_3$ is the elastic modulus in the 3-direction, and $t$ is the thickness of the adjacent sublaminate. Song et al. [2008] obtained good results when using this method to model mode I, mode II, and mixed mode fracture in Abaqus assuming $K$ is identical for all three modes of fracture. For this thesis, three ELS specimens were modeled in Abaqus using the same $K$ for all three modes of fracture calculated using $\alpha = 50$, $E_3 = E_2$, and $t$ is half the total beam thickness. The $K$ values that were used are presented in Table 4.7, and the resulting numerical model force-displacement responses were oversoftened compared to the experimental test data. Therefore, the penalty stiffnesses were obtained empirically.

Table 4.7: Penalty Stiffnesses ($K$) Obtained Using the Method Proposed by Turon et al. [2007]

| Thickness [mm] | Length [mm] | Specimen Number | $K$ [N/mm$^3$] |
|---|---|---|---|
| 8 | 100 | 3 | 109000 |
| 4 | 100 | 6 | 230000 |
| 4 | 50 | 1 | 221000 |

Penalty stiffness values that were approximately 10 times larger than the $E_1$ values gave force-displacement simulation results which compared well with the experimental tests, and were therefore used for all three modes of fracture for each specimen. The penalty stiffness values used to obtain the results shown in Chapter 5 are provided in Table 4.8. Values as small as the ones presented in Table 4.7 gave softened force-displacement responses, and penalty stiffnesses larger than those presented in Table 4.8 sometimes prevented the simulations from converging.

Table 4.8: Empirically Obtained Penalty Stiffnesses ($K$)

| Thickness [mm] | Length [mm] | Specimen Number | $K$ [N/mm$^3$] |
|---|---|---|---|
| 8 | 100 | 3 | 800000 |
| 4 | 100 | 6 | 1000000 |
| 4 | 50 | 1 | 800000 |

## *4.3 Size Effects on Experimentally Obtained $G_{IIC}$*

The critical strain energy release rate is considered to be a material property, and therefore should be independent of geometry. Verifying that $G_{IIC}$ values are independent of specimen geometry includes not only evaluating different types of specimens and the influence of loading fixtures, but also examining the influence of width, length, and thickness [Davies et al., 2001]. This section explores the effects that different specimens (ENF and ELS), and geometries (lengths and thicknesses) have on $G_{IIC}$.

To investigate thickness effects, the approximately 8 mm thick with 100 mm free length, and the approximately 4 mm thick with 50 mm free length ELS and ENF specimen $G_{IIC}$ values were compared, as shown in Figure 4.2. The $G_{IIC}$ value for each test is shown in this plot (all the $G_{IIC,PC}$ values are plotted, rather than just the average for each specimen). These two specimen geometries were compared for thickness effects since they have identical thickness to free length ratios, as well as identical initial crack length to free length ratios. On average, the ELS specimens give higher $G_{IIC}$ values than the ENF specimens, and on average, the approximately 8 mm thick specimens give higher $G_{IIC}$ values than the approximately 4 mm thick specimens.

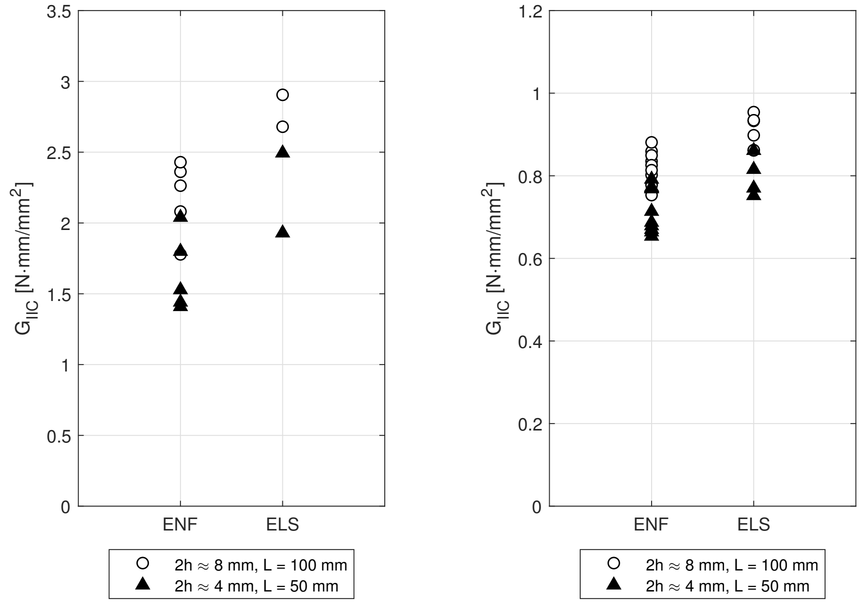

Figure 4.2: Comparison of $G_{IIC,NPC}$ (left) and $G_{IIC,PC}$ (right) between thicknesses (4 mm, 8 mm) and specimens (ENF, ELS)

To investigate length effects, the approximately 4 mm thick with 100 mm free length, and the approximately 4 mm thick with 50 mm free length ELS specimen $G_{IIC}$ values were compared, as shown in Figure 4.3. Both of these specimen geometries had identical initial crack length to free length ratios. A comparison between specimens for the length effects was not possible since no ENF specimen tests were performed with a 4 mm approximate thickness and 100 mm free length. On average, the 50 mm free length specimens give higher $G_{IIC}$ values than the 100 mm free length specimens, for both the NPC and the PC tests. For this comparison, only one specimen had a 100 mm free length, while two specimens had a 50 mm free length, therefore this comparison is less conclusive than the thickness effects comparison. However, two PC tests were performed for the 100 mm free length specimen, and both $G_{IIC}$ values obtained from these tests were lower than the $G_{IIC}$ values obtained from the 50 mm length specimens.

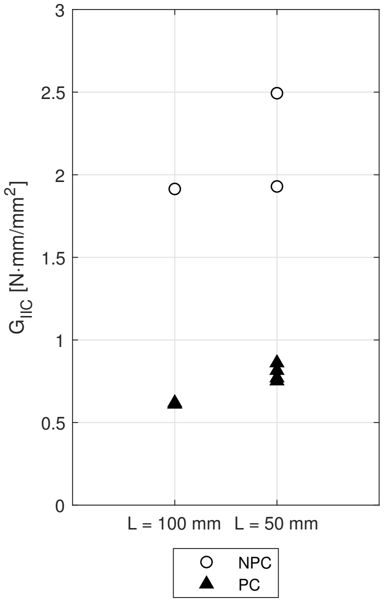

Figure 4.3: Comparison of $G_{IIC}$ between tests (NPC, PC) and lengths (50 mm, 100 mm) for the approximately 4 mm thick ELS specimens

The observations from these investigations of geometry effects likely imply that friction on the post fractured plane has an effect on $G_{IIC}$. The higher $G_{IIC}$ values for the thicker specimens compared to the thinner specimens, for the ELS specimens compared to the ENF specimens, and for the shorter specimens compared to the longer specimens are all associated with higher peak loads, and consequently higher shear forces, and hence higher friction. The higher $G_{IIC}$ values for the NPC tests compared to the PC tests do not imply higher friction, rather the disparity between these values is due to the higher energy required to initiate crack growth from a blunted crack tip as opposed to a sharp crack tip.

## 4.4 *R-Curve*

The $R$-curve was introduced in Section 1.5.5 to describe the relationship between critical strain energy release rate and crack length, where brittle materials exhibit a flat $R$-curve, and ductile materials exhibit a rising $R$-curve. This section discusses how the $R$-curve was established from the experimental test data, and investigates the implications that the $R$-curve has on the validity of the data analysis done for this thesis.

To develop the $R$-curve from the experimental data, both the crack length and the mode II critical strain energy release rate were calculated. The crack length calculations as described in Section 4.2.1 for the initial fracture crack length depended on a compliance which was determined by a linear least squares fit of the force-displacement data. During crack propagation, it is not possible to determine compliance using a linear least squares regression analysis, therefore the crack length was estimated using equation (4.1) with a compliance calculated by

$$C = \frac{\delta_i}{P_i}$$

where $\delta_i$ and $P_i$ are the displacement and load, respectively, for any data point on the loading force-displacement curve after crack growth has been initiated. Using this crack length, the mode II critical strain energy release rate was then calculated using equation (4.2). The $R$-curve was then established for each test for each specimen by plotting the $G_{IIC}$ values against the crack length values, as shown in Figure 4.4. Although the crack lengths, and hence the $G_{IIC}$ values, are not exactly accurate since only an estimation for the compliance was used, this exercise provides useful insight about the general trend of the $R$-curve for the material used for this thesis.

Several important observations can be made from these $R$-curves. The first is that the $R$-curves for all specimens show the instability of the NPC test, as well as the higher crack growth initiation value of $G_{IIC}$ for the NPC test compared to the PC test. Both of these observations are consistent with the expected result, as the NPC test initiates crack growth from a blunted crack tip compared to the PC test. Furthermore, for all PC tests the material exhibits a flat $R$-curve which is consistent with a brittle material. This is an especially important observation since many of the fracture mechanics theories presented in Section 1.5 are based on the assumption that the material is perfectly brittle. Specifically, this

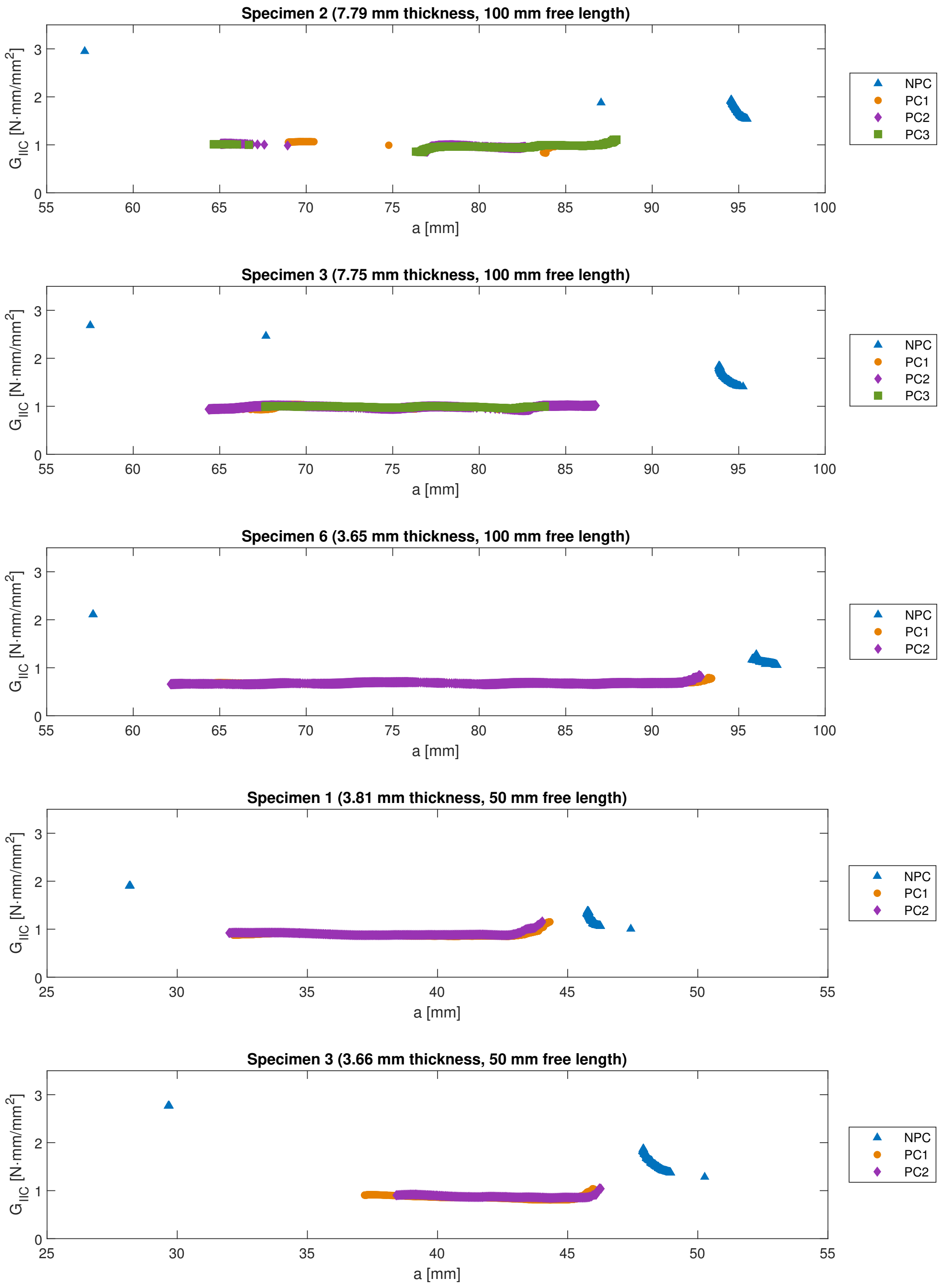

Figure 4.4: *R*-curves for the ELS specimens

observation implies that the use of equation (1.1) to calculate the mode II critical strain energy release rate is appropriate for this thesis since this equation is based on Griffith's theory for strain energy release rate which assumes a perfectly brittle material.

# Chapter 5

# EXPERIMENTAL AND NUMERICAL MODELING FORCE-DISPLACEMENT RESULTS

In this chapter, the experimental and numerically modeled force-displacement results are used to investigate several topics including the validation of the mechanical properties, the capabilities of VCCT and CZM for simulating delamination propagation, as well as their capabilities for handling size effects. The pristine beam experimental and numerical force-displacement results are compared primarily to validate the local 1-direction elastic modulus $E_1$, while the fracture test experimental and numerical force-displacement results are compared to validate the fracture properties and to investigate the suitability of the two crack growth models for simulating mode II delamination propagation for the ELS specimen. This chapter only discusses the PC fracture test results, and not the NPC test results, since the fracture mechanics theories on which the two modeling methods, and the $G_{IIC}$ equation are based, assume an ideally sharp crack. The VCCT and CZM capabilities for handling size effects are investigated by using the most conservative experimentally obtained $G_{IIC}$ value on other specimens. Additionally, the $E_1$ from the specimen with the most conservative $G_{IIC}$ is also used in conjunction with this $G_{IIC}$ to further investigate size effects, as well as the relationship between the two material properties.

## *5.1 Pristine Test*

To verify the mechanical material properties, pristine cantilever beams of three different geometries were modeled: (1) specimen 3, with an approximately 8 mm thickness and a 100 mm free length, (2) specimen 6, with an approximately 4 mm thickness and a 100 mm free length, and (3) specimen 1, with an approximately 4 mm thickness and a 50 mm free length.

These specimens were chosen to investigate size effects, and are the same specimens that were modeled for fracture, which is discussed in Section 5.2.

The pristine beams were modeled using the same methodology as for the VCCT modeling, as discussed in Section 3.2, but without a crack. This was accomplished by selecting all of the nodes on both of the sublaminates to be included in the bonded node set, and increasing the critical strain energy release rates for all three fracture modes to a value of 10, which is too high for crack growth to occur. This unreasonably high value for $G_C$ effectively ensured that the split beam was completely bonded such as to act as a whole beam. The force-displacement results from both the experimental tests and the numerical models are shown in Figure 5.1.

The experimental force-displacement curves exhibit initial nonlinearity due to the imperfection of the clamped end, but reach a relatively constant and stable slope. The numerical models do not have initial nonlinearity, since the clamped end was modeled using perfect fixity of all the displacements and rotations at the fixed end, but the numerical model results compare well with the experimental results after the experimental force-displacement curves overcome the initial nonlinearity. The accuracy of these simulations is dominated by $E_1$, and hence the force-displacement results primarily validate that material property. Potential errors in other properties would require further testing, and the effects on the fracture process due to errors in the mechanical properties requires further exploration.

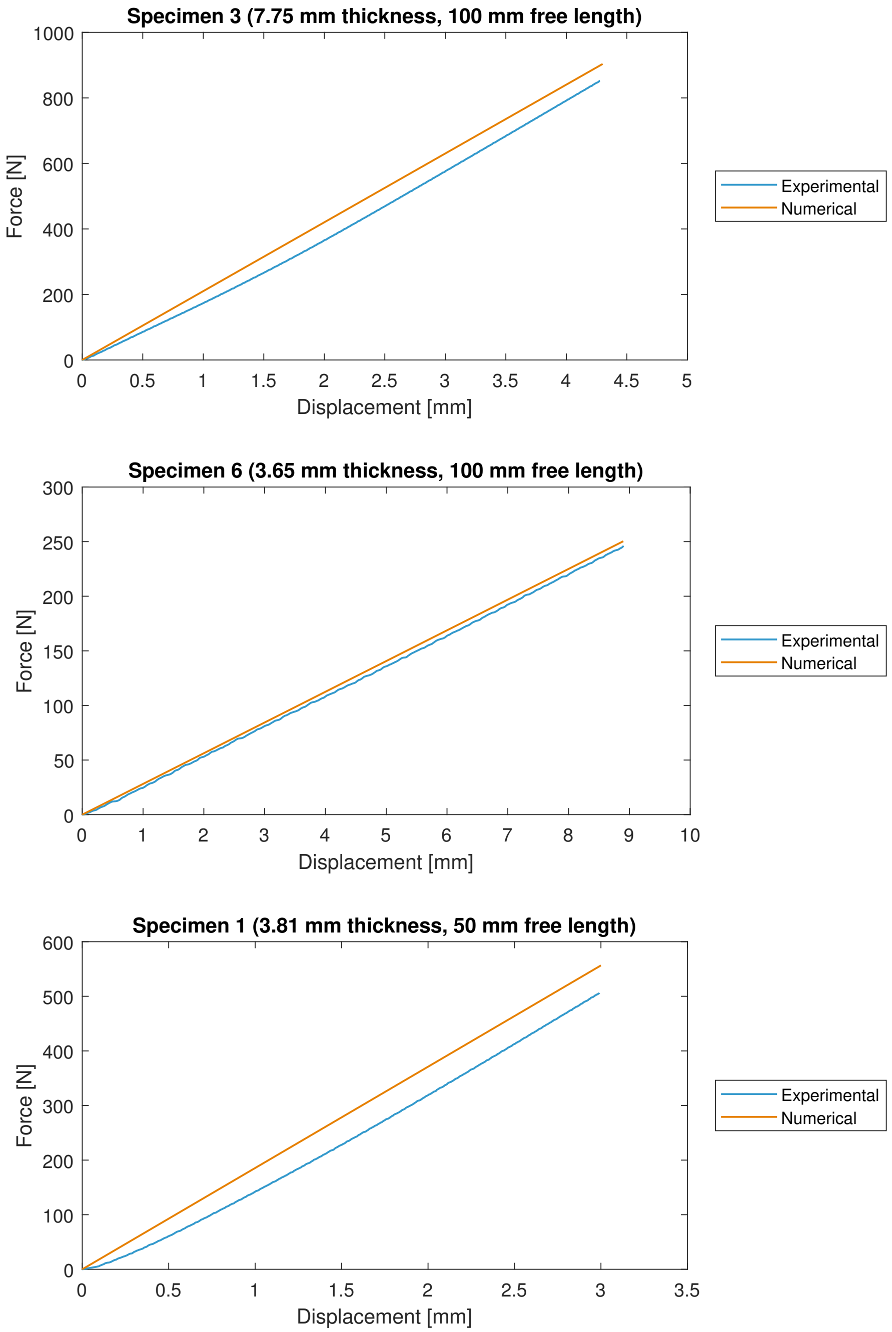

Figure 5.1: Experimental and numerical force-displacement results for the pristine beam cantilever tests

## 5.2 *Fracture Test*

This section provides and discusses the force and displacement results at the load application point for the both the VCCT and CZM Abaqus simulations compared with the experimental test data, as well as the closed form force-displacement solution for the ELS specimen as derived in Appendix B. These results provide insight into both the VCCT and CZM model capabilities for predicting delamination propagation, and for handling size effects.

### *5.2.1 VCCT*

The VCCT models were created for each of the three specimens using the procedure outlined in Section 3.2, the beam geometries provided in Section 2.2, the mechanical properties provided in Section 4.1, and the fracture properties provided in Section 4.2. The force-displacement results from the VCCT simulations are compared to the experimental test data for each of the three selected specimens in Figure 5.2. The approximate global size (AGS) of the shell elements for specimen 3 was set to a value of 4, and for specimens 6 and 1 was set to a value of 2. The AGS determines the approximate element dimensions, where for an AGS of 2 the elements were approximately square shaped with dimensions of approximately 2 mm. The VCCT simulation results compare well with the experimental data for all three of the specimens in regard to the initial compliance of the beam, the crack growth initiation load, and the general force-displacement trend during crack propagation, however, VCCT underpredicts the crack growth initiation displacement. Furthermore, the maximum crack length attained from the VCCT simulations is greater than that from the experimental tests likely due to friction effects, where the crack grew to the fixed end for the VCCT simulation but did not reach the fixed end in the experimental tests. During testing, the maximum crack length was considered to be reached when the force-displacement curve reached a positive stable slope after the decrease in force due to crack propagation. This is only apparent in the force-displacement results for specimens 6 and 1, as the specimen 3 test was not carried out until maximum crack length was attained.

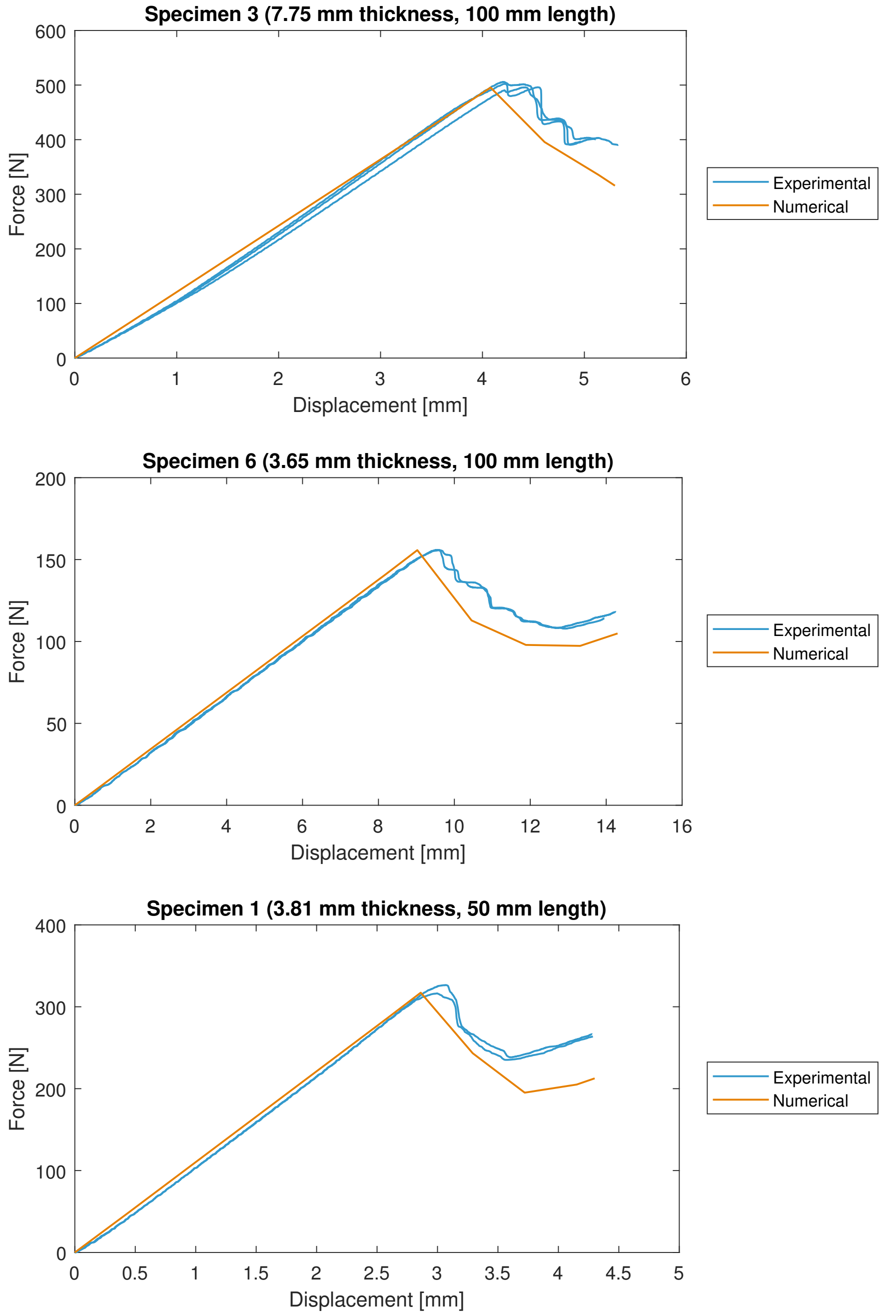

Figure 5.2: Experimental and VCCT simulation force-displacement results for the ELS Specimen PC Tests

The most immediate concern for validating these VCCT simulations is the results from mesh refinement for each of the two different thicknesses used. For shell elements, it is important to consider the thickness to characteristic length ratio, as this ratio should remain relatively small to achieve accurate results. If this ratio becomes too large, it is appropriate to use three-dimensional elements [Motley, 2018]. A mesh refinement study was done for specimen 3 (8 mm approximate thickness and 100 mm free length), and specimen 1 (4 mm approximate thickness and 50 mm free length), as shown in Figure 5.3. The mesh refinements are compared to both the analytical (closed form force-displacement solution derived in Appendix B) and the experimental force-displacement results, where the VCCT force-displacement result should converge toward the analytical solution since both are based on LEFM. This study shows that the VCCT results which matched closely with the analytical and experimental results had lower thickness to characteristic length ratios, which corresponded to a coarser mesh. Additionally, the analytical solution also underpredicts the crack initiation displacement because it does not account for friction.

For the approximately 8 mm thick specimen, even an AGS of 2 gives a high thickness to characteristic length ratio, therefore in an effort to improve the VCCT result for specimen 3, continuum shell elements were used instead of conventional shell elements. The model creation process is identical to the procedure outlined in Section 3.2, except a three-dimensional part was created for the sublaminates in the part module, the “Continuum Shell” element type was selected for the composite layup in the property module, and “SC8R,” the eight-node continuum shell element with reduced integration (Abaqus does not offer a full integration continuum shell element), was selected for the element type in the mesh module. Furthermore, the stacking direction was set to the thickness direction of the sublaminates in both the property module when creating the composite layup, and in the mesh module when assigning the continuum shell element orientation. Both the conventional and continuum shell elements use a plane stress formulation, therefore the “Lamina” constitutive definition was kept [Abaqus, 2014]. The meshes for specimen 3 with an AGS of 1 for both the conventional shell and continuum shell elements are shown in Figure 5.4, which illustrates the

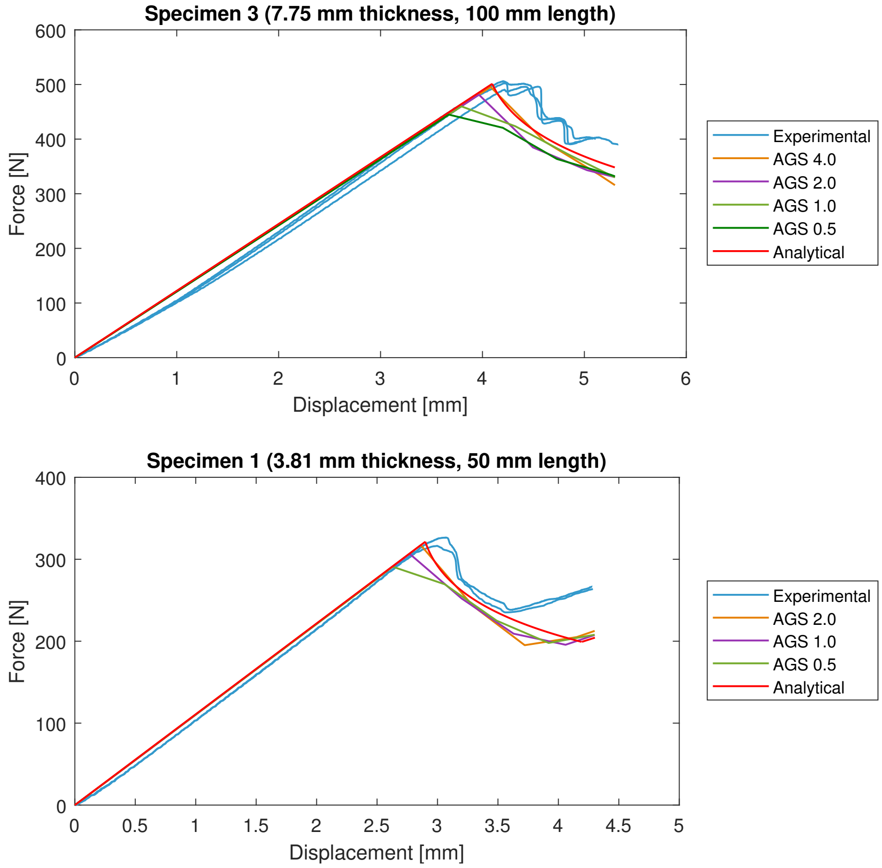

Figure 5.3: VCCT mesh refinement

inappropriate thickness to characteristic length ratio when using the conventional shell elements. The VCCT force-displacement results for the continuum shell element mesh with an AGS of 1 deviate from the experimental results, as shown in Figure 5.5. Observing the crack front advance using the “BDSTAT” variable, as mentioned in Section 3.2.4, revealed that this was caused by spurious deformations which prevented nodes that should have debonded from debonding, as shown in Figure 5.6. This is consistent with the findings of Lin [2017] when using “S4R” elements instead of “S4” elements.

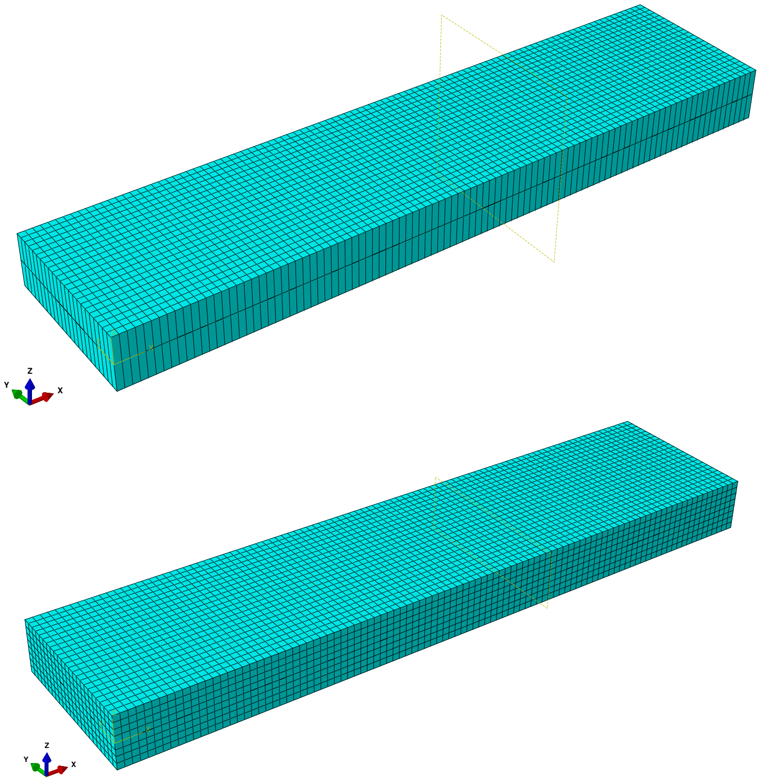

Figure 5.4: Sublaminate meshes using conventional shell elements with shell thickness rendered (top), and using continuum shell elements (bottom)

The conventional and continuum shell elements are recommended over the solid elements for modeling composites, as the composite solid elements are primarily intended for modeling conveniences and usually do not provide a more accurate solution than the composite

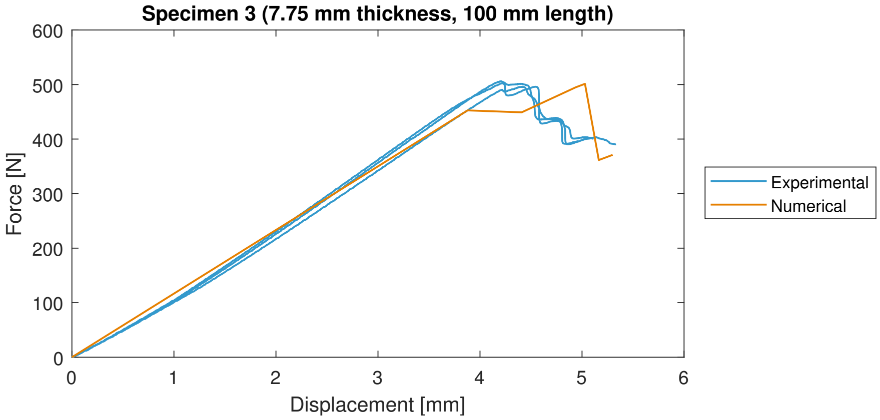

Figure 5.5: VCCT simulation force-displacement result for continuum shell element mesh

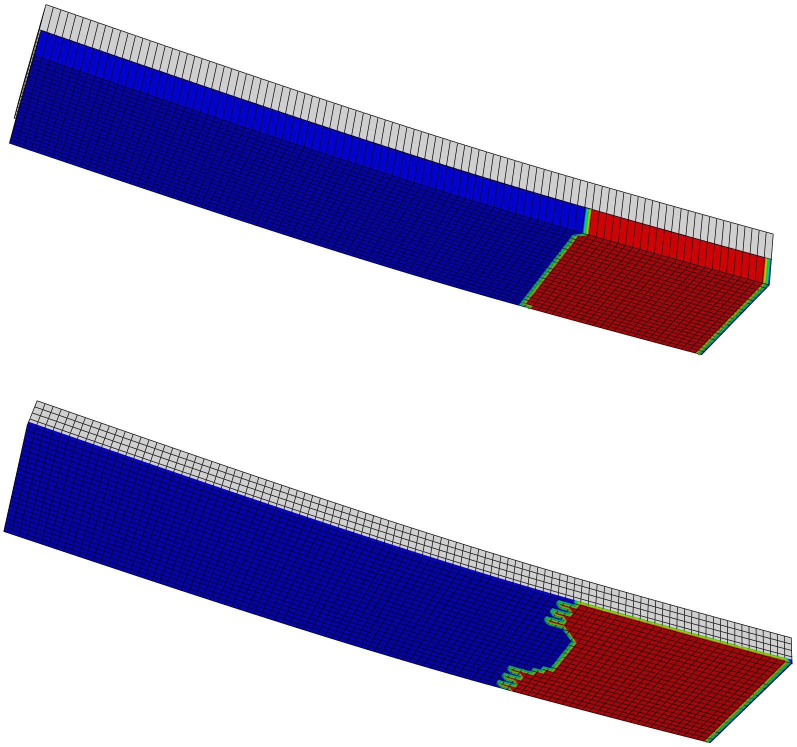

Figure 5.6: Crack front during delamination propagation for conventional shell element mesh (top), and continuum shell element mesh (bottom), where bonded and unbonded nodes are red and blue, respectively

shell elements [Abaqus, 2014]. Furthermore, the solid element does not use a plane stress formulation, and therefore the constitutive definition must be modified to include more mechanical material parameters than were determined for this thesis. For these reasons, the solid elements were not used to model the sublaminates for VCCT.

Despite the limiting assumptions used for VCCT (LEFM), and the limitations on mesh size due to beam geometry, the VCCT simulation results compare well with the experimental results when using the material properties associated with each specimen. These results show that the virtual crack closure technique is appropriate for modeling mode II delamination in unidirectional composite beams. Furthermore, these results highlight the need for an “SC8” element, as the “SC8R” element is likely appropriate for modeling general composite mechanical behavior, but when used in conjunction with VCCT the “SC8R” element introduces errors.

### *5.2.2 CZM*

The CZM models were created for each of the three selected specimens using the procedure outlined in Section 3.4, the beam geometries provided in Section 2.2, the mechanical properties provided in Section 4.1, and the fracture properties provided in Section 4.2. The force-displacement results from the CZM simulations are compared to the experimental test data for each of the three specimens in Figure 5.7. For specimen 3 the AGS of the shell elements was 2 and the AGS of the cohesive elements was 0.5, and for specimens 6 and 1 the AGS of the shell elements was 1 and the AGS of the cohesive elements was 0.5 (the cohesive elements were approximately square with approximately 0.5 mm dimensions, and had zero thickness). The CZM simulation results compare well with the experimental data for all three of the specimens in regard to the initial compliance, the crack growth initiation displacement, and the general force-displacement trend during crack propagation, however, the CZM underpredicts the crack growth initiation load. The VCCT better predicts the crack growth initiation load while the CZM better predicts the crack growth initiation displacement. Similar to VCCT, the final crack length of the CZM simulation is longer than the experimental data because the Abaqus model does not account for friction (although this could be introduced in the traction-separation law). This is only apparent for specimens 6 and 1, as the specimen 3 test was not carried out until maximum crack length was attained. Unlike VCCT, where the force-displacement curve is smooth during crack propagation, the CZM curve is jagged. This jaggedness is dependent on the mesh sizes of the shell elements and the cohesive elements, where a sudden loss in stiffness on the force-displacement curve occurs when cohesive elements fail at the crack front and the load is then carried by the adjacent cohesive elements.

A similar mesh refinement study to VCCT was carried out for the CZM, where various mesh sizes for specimens 3 and 1 are compared to the experimental test data as well as the analytical force-displacement solution, as shown in Figure 5.8. Although the mesh refinement for VCCT showed that there were issues with small mesh sizes using the conventional shell elements, the mesh refinement for the CZM converges toward the analytical solution since the bond between the sublaminates is represented by the cohesive elements for the CZM, rather than through the nodes of the shell elements for VCCT. Furthermore, the mesh refinement for the CZM shows that, as mentioned previously, the performance of the CZM depends on both the shell and cohesive element sizes, where the jagged behavior during crack propagation becomes less pronounced with mesh refinement. Unlike VCCT where the initial compliance matches the experimental and analytical results, the CZM exhibits an over-softening prior to the crack growth initiation point, which also becomes less pronounced with mesh refinement.

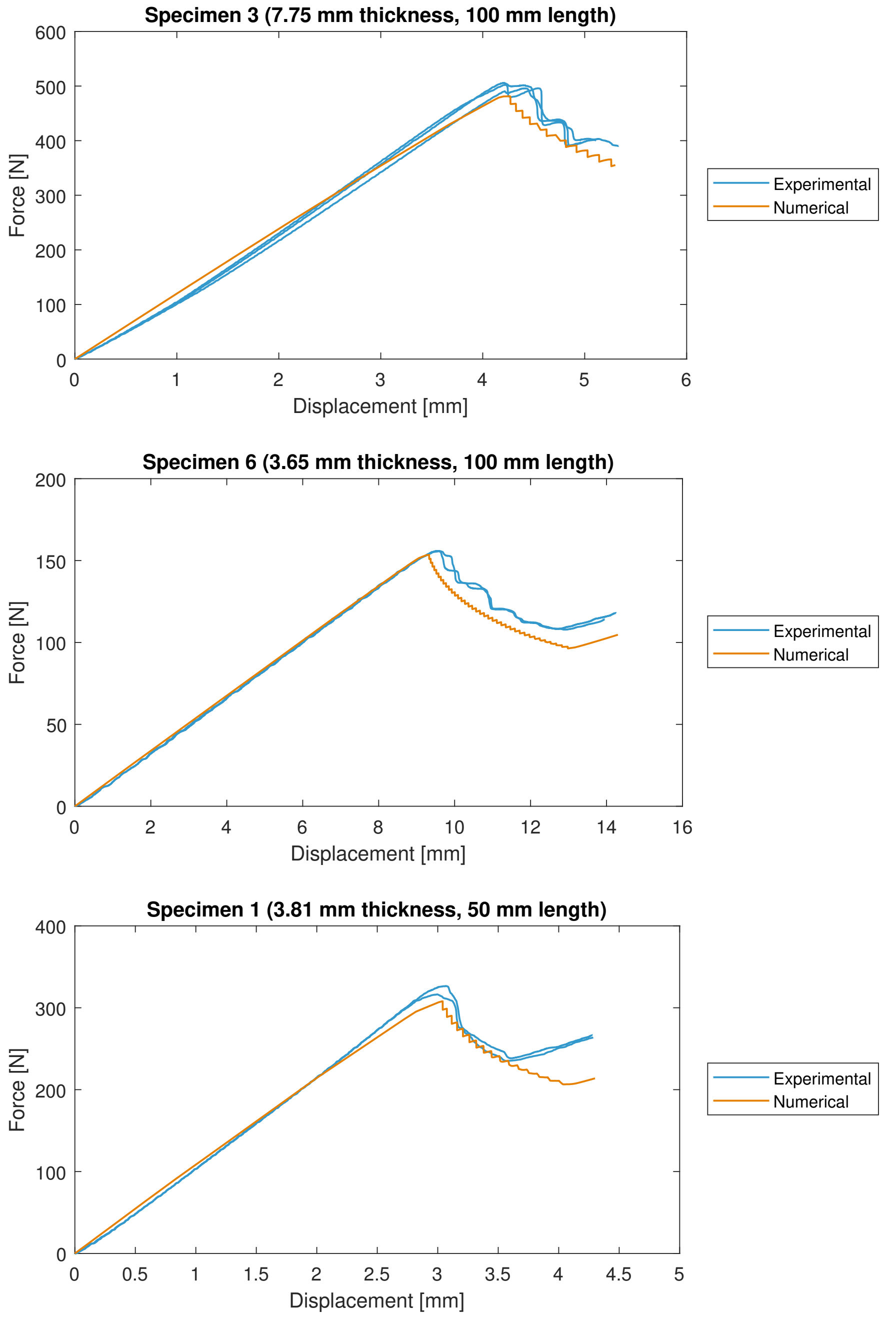

Figure 5.7: Experimental and CZM simulation force-displacement results for the ELS Specimen PC Tests

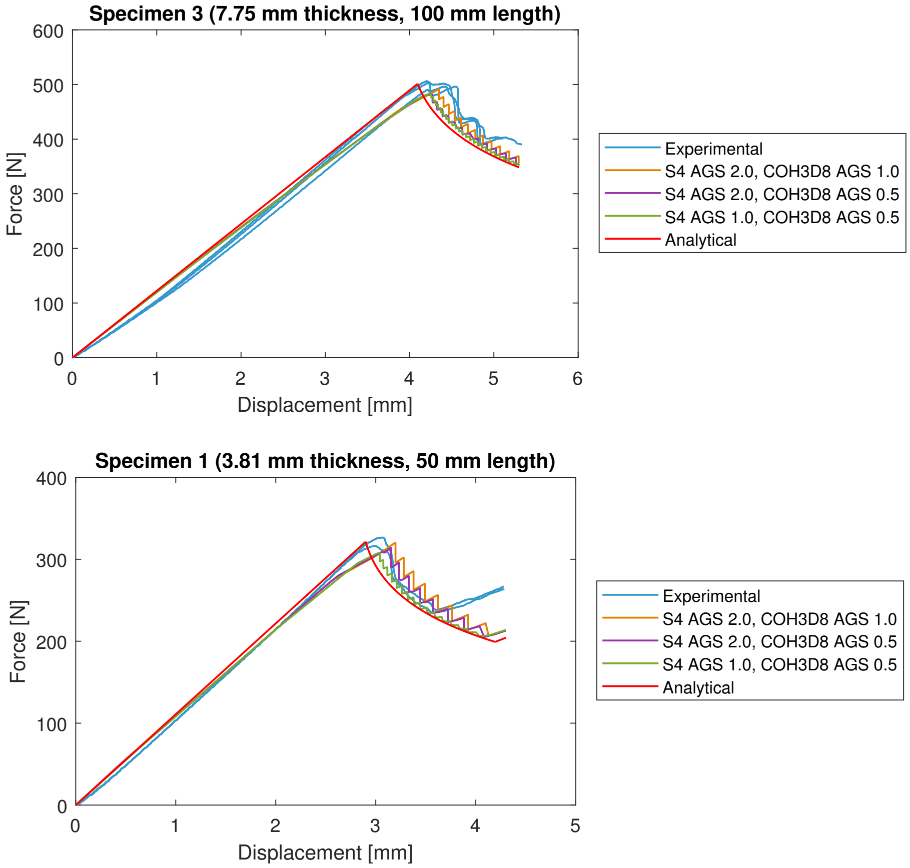

Figure 5.8: CZM mesh refinement

### *5.2.3 Size Effects on Model Accuracy*

To investigate size effects, specimens 3 and 1 were modeled using the properties from specimen 6 because this specimen has the lowest (most conservative) value for $G_{IIC}$. Specimens 3 and 1 were modeled using both the VCCT and CZM methods. For each specimen for each crack growth model two simulations were run: (1) using only $G_{IIC}$ from specimen 6, and (2) using both $E_1$ and $G_{IIC}$ from specimen 6. These results are shown for specimen 3 in Figure 5.9, and for specimen 1 in Figure 5.10. The VCCT simulations in these figures used a mesh with an AGS of 2, the specimen 3 CZM simulation used a shell element mesh with an AGS of 2 and a cohesive element mesh with an AGS of 0.5, and the specimen 1 CZM simulation used a shell element mesh with an AGS of 1 and a cohesive element mesh with an AGS of 0.5.

Interchanging only the value of $G_{IIC}$ between specimen numerical models should yield similar beam behavior if $G_{IIC}$ is truly a material property independent of size effects. However, the numerical modeling done for this thesis shows that to accurately model the crack growth using the two modeling methods, $E_1$ and $G_{IIC}$ are not independent. Size effects are evident in all of the simulation results shown in Figures 5.9 and 5.10, as the use of the specimen 6 properties underpredicts both crack growth initiation displacement and load even when using $E_1$ and $G_{IIC}$ together. This investigation reveals how important and difficult it is to obtain not only accurate fracture properties, but mechanical properties as well. The disparity between the $E_1$ values when using varying thickness to free length ratios implies not only issues due to size effects, but the possibility of issues associated with the repeatability of the clamped end, and whether perfect fixity is appropriate for modeling the clamped end boundary condition in Abaqus. Furthermore, this investigation reveals that even the more sophisticated material model used for the CZM method cannot handle size effects well.

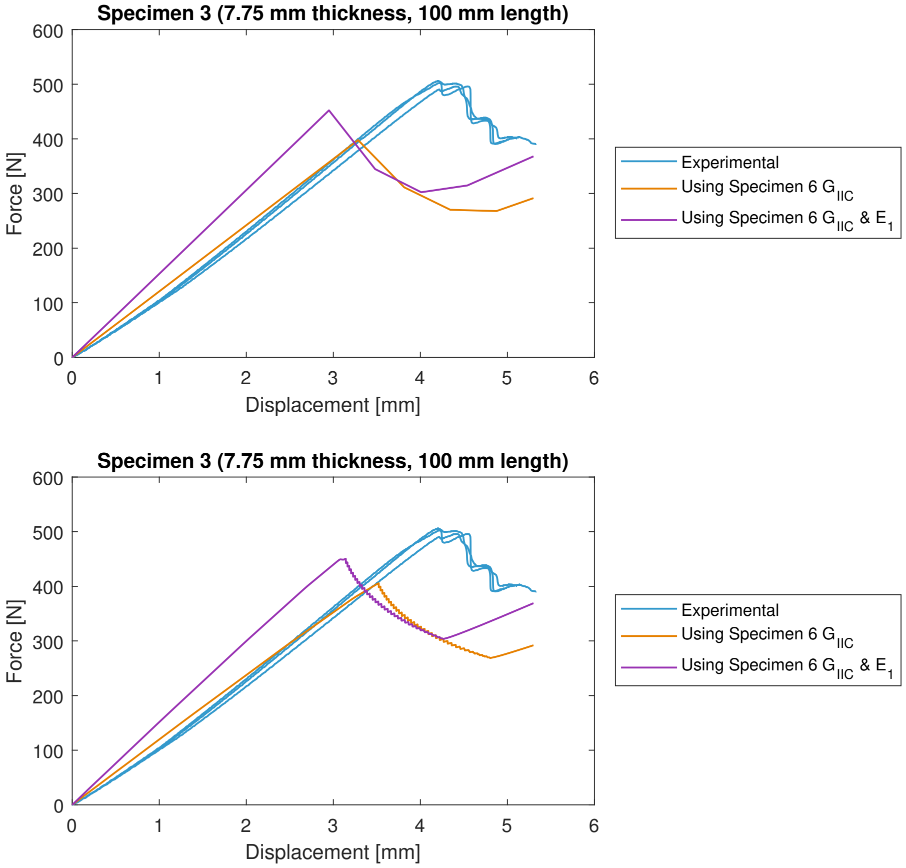

Figure 5.9: Force-displacement results for the investigation of size effects for specimen 3 using VCCT (top), and CZM (bottom)

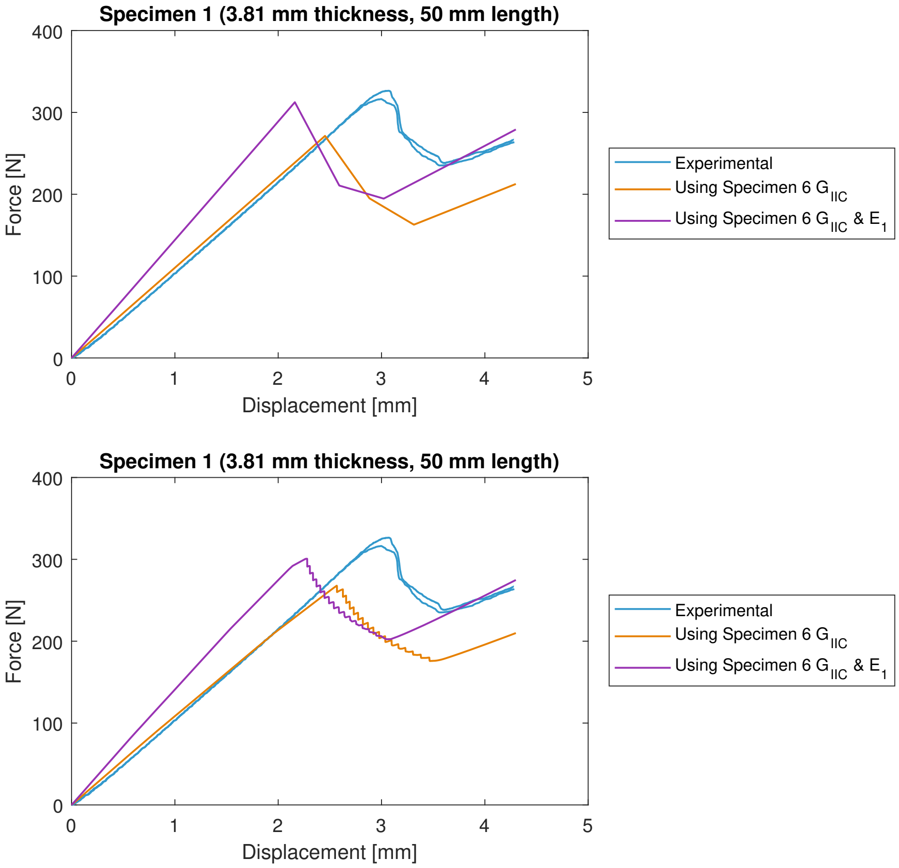

Figure 5.10: Force-displacement results for the investigation of size effects for specimen 1 using VCCT (top), and CZM (bottom)

# Chapter 6

# THROUGH-THICKNESS DISPLACEMENT FIELD RESULTS

This chapter discusses the analysis of the through-thickness displacement field data obtained from the DIC system, and discusses the applicability of the analysis results for determining pristine and cracked beam behavior. The traction-separation law used for the Abaqus simulations was based on several limiting assumptions, namely the values for penalty stiffnesses and interface strengths, along with bilinear behavior. Ideally, an exact traction-separation law would be obtained by observing the deformation field near the crack tip, rather than depending on assumed material properties and behavior. With this goal in mind, the DIC results from both the pristine and fracture tests were investigated for an 8 mm thick specimen, as there is more through-thickness speckled surface area to be analyzed compared to a 4 mm thick specimen, and hence the results for this specimen should be better.

This analysis focuses on the suitability of the DIC system for determining through-thickness beam behavior by comparing the experimental results to the predicted theoretical behavior for thin beams. The strains were calculated from the displacement field data, and the stresses were calculated using the constitutive law, then the shear stress distribution was compared to the known load applied to the beam through the theoretical through-thickness shear stress distribution. Finally, the shear stresses were integrated through the thickness to obtain the shear force diagram, which was also compared to the known load applied to the beam. It is important to note that the DIC results are highly dependent on the quality of the beam speckle, as well as the technician's skills for calibrating the DIC system.

### 6.1 Displacement Field Data

The DIC system uses the beam speckle to discretize a through-thickness face of the beam, as shown in Figure 6.1 for the specimen 3 (approximately 8 mm thickness and 100 mm length) pristine beam test for undeformed and deformed beam configurations. The fixed end of the cantilever beam is on the right, and the free end is on the left. The DIC software provides these displacement fields in the form of original nodal coordinates from a reference image of the beam in an undeformed state, and nodal displacements calculated from images taken during testing of the beam undergoing deformation relative to the reference image.

Filtering was done on the displacement field data to remove data points which either had very large nodal coordinates or displacements (did not lay on the face of the beam) or had values of zero. The DIC software also provides a variable "sigma" which is the confidence interval for the match at every point, in pixels [Correlated Solutions, 2016]. The typical range for "sigma" for this thesis was 0.01-0.05, and a value of $-1$ for "sigma" implied no confidence, hence the data points which had a $-1$ value for "sigma" were also removed. With this data filtering, the load application point is visible in the pristine beam displacement field in the form of missing nodes, where during testing the load application roller or its shadow obscured the camera's view of the speckle at the point of contact with the beam, as shown in Figure 6.1. The data filtering for the fracture test resulted in the displacement field shown in Figure 6.2 for undeformed and deformed states, where the beam speckle was compromised by the splitting of the beam at the mid-plane. There are approximately 20 through-thickness data points discretizing this approximately 8 mm thick beam for the pristine beam test, and even less for the fracture test due to the missing data points compromised by the crack.

These displacement fields capture portions of the beam which extend past the boundary conditions (to the left of the load application point at the free end, and to the right of the fixed end). Furthermore, the load application roller changes point of contact with the beam as it deforms, and the fixed end rotates slightly in the clamping fixture.

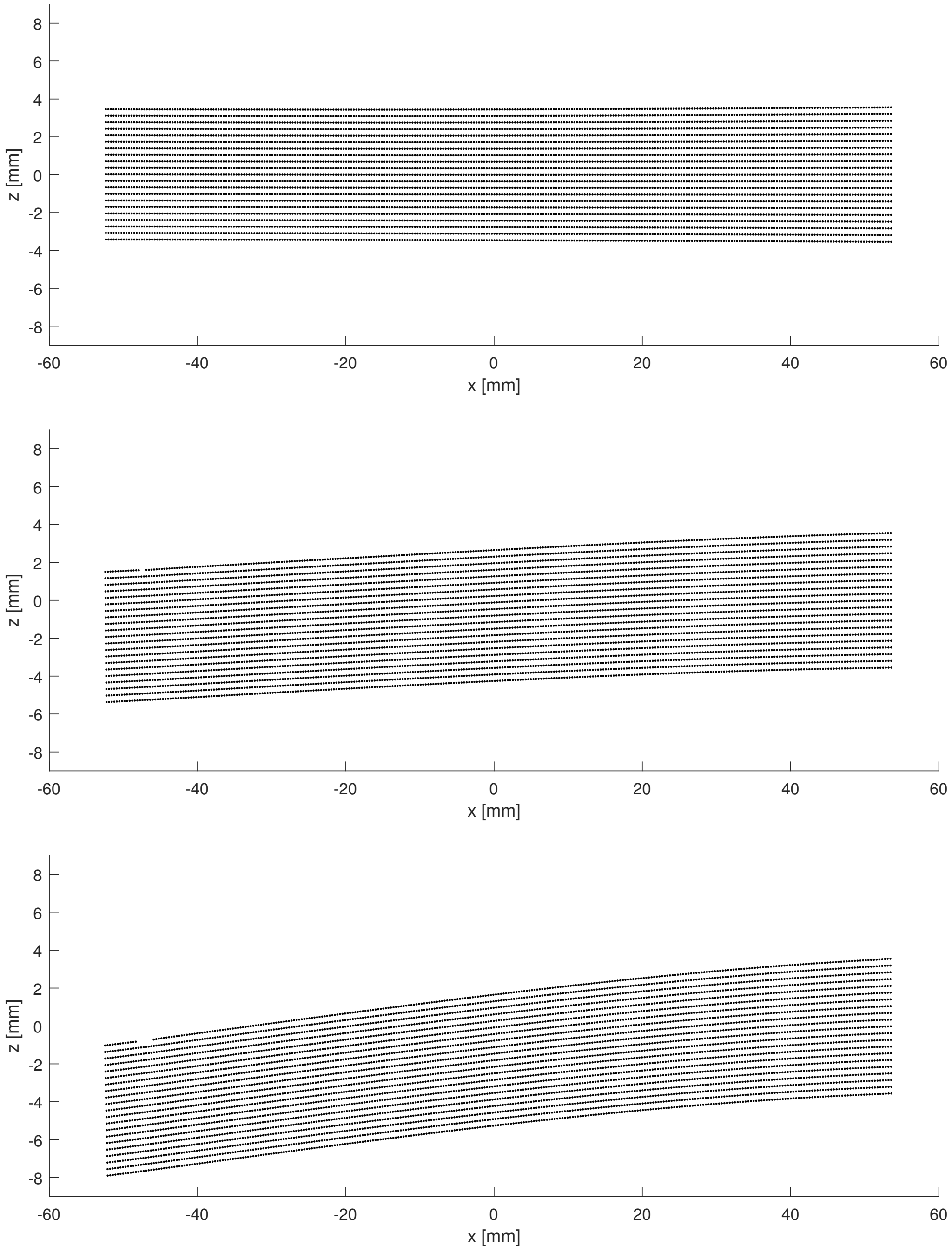

Figure 6.1: Through-thickness displacement field for approximately 8 mm thick specimen pristine beam test

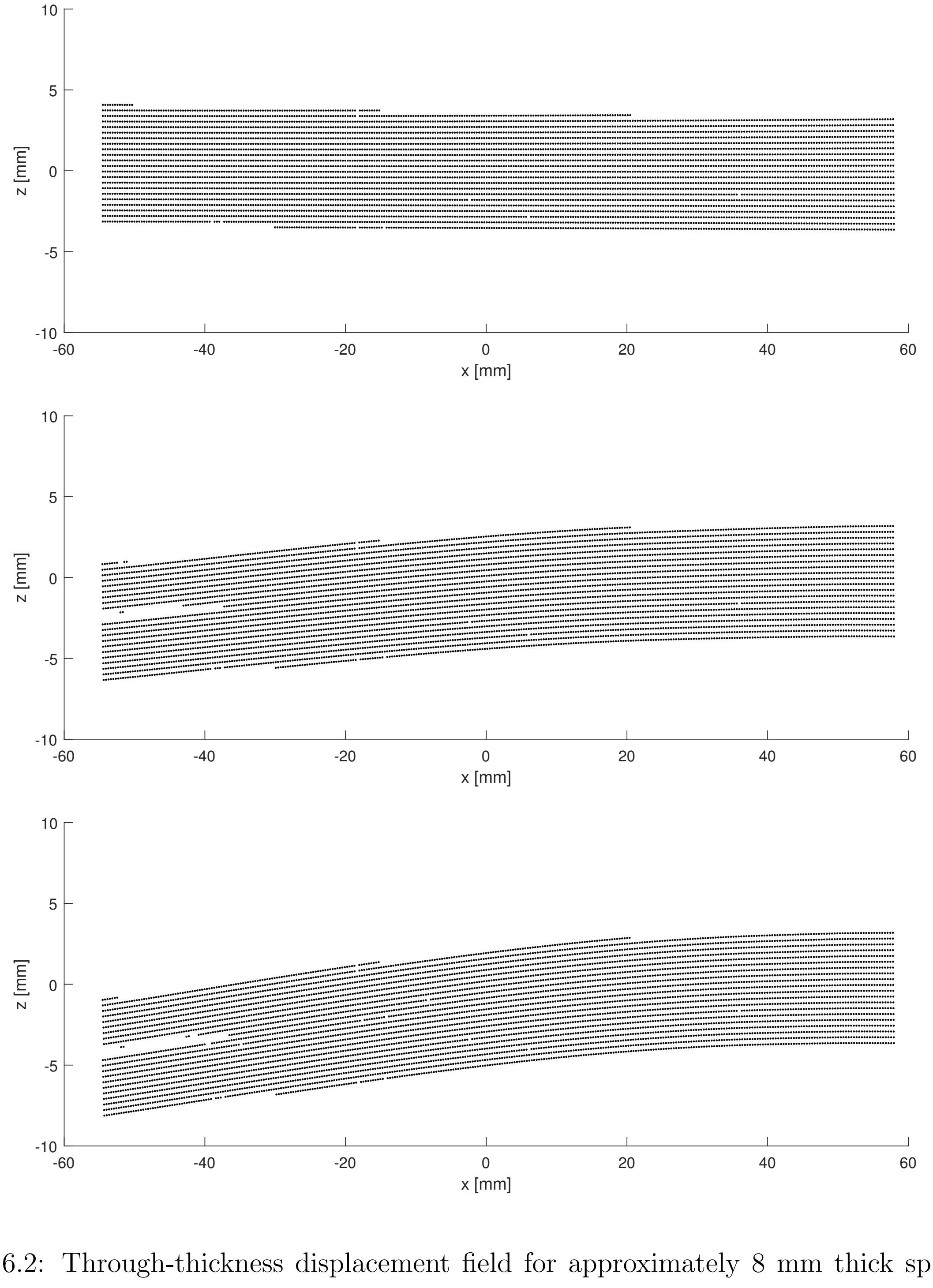

Figure 6.2: Through-thickness displacement field for approximately 8 mm thick specimen fracture test

## 6.2 Analysis Methodology

The DIC software is capable of performing strain calculations in a similar way to FEM software [Correlated Solutions, 2016]. The displacement field is used to create a mesh of triangular elements for which the strain tensor is calculated for each element, then nodal strain values are determined by interpolating the strains from the elements surrounding each node. Finally, these nodal strain values are smoothed over a group of points using a Gaussian filter, as the nodal strain tensors can be noisy since the triangular elements are small [Correlated Solutions, 2016]. This is illustrated schematically in Figure 6.3.

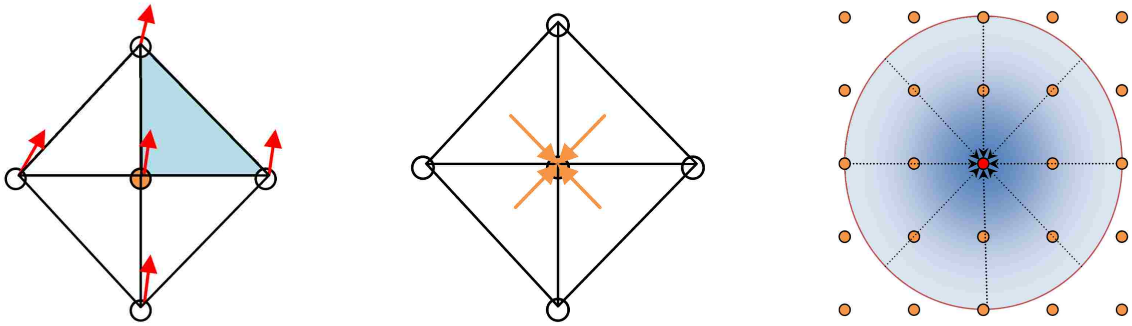

Figure 6.3: Triangular mesh (left), nodal strain value interpolation (middle), and smoothing scheme for nodal strains (right) [Correlated Solutions, 2016]

Separate strain calculations were done for this thesis to serve as a comparison to the DIC software generated strain values. Two methods were used: (1) the finite difference method, where the central difference method was used as much as possible, but the forward and backward difference methods were used for nodes at the borders and for nodes adjacent to missing nodes, and (2) a "smoothed" finite difference method where polynomial curves were fit to the displacement fields and derivatives were taken with respect to these polynomials to solve strain. To solve the strains, and subsequently the stresses and shear forces, consider the composite beam shown in Figure 6.4, where the local coordinate system is defined by the 1-, 2-, and 3-axes, and the global coordinate system is defined by the $x$-, $y$-, and $z$-axes.

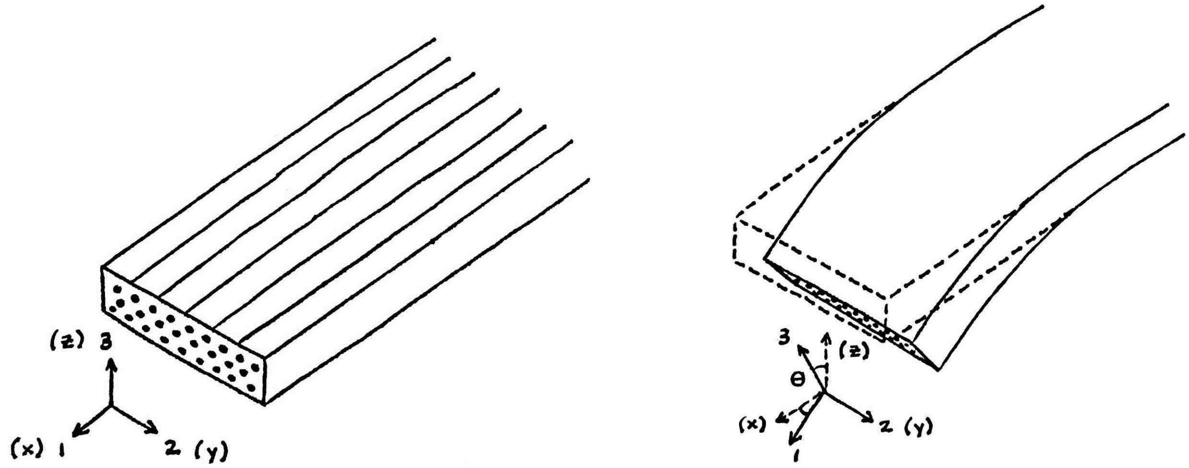

Figure 6.4: Transversely isotropic beam in an undeformed state (left), and undergoing deformation such that the local 2- and global $y$-axes are coincident and the 13-plane is rotated about these axes by the beam angle $\theta$ (right)

This beam is transversely isotropic with the 1-axis aligned with the fiber direction, and with isotropy in the 23-plane. Considering the ELS testing done for this thesis, it is reasonable to assume that the 2-axis and the $y$-axis are always coincident, and the rotation of the 13-plane about these axes is the rotation of the beam. The strains for both methods previously mentioned were calculated as

$$\varepsilon_x = \frac{\partial u}{\partial X}, \qquad \varepsilon_z = \frac{\partial w}{\partial Z}, \qquad \varepsilon_{xz} = \frac{1}{2}\left(\frac{\partial u}{\partial Z} + \frac{\partial w}{\partial X}\right)$$

where $X$ and $Z$ denote the original nodal positions, $u$ and $w$ are the nodal displacements in the $x$- and $z$-directions, respectively, and $\gamma_{xz} = 2\,\varepsilon_{xz}$.

To obtain stress values from the calculated strain values, the constitutive law was defined assuming assuming linear elasticity. Although linear elasticity in the vicinity of the crack tip is not accurate, the results obtained using this assumption are investigated to serve as a baseline for understanding the DIC capabilities. The local stresses and strains are related through the compliance matrix for a transversely isotropic material defined by

$$\begin{Bmatrix} \varepsilon_1 \\ \varepsilon_2 \\ \varepsilon_3 \\ \gamma_{23} \\ \gamma_{13} \\ \gamma_{12} \end{Bmatrix} = \begin{bmatrix} \frac{1}{E_1} & \frac{-\nu_{12}}{E_1} & \frac{-\nu_{12}}{E_1} & 0 & 0 & 0 \\ \frac{-\nu_{12}}{E_1} & \frac{1}{E_2} & \frac{-\nu_{23}}{E_2} & 0 & 0 & 0 \\ \frac{-\nu_{12}}{E_1} & \frac{-\nu_{23}}{E_2} & \frac{1}{E_2} & 0 & 0 & 0 \\ 0 & 0 & 0 & \frac{2(1+\nu_{23})}{E_2} & 0 & 0 \\ 0 & 0 & 0 & 0 & \frac{1}{G_{12}} & 0 \\ 0 & 0 & 0 & 0 & 0 & \frac{1}{G_{12}} \end{bmatrix} \begin{Bmatrix} \sigma_1 \\ \sigma_2 \\ \sigma_3 \\ \tau_{23} \\ \tau_{13} \\ \tau_{12} \end{Bmatrix}.$$

The strains and stresses in the 13-plane may be calculated using the through-thickness displacement field data provided by the DIC system. It is reasonable to assume that for a transversely isotropic beam in bending $\varepsilon_2$, $\gamma_{23}$, and $\gamma_{12}$ are zero, and hence the stress-strain relationship simplifies to

$$\begin{Bmatrix} \sigma_1 \\ \sigma_3 \\ \tau_{13} \end{Bmatrix} = \begin{bmatrix} Q_{11} & Q_{13} & 0 \\ Q_{13} & Q_{33} & 0 \\ 0 & 0 & Q_{55} \end{bmatrix} \begin{Bmatrix} \varepsilon_1 \\ \varepsilon_3 \\ \gamma_{13} \end{Bmatrix}$$

where $Q_{11}$, $Q_{13}$, $Q_{33}$, and $Q_{55}$ are solved by inverting the full compliance matrix. Using the material properties as determined in Section 4.1, and assuming $\nu_{23}$ is equal to $\nu_{12}$ gives

$$\begin{aligned} Q_{11} &= \frac{1}{D}\, E_1^2(\nu_{12}-1), & Q_{13} &= -\frac{1}{D}\, E_1 E_2 \nu_{12}, \\ Q_{33} &= \frac{1}{D}\, \frac{E_2(E_2\nu_{12}^2 - E_1)}{\nu_{12}+1}, & Q_{55} &= G_{12} \end{aligned}$$

where $D = 2E_2\nu_{12}^2 - E_1 + E_1\nu_{12}$.

This stress-strain relationship is valid in the local coordinate system of the beam, but the displacement field data is given in terms of global coordinates. Therefore, two methods were used to calculate stresses: (1) using a small displacement formulation such that the local coordinate system was assumed to be identical to the global coordinate system, and (2) using a large displacement formulation. The stress-strain relationship for the small displacement formulation is given by

$$\begin{Bmatrix} \sigma_x \\ \sigma_z \\ \tau_{xz} \end{Bmatrix} = \begin{bmatrix} Q_{11} & Q_{13} & 0 \\ Q_{13} & Q_{33} & 0 \\ 0 & 0 & Q_{55} \end{bmatrix} \begin{Bmatrix} \varepsilon_x \\ \varepsilon_z \\ \gamma_{xz} \end{Bmatrix},$$

and for the large displacement formulation is given by

$$\begin{Bmatrix} \sigma_x \\ \sigma_z \\ \tau_{xz} \end{Bmatrix} = \begin{bmatrix} c^2 & s^2 & 2cs \\ s^2 & c^2 & -2cs \\ -cs & cs & c^2 - s^2 \end{bmatrix}^{-1} \begin{bmatrix} Q_{11} & Q_{13} & 0 \\ Q_{13} & Q_{33} & 0 \\ 0 & 0 & Q_{55} \end{bmatrix} \begin{bmatrix} c^2 & s^2 & cs \\ s^2 & c^2 & -cs \\ -2cs & 2cs & c^2 - s^2 \end{bmatrix} \begin{Bmatrix} \varepsilon_x \\ \varepsilon_z \\ \gamma_{xz} \end{Bmatrix}$$

where $c$ and $s$ are $\cos\theta$ and $\sin\theta$, respectively, and $\theta$ is the beam rotation. The through-thickness shear stress distributions were compared to the theoretical parabolic shear stress distribution, where the theoretical solution was determined using the known load applied to the beam for the given beam displacement, and the known beam thickness as provided in Table 2.3.

The experimental shear force diagram was obtained by integrating the shear stress distributions through the beam thickness using the trapezoidal rule. The experimental shear force diagram was then compared to the theoretical shear force diagram which was obtained using the known load applied to the beam for the given beam displacement.

### *6.3 Pristine Beam Strain Field*

The $\varepsilon_x$, $\varepsilon_z$, and $\gamma_{xz}$ strain fields are provided and discussed in this section for the approximately 8 mm thick specimen 3 pristine beam test. For the "smoothed" finite difference method, polynomials of order 3 were used for the displacement field fits, and the results from these analyses are discussed later in comparison to higher order polynomials. The normal strain in the $x$-direction is shown in Figure 6.5. The expected theoretical linear shape is obtained only from the DIC software calculations. The finite difference method is too noisy to observe any distinct trends in the data, and the “smoothed” finite difference method exhibits a linear shape, but is skewed such that the neutral axis does not appear to be at the mid-plane of the beam. The normal strain in the $z$-direction is shown in Figure 6.6, and all three methods for calculating strain give the expected theoretical result of near 0 pinching strain. The shear strain in the $xz$-plane is shown in Figure 6.7. The expected theoretical parabolic shape for shear strain is obtained only from the DIC software calculations, and the “smoothed” finite difference method. The finite difference method gives a noisy shear strain distribution. The portions of the beam which extend past the boundary conditions are evident in all of the three-dimensional strain distribution plots.

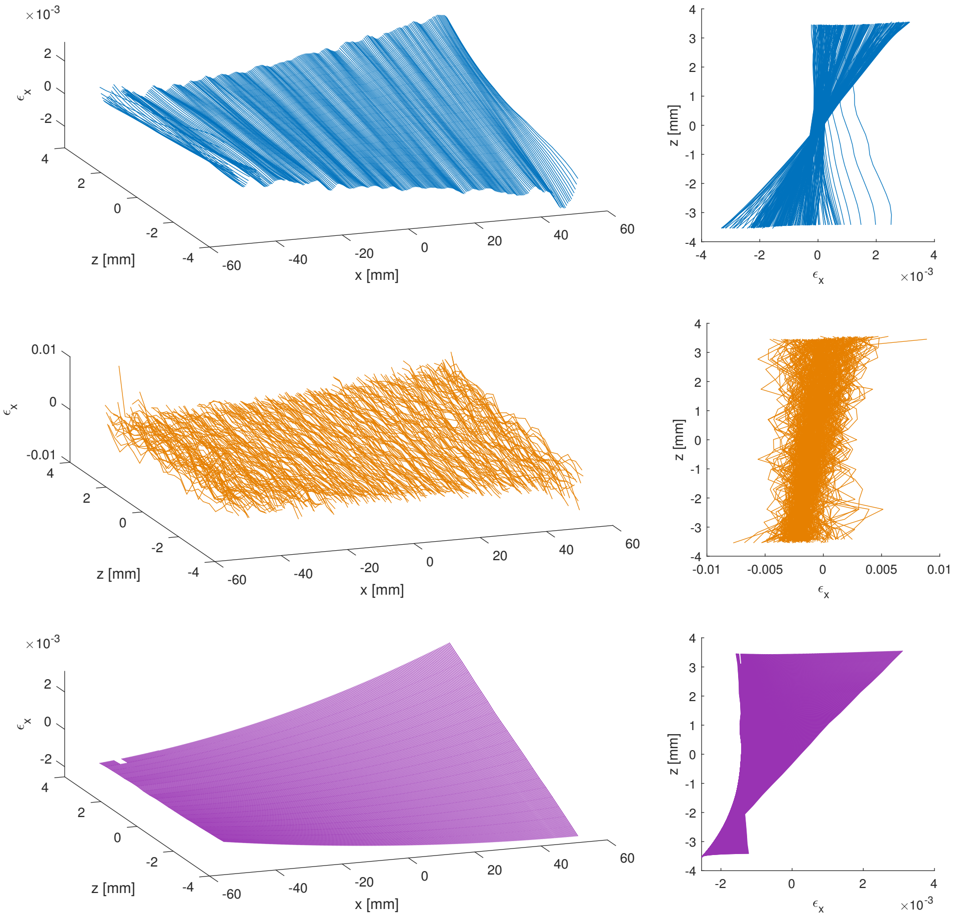

Figure 6.5: Pristine beam through-thickness $\varepsilon_x$ field using DIC software calculations (top), finite difference method (middle), and "smoothed" finite difference method (bottom)

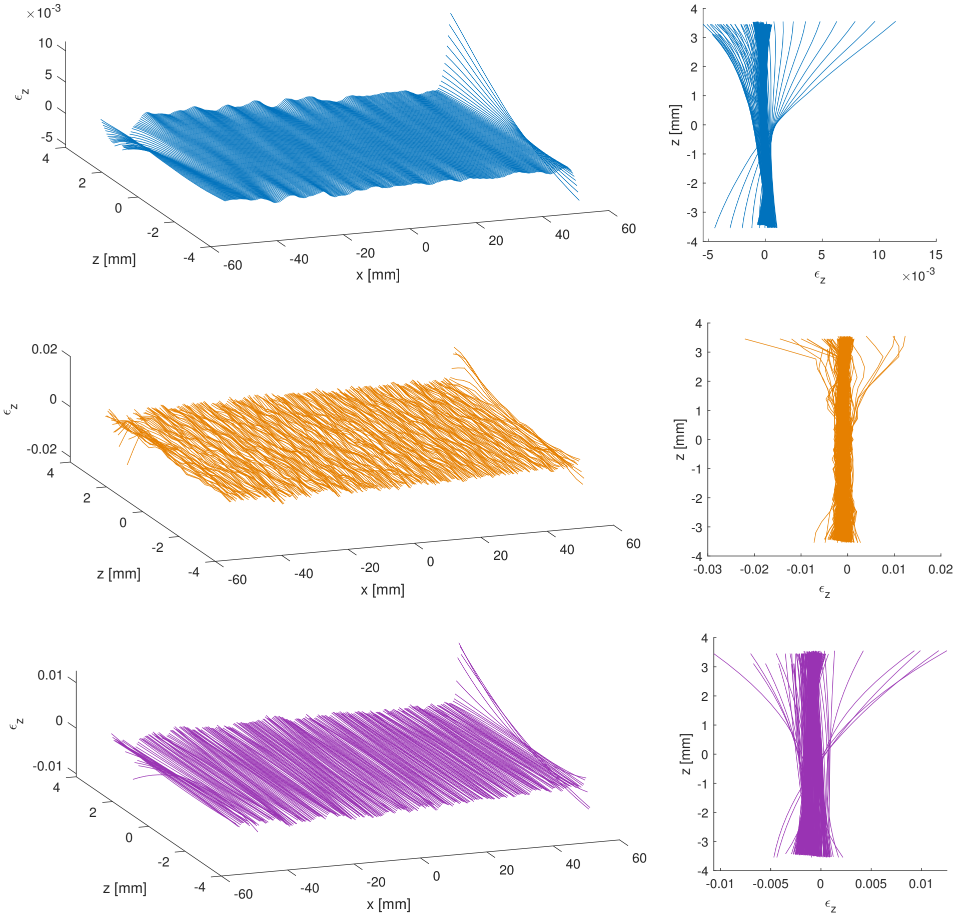

Figure 6.6: Pristine beam through-thickness $\varepsilon_z$ field using DIC software calculations (top), finite difference method (middle), and "smoothed" finite difference method (bottom)

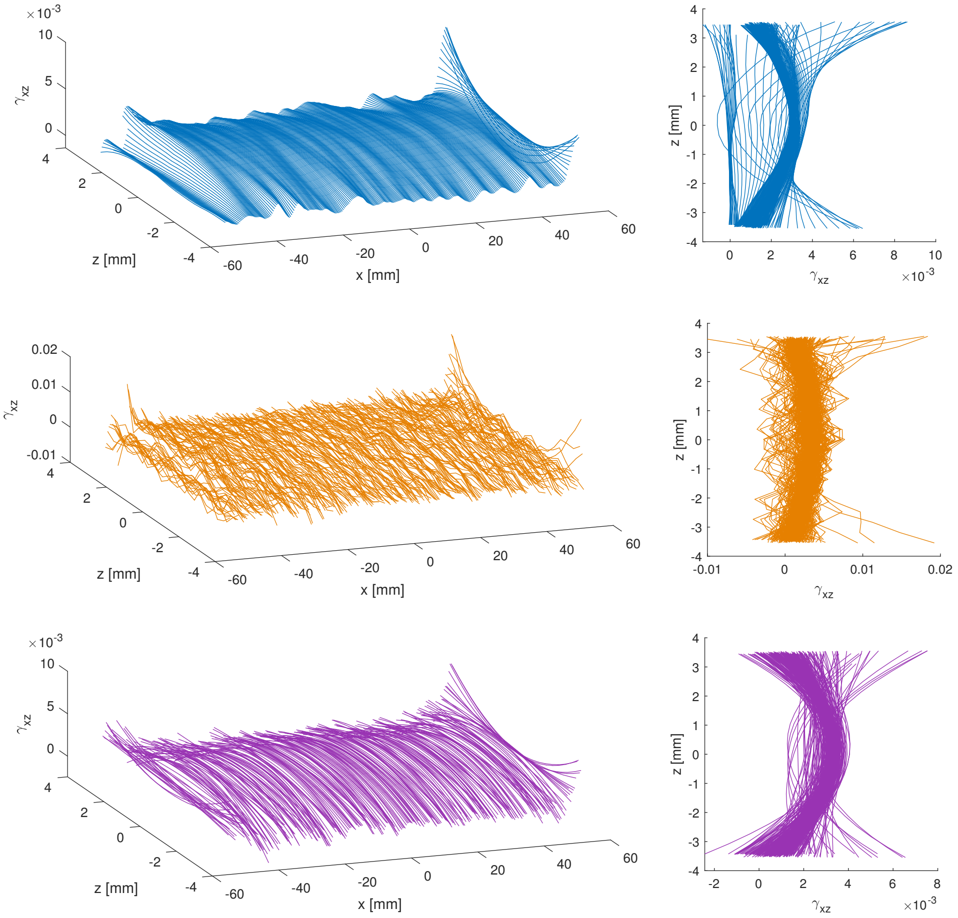

Figure 6.7: Pristine beam through-thickness $\gamma_{xz}$ field using DIC software calculations (top), finite difference method (middle), and “smoothed” finite difference method (bottom)

## 6.4 Pristine Beam Shear Stress Field

For the approximately 8 mm thick and 100 mm long specimen 3, the slope of the beam used to transform the local stiffness matrix is shown in Figure 6.8 for a loaded configuration. These slopes were obtained by fitting polynomials of order 3 to the displacement in the $z$-direction $w$, and the current nodal position $x$ for each row of nodes, then using

$$\theta = \frac{\partial w}{\partial x}.$$

The general trend for the experimental beam slope matches the theoretical solution, but the magnitudes do not match. This plot of the slope also reveals the difficulty in achieving perfect fixity for the clamped end, as there is a small rotation at the right end.

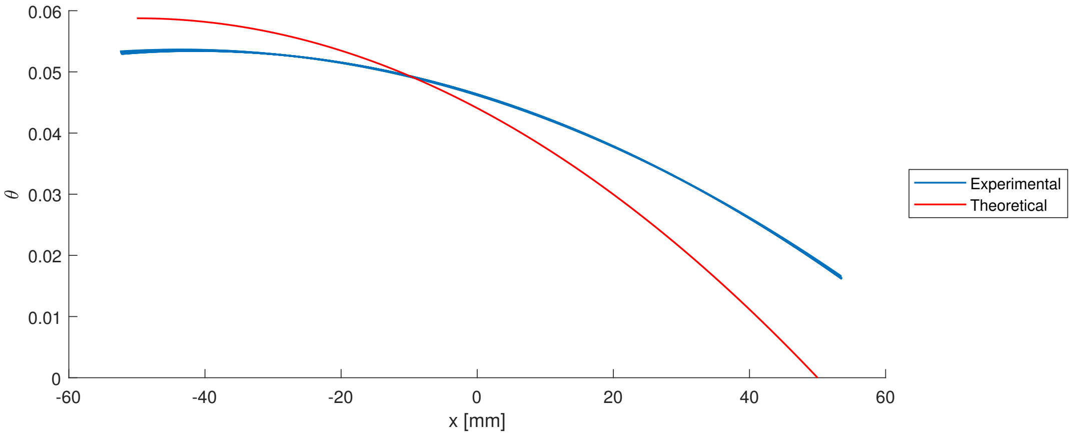

Figure 6.8: Pristine beam experimental and theoretical slope for a loaded configuration

For the specimen 3 pristine beam test, the shear stress distribution assuming small displacements is shown in Figure 6.9. The shape of these curves is identical to the shear strain distribution shapes shown previously with only a change in magnitude due to the constitutive law. The shear stress distribution using the transformed constitutive law (large displacement formulation) is shown in Figure 6.10. Since the $\varepsilon_z$ through-thickness distributions were nearly zero, the variations between the small displacement and large displacement formulations were dominated by $\varepsilon_x$. The $\tau_{xz}$ distributions using the large displacement formulation do not yield a better result than the small displacement formulation, as they are skewed slightly such that the distribution is no longer approximately symmetric about the beam mid-plane.

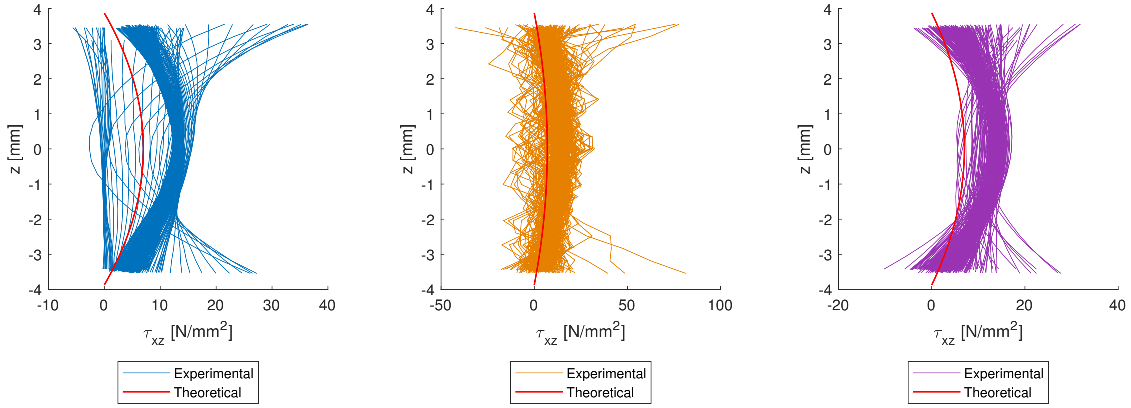

Figure 6.9: Pristine beam through-thickness $\tau_{xz}$ field using small displacement formulation for DIC software calculations (left), finite difference method (middle), and "smoothed" finite difference method (right)

These shear stress distributions illustrate the coarseness of the DIC system discretization of the through-thickness surface of the beam, as the experimental shear stress distributions do not span the full thickness of the beam, while the theoretical shear stress distribution uses the actual beam thickness. All methods for obtaining $\tau_{xz}$ through the beam thickness yielded a stress distribution which was on average greater in magnitude than the theoretical solution.

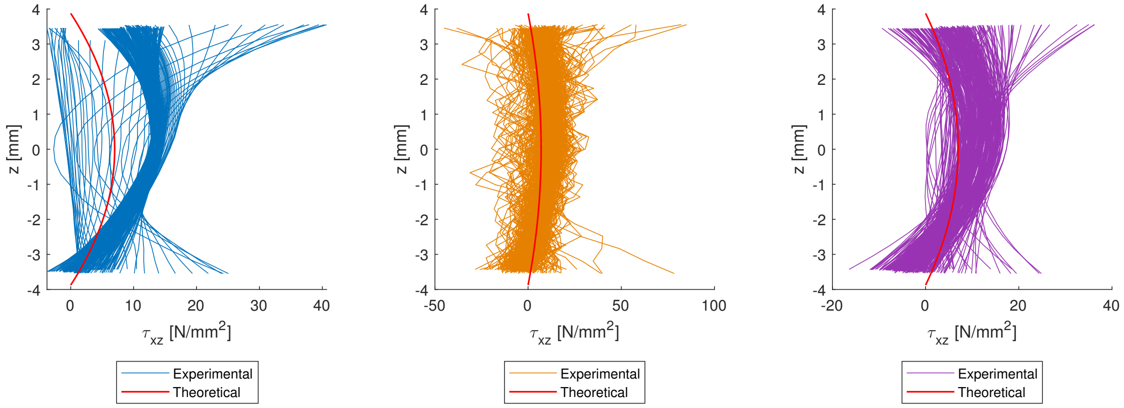

Figure 6.10: Pristine beam through-thickness $\tau_{xz}$ field using large displacement formulation for DIC software calculations (left), finite difference method (middle), and "smoothed" finite difference method (right)

## *6.5 Pristine Beam Shear Force Diagram*

The shear force diagram derived from all three strain calculation methods using the small displacement formulation is shown in Figure 6.11. The diagrams are approximately constant, but the experimental calculations significantly overestimate the shear force. The three strain calculation methods show good agreement, hence validating both the DIC software calculations, as well as the alternate strain calculation formulations used for this thesis. The finite difference method shear diagram is more noisy than the DIC software calculated shear diagram, and as expected, the "smoothed" finite difference method produces a slightly less noisy shear diagram than the finite difference method. The "smoothed" finite difference method does not capture the portions of the beam which extend past the boundary condition when using polynomial fits of order 3, as is visible on both the left and right ends of the shear diagram.

The shear diagrams using the large displacement formulation are compared to the small displacement formulation in Figure 6.12. The DIC calculated shear force diagram shows little change between the small and large displacement formulations, but both the finite

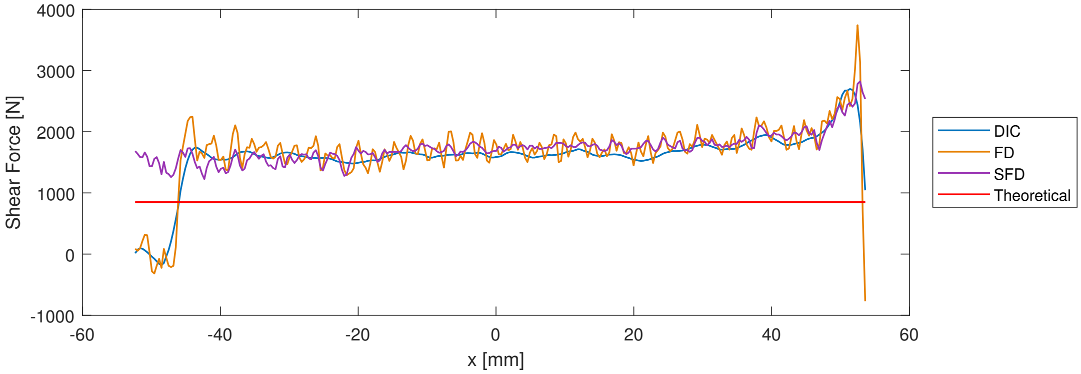

Figure 6.11: Pristine beam shear force diagram using small displacement formulation

difference and the "smoothed" finite difference derived shear force diagrams show a vast disparity between the small and large displacement formulations. This disparity is likely primarily due to the $\varepsilon_x$ contribution where recalling from Section 6.3 that the $\varepsilon_x$ distribution only exhibited the expected theoretical behavior for the DIC software calculation, and the $\varepsilon_z$ distributions were nearly 0 for all strain calculation methods. These shear force diagram comparisons show that even for a small slope, and hence a small change in the stiffness matrix, vastly different shear force diagrams are obtained using the finite difference and "smoothed" finite difference methods when inaccurate strain tensor components are used. The uncertain material properties also likely contributed to the disparity.

Increasing the polynomial order for the "smoothed" finite difference method gives through-thickness strain and stress distributions which are not significantly improved in terms of the general shape and magnitude compared to the DIC software calculations and theoretical solutions, and the increased polynomial order does not much improve the shear force result of the calculations. The shear force diagram using polynomials of order 8 is shown in Figure 6.13. This higher polynomial order allows the method to better capture the behavior at the ends of the beam compared to the DIC and finite difference method calculated shear forces, but the noise is not noticeably reduced compared to the polynomial order 3 shear force diagram previously shown.

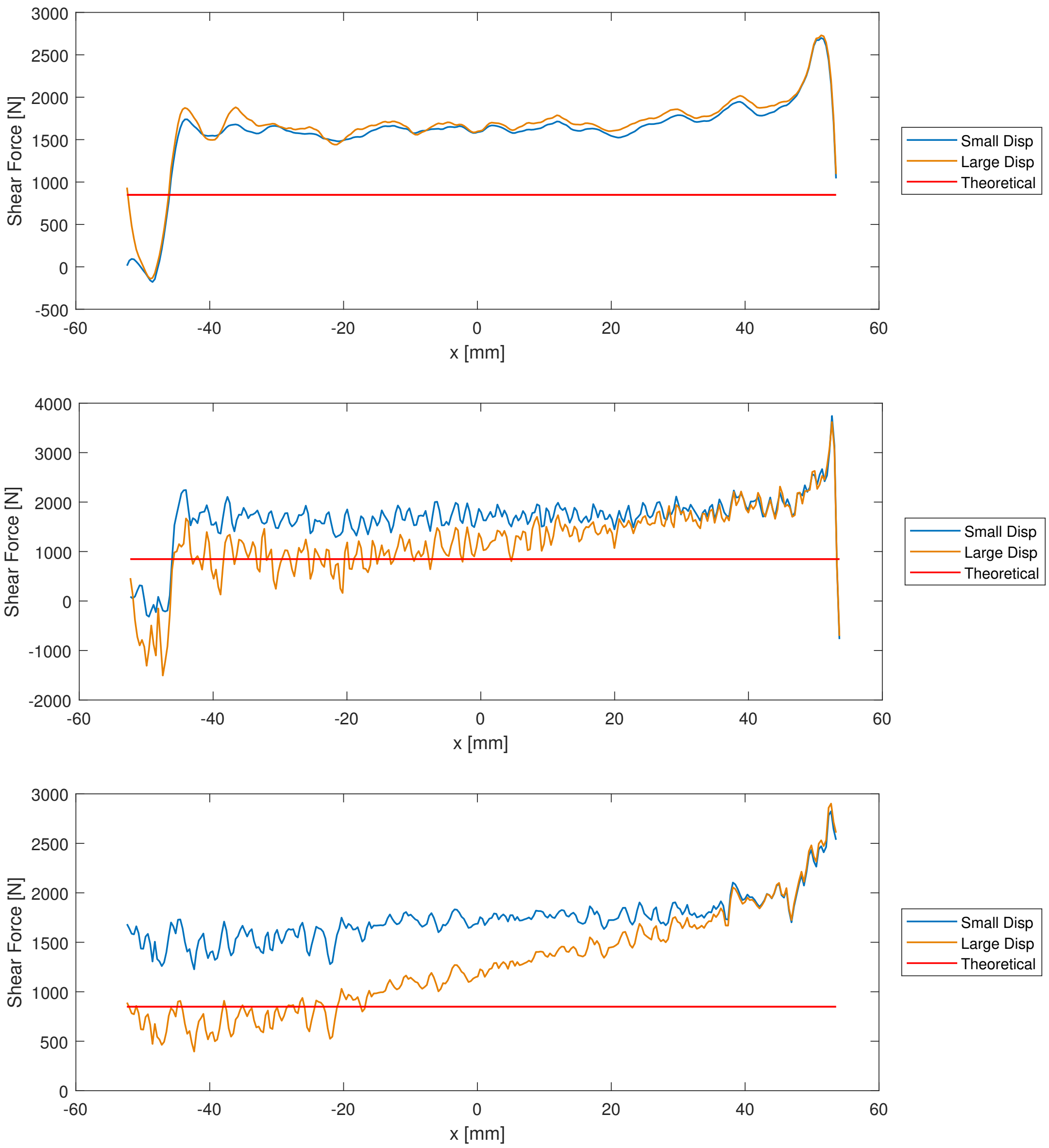

Figure 6.12: Comparison of small and large displacement formulations for the DIC software (top), finite difference method (middle), and "smoothed" finite difference method (bottom) derived pristine beam shear force diagrams

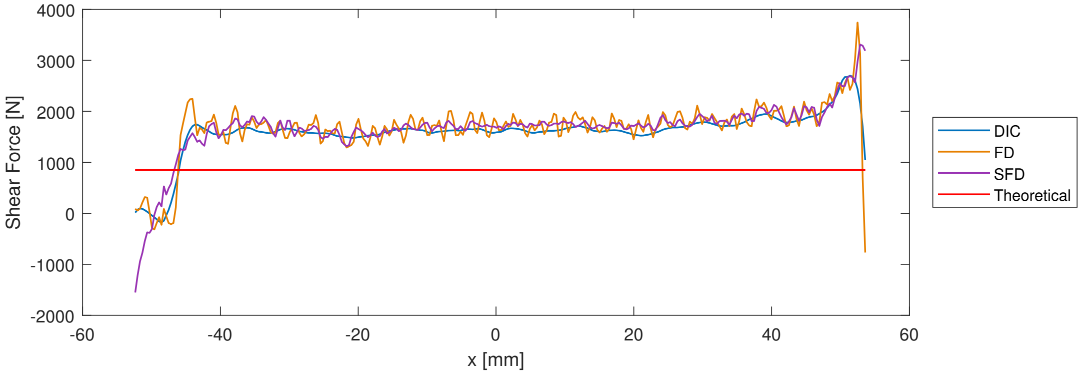

Figure 6.13: Pristine beam shear force diagram using small displacement formulation, and polynomials of order 8 for the "smoothed" finite difference method

This investigation of the approximately 8 mm thick beam through-thickness displacement field shows that the DIC system used for this thesis is not capable of capturing the through-thickness beam behavior for even a pristine beam test, and therefore this data cannot be used to establish a traction-separation law for this thesis. The use of the three different methods for strain calculation, and the relatively similar results from each method indicates that the issue does not lie in the analysis methodology, but rather that the DIC system itself does not provide the accuracy needed represent the through-thickness behavior of the beam. The assumed material properties, and the assumption of a linear elastic constitutive law likely compounded the errors, therefore this investigation also highlights the need for further testing to determine other material properties, and for the use of a more complex material model.

## *6.6 Fracture Test Strain Field*

The theoretical $\gamma_{xz}$ through-thickness distribution for the ELS specimen is shown in Figure 6.14, where when assuming no friction each sublaminate has a parabolic shaped shear strain distribution for the cracked portion of the beam, and for the uncracked portion of the beam the parabolic shaped shear strain distribution spans the entire thickness. For the approximately 8 mm thick and 100 mm long specimen 3, the shear strain field for the cracked

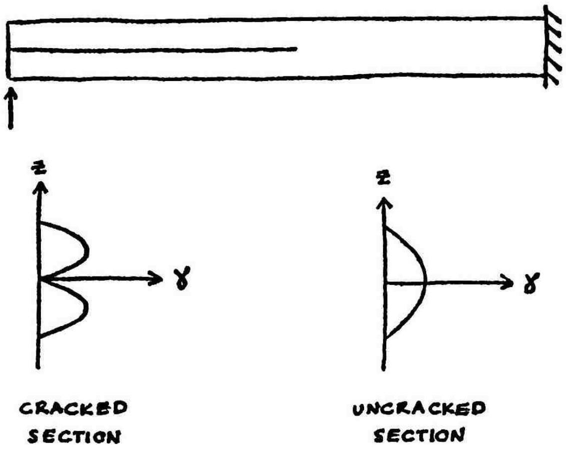

Figure 6.14: Theoretical through-thickness $\gamma_{xz}$ distribution without friction

beam configuration in a loaded state but prior to crack propagation is shown in Figure 6.15, and the shear strain field for the same beam after crack propagation once maximum crack length was attained is shown in Figure 6.16. For the "smoothed" finite difference method polynomials of order 3 were used. These shear strain diagrams show very high magnitude strains, and do not show the expected theoretical result. Despite this, the change in the location of the crack tip is visible in the three-dimensional diagrams, where the cracked portion of the beam exhibits a high magnitude parabolic shaped through-thickness shear strain distribution, and the uncracked portion of the beam has a relatively flat through-thickness shear strain distribution.

## *6.7 Fracture Test Shear Force Diagram*

Using the small displacement formulation to calculate shear stress, and integrating the shear stresses through the thickness gives the shear force diagrams shown in Figure 6.17 for the pre-crack-propagation and post-crack-propagation states. The crack tip is visible in these diagrams where the cracked portion of the beam exhibits high nonconstant magnitude shear forces, and the uncracked portion of the beam exhibits lower and relatively constant magnitude shear forces. This investigation of the through-thickness displacement field data shows

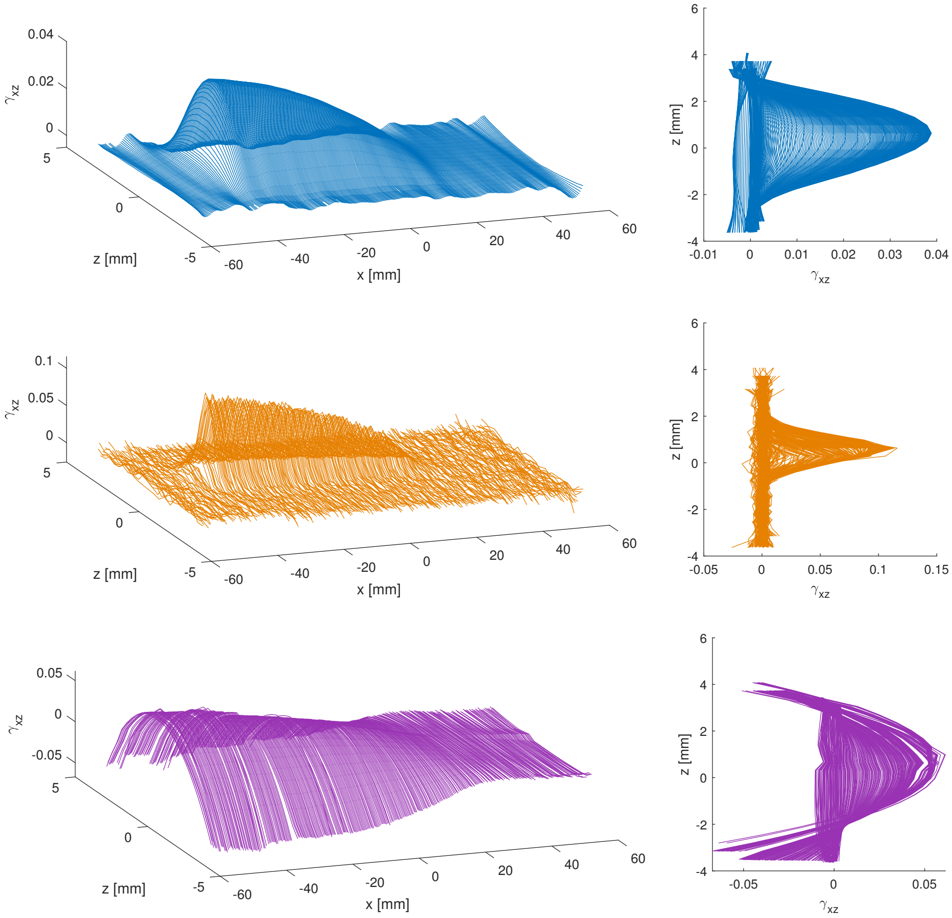

Figure 6.15: Through-thickness $\gamma_{xz}$ field using DIC software (top), finite difference method (middle), and "smoothed" finite difference method (bottom) for a loaded cracked beam configuration prior to crack propagation

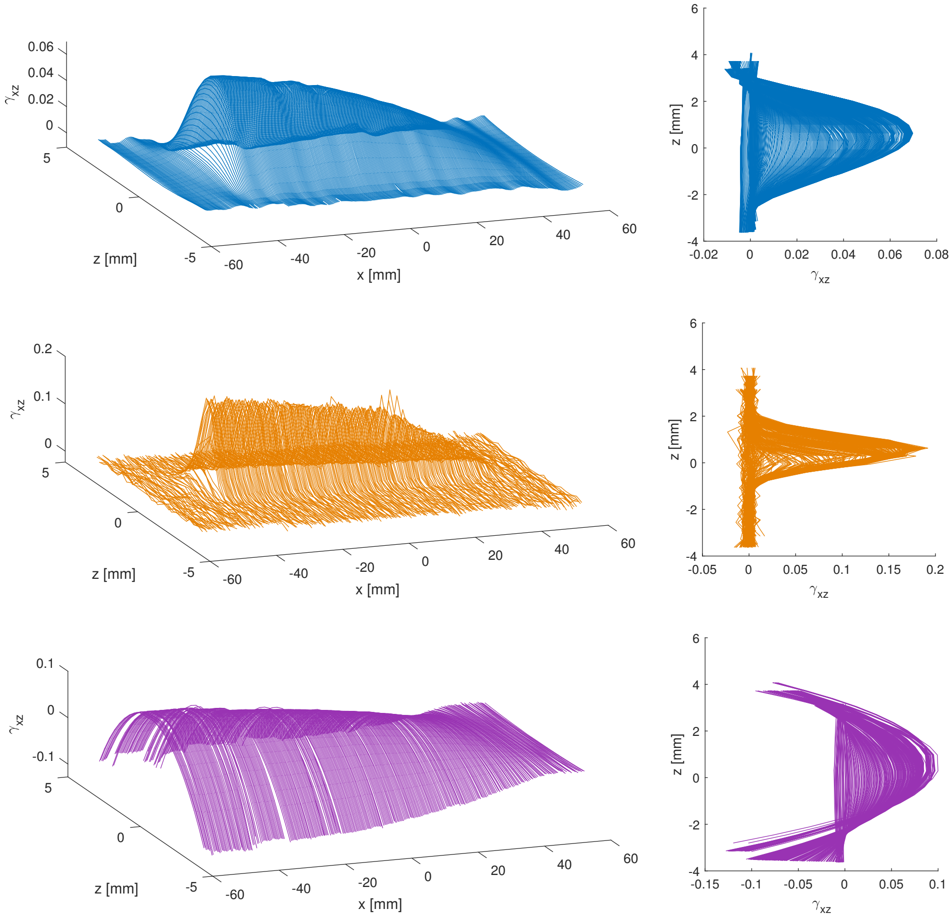

Figure 6.16: Through-thickness $\gamma_{xz}$ field using DIC software (top), finite difference method (middle), and “smoothed” finite difference method (bottom) for a loaded cracked beam configuration after crack propagation at maximum crack length

that the DIC system is not capable of accurately capturing the through-thickness beam behavior for these fracture tests, and hence cannot be used to establish a traction-separation law for this thesis.

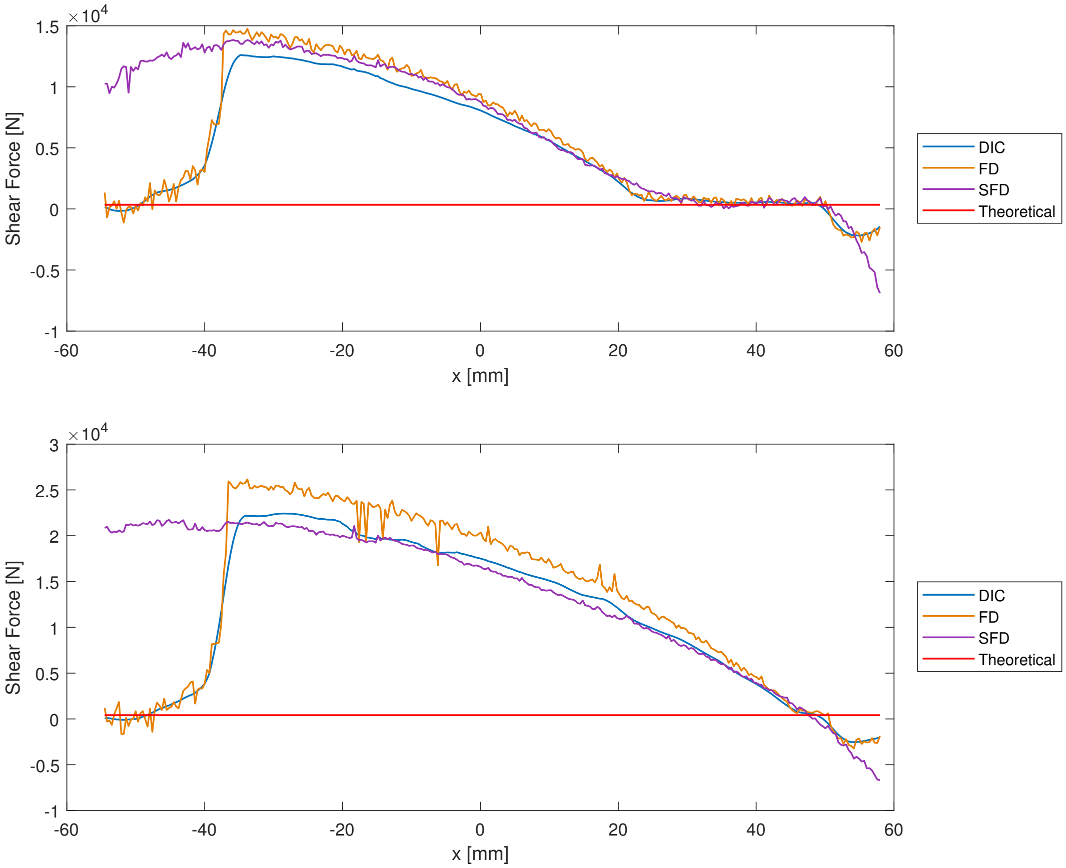

Figure 6.17: Shear diagram for fracture test using small displacement formulation for a loaded cracked beam configuration prior to crack propagation (top), and for a loaded cracked beam configuration after crack propagation at maximum crack length (bottom)

# Chapter 7

# CONCLUSION

## *7.1 Summary of Work*

This thesis investigated mode II delamination behavior in unidirectional composite end loaded split (ELS) specimens through the experimental testing of three different geometry beams, and investigated the capabilities of two different crack growth models. Both pristine and cracked ELS specimens were tested in an Instron load frame which collected the force and displacement data from the load application point, while simultaneously a digital image correlation (DIC) system collected displacement field data of a through-thickness face of the specimens. Euler-Bernoulli beam theory was used to determine the local 1-direction elastic modulus $E_1$ from the pristine beam test, and Griffith's energy approach to fracture was used to determine the mode II critical strain energy release rate $G_{IIC}$. These material properties, and other manufacturer provided or empirically determined material properties, were input into the Abaqus numerical models where delamination propagation was simulated using both the virtual crack closure technique (VCCT), and cohesive zone model (CZM) approaches. The virtual crack closure technique required only elastic material properties to characterize the composite beam behavior in bending, and the critical strain energy release rates to characterize fracture. The cohesive zone model approach required these same properties, as well as the establishment of a traction-separation law to characterize fracture, which included determining not only the critical strain energy release rates, but also the interface strengths and the penalty stiffnesses.

The experimental test and numerical model force-displacement results from the load application point for each of the three different geometry specimens and for each of the two crack growth models showed good agreement when the properties specific to each specimen were used in the numerical model. However, size effects were observed when interchanging properties; this includes interchanging both $E_1$ and $G_{IIC}$ as these were the only two material properties which were determined from the experimental tests, and hence the only properties which varied between specimens. This reveals that, while both the VCCT and CZM methods are capable of accurately capturing beam behavior for mode II delamination, more robust crack growth models are needed to address size effects. Size effects were also observed in the experimentally determined $G_{IIC}$ values themselves, where friction likely affected the calculated values such that higher $G_{IIC}$ values were obtained when the experimental tests had higher friction.

While the traction-separation law used for the CZM Abaqus simulations for this thesis gave force-displacement results which closely matched the experimental test data, this law depended on assumed material properties and behavior. Ideally, the traction-separation law would be determined experimentally by directly observing the traction and crack tip displacements using the through-thickness displacement field data collected by the DIC system. The displacement field analysis results (assuming a linear elastic constitutive law) revealed that the DIC system used for this thesis did not collect accurate enough data to capture the correct through-thickness beam behavior even for a pristine test. The general trends of the calculated strains, stresses, and shear force diagrams matched the theoretical solutions, however the magnitudes were not accurate. The errors in these diagrams were likely also due in part to assumed mechanical material properties. The displacement field data analysis for the fracture test gave insight into the location of the crack tip, however the experimentally obtained strain and shear force diagrams were not accurate and severely overestimated the beam behavior compared to the expected theoretical solution.

## *7.2 Future Work*

The most important item for future work is the improvement of the material model for fracture. The traction-separation law for the Abaqus simulations relied on assumed material properties, with the exception of $G_{IIC}$, and assumed bilinear behavior. Its use produced good results when using the specimen specific $G_{IIC}$ values, however this traction-separation law proved to be ineffective at addressing size effects. Furthermore, attempts to interpret the through-thickness displacement field data yielded no useful results in terms of establishing pristine beam and cracked beam behavior, but specifically for directly determining the traction-separation law for the material. Therefore, a microscopic DIC system should be used to attempt to obtain the data resolution needed to accurately establish beam through-thickness behavior, especially near the crack tip. This approach for determining the traction-separation law will also likely require the use of a more advanced constitutive law, rather than the linear elastic constitutive law used for this thesis. It also may be useful to experimentally determine the interface strengths using ASTM established standard test methods, rather than using manufacturer provided values, as well as a parametric study to determine the shape of the traction-separation law, rather than assuming bilinear behavior. Furthermore, the assumption of negligible friction for the equation used to determine $G_{IIC}$ is inaccurate, as was evident in the size effect investigation of the experimentally obtained $G_{IIC}$ values. Therefore, a more robust theory which includes friction considerations should be used for determining $G_{IIC}$.

The improvement of the determination of the mechanical material properties is less critical than the fracture material model, although not inconsequential. The composite ELS beams used for this thesis were assumed to be transversely isotropic, but only one of the necessary six mechanical material properties required for the numerical modeling (when using Abaqus elements with a plane stress formulation) could be obtained from the experimental test data. While the $E_1$ material property is the most important for ensuring the accuracy of the numerical models, the effects of errors in the other material properties should not be ignored, especially for the through-thickness displacement field data analysis. Ideally, some or all of the other mechanical material properties would be obtained from standardized tests. Furthermore, the determination of mechanical material properties beyond those needed for the plane stress formulation elements in Abaqus should be considered if using solid elements for numerical modeling. Particularly for thicker ELS specimens, the use of solid elements would be useful if finer meshes than those used for this thesis are desired.

A probabilistic study should be done to investigate the effects of compounding errors in specimen parameters on the experimental results. This study would be used to create confidence intervals for experimental results such as the $G_{IIC}$ values, and the through-thickness displacement field analysis results. The specimen parameters to investigate could include the layup orientations (all plies were assumed to have exactly 0° orientation); the specimen thickness, length, and width; the crack length; and the mechanical material properties.

As was mentioned in Chapter 4, the material properties obtained from the experimental tests done for this thesis were lower than the manufacturer provided material properties. The disparity could be caused by the aging of the composite, the storage conditions, the fabrication and curing process, or a combination of these factors. An investigation into the effects of composite degradation could produce useful insights regarding this finding.

As was mentioned in Chapter 2, the ELS specimen was chosen in part due to the prospect of experimental testing in a CT scanner due to its longer unobstructed span for observing crack front advance compared to the ENF specimen. Lin [2017] reported that the fixtures used for the ENF specimen introduced signal noise to, and limited the resolution of the scans. The research results from this thesis show that the ELS specimen is a viable alternative to the ENF specimen for characterizing mode II delamination behavior, therefore the ELS specimen could be used in conjunction with the CT scanner to further characterize mode II delamination in terms of determining through-width crack front advance.

# REFERENCES

Abaqus (2014). *Version 6.14 Documentation.* Dassault Systèmes, Providence, Rhode Island.

ASTM (2014). *Standard Test Method for Determination of the Mode II Interlaminar Fracture Toughness of Unidirectional Fiber-Reinforced Polymer Matrix Composites.*

ASTM (2015). *Standard Test Method for Flexural Properties of Polymer Matrix Composite Materials.*

ASTM (2016). *Standard Test Method for Short–Beam Strength of Polymer Matrix Composite Materials and Their Laminates.*

Bisagni, C., Brambilla, P., and Dávila, C. G. (2013). "Modeling delamination in postbuckled composite structures under static and fatigue loads." *Conference Paper: SAPME at Long Beach, CA.*

Blackman, B., Brunner, A., and Williams, J. (2006). "Mode II fracture testing of composites: a new look at an old problem." *Engineering Fracture Mechanics*, 73(16), 2443–2455.

Brunner, A., Blackman, B., and Davies, P. (2008). "A status report on delamination resistance testing of polymer–matrix composites." *Engineering Fracture Mechanics*, 75(9), 2779–2794.

Correlated Solutions (2016). *Vic-3D v7 Testing Guide.*

Costa, M. L., De Almeida, S. F. M., and Rezende, M. C. (2001). "The influence of porosity on the interlaminar shear strength of carbon/epoxy and carbon/bismaleimide fabric laminates." *Composites Science and Technology*, 61(14), 2101–2108.

Davies, P., Blackman, B., and Brunner, A. (2001). "Mode II delamination." *European Structural Integrity Society*, Vol. 28, Elsevier, 307–333.

Griffith, A. (1920). "The phenomena of rupture and flow in solids." *Philosophical Transactions of the Royal Society*, 221, 163–198.

Inglis, C. (1913). "Stresses in a plate due to the presence of cracks and sharp corners." *Transactions of the Institute of Naval Architects*, 60, 219–241.

Irwin, G. (1948). "Fracture dynamics." *Fracturing of Metals*, 146–166.

Kollar, L. P. and Springer, G. S. (2003). *Mechanics of Composite Structures*. Cambridge University Press.

Krueger, R. (2004). "Virtual crack closure technique: history, approach, and applications." *Applied Mechanics Reviews*, 57(2), 109–143.

Lin, C.-P. (2017). "Delamination growth in carbon fiber beams: Numerical and experimental study using computed tomography." M.S. thesis, University of Washington, Civil and Environmental Engineering, More Hall, Seattle, WA 98195.

Mamidala, R. (2018). "Lecture notes in introduction to fracture mechanics." *University of Washington*, Department of Mechanical Engineering.

Motley, M. (2018). "Lecture notes in finite elements for structural mechanics." *University of Washington*, Department of Civil and Environmental Engineering.

Orowan, E. (1949). "Fracture and strength of solids." *Report of Progress in Physics*, 12(185), 185–232.

Rice, J. (1968). "A path independent integral and the approximate analysis of strain concentration by notches and cracks." *Journal of Applied Mechanics*, 35, 379–386.

Sanford, R. (2003). *Principles of Fracture Mechanics.* Pearson Education, Upper Saddle River, New Jersey.

Song, K., Dávila, C. G., and Rose, C. A. (2008). “Guidelines and parameter selection for the simulation of progressive delamination.” *Abaqus Users' Conference.*

Tay, T. (2003). “Characterization and analysis of delamination fracture in composites: An overview of developments from 1990 to 2001.” *Applied Mechanics Reviews*, 56(1), 1–32.

Toray Composites America, Inc. (2018a). *2510 Prepreg System.*

Toray Composites America, Inc. (2018b). *T700G Data Sheet.*

Tsenoglou, C. J., Pavlidou, S., and Papaspyrides, C. D. (2006). “Evaluation of interfacial relaxation due to water absorption in fiber–polymer composites.” *Composites Science and Technology*, 66(15), 2855–2864.

Turon, A., Davila, C. G., Camanho, P. P., and Costa, J. (2007). “An engineering solution for mesh size effects in the simulation of delamination using cohesive zone models.” *Engineering Fracture Mechanics*, 74(10), 1665–1682.

Westergaard, H. (1939). “Bearing pressures and cracks.” *Journal of Applied Mechanics*, 6, A49–A53.

Williams, J. (1988). “On the calculation of energy release rates for cracked laminates.” *International Journal of Fracture*, 36(2), 101–119.

Yang, J. (2018). “Lecture notes in mechanics of composite materials.” *University of Washington*, Department of Aeronautics and Astronautics.

Zhu, J., Imam, A., Crane, R., Lozano, K., Khabashesku, V. N., and Barrera, E. V. (2007). “Processing a glass fiber reinforced vinyl ester composite with nanotube enhancement of interlaminar shear strength.” *Composites Science and Technology*, 67(7-8), 1509–1517.

# Appendix A

## COMPLIANCE OF THE ELS SPECIMEN

Consider the beam, as well as its associated shear and moment distributions, shown in Figure A.1. To determine the compliance of this beam, solve the following differential equation and boundary condition set by considering the cracked (section C) and uncracked (section U) portions of the beam separately:

$$\begin{aligned} M(x) &= EI_C v_C''(x), & v_U(L) &= 0, & v_C(a) &= v_U(a) \\ M(x) &= EI_U v_U''(x), & v_U'(L) &= 0, & v_C'(a) &= v_U'(a). \end{aligned}$$

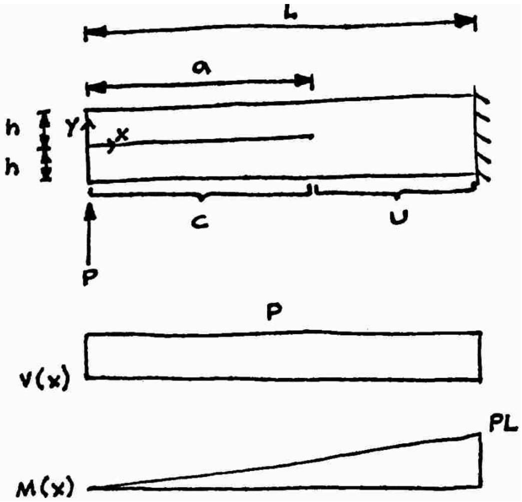

Figure A.1: End loaded split specimen, shear, and moment diagrams

The cracked and uncracked sections of the beam have moments of inertia

$$I_C \;=\; 2\frac{Bh^3}{12} \;=\; 2I \qquad\qquad \text{and} \qquad\qquad I_U \;=\; \frac{B(2h)^3}{12} \;=\; 8I.$$

Plugging the moment $M(x)$, and the moments of inertia $I_C$ and $I_U$ into the differential equations and integrating twice gives

$$\begin{aligned} v_C(x) &= \frac{P}{12EI}x^3 + c_1 x + c_2, \\ v_U(x) &= \frac{P}{48EI}x^3 + c_3 x + c_4, \end{aligned}$$

and applying the boundary conditions gives the unknown constants of integration

$$\begin{aligned} c_1 &= -\frac{3Pa^2 + PL^2}{16EI}, & \qquad c_2 &= \frac{3Pa^3 + PL^3}{24EI}, \\ c_3 &= -\frac{PL^2}{16EI}, & \qquad c_4 &= \frac{PL^3}{24EI}. \end{aligned}$$

The compliance $C$ of the beam is defined such that the relationship between vertical displacement $v$ and applied load $P$ at the free end of the beam is given by

$$v = PC,$$

and therefore the compliance of the end loaded split beam can be found by solving

$$v \;=\; v_C(0) \;=\; c_2 \;=\; \frac{3Pa^3 + PL^3}{24EI} \;=\; P\left(\frac{3a^3 + L^3}{24EI}\right),$$

and hence,

$$C = \frac{3a^3 + L^3}{24EI}.$$

# Appendix B

# CLOSED-FORM FORCE-DISPLACEMENT SOLUTION FOR THE ELS SPECIMEN

To obtain a closed-form solution for the force-displacement response of the end loaded split specimen, three loading stages must be considered: (1) the initial loading stage where the crack has not yet begun growing, (2) the crack propagation stage and (3) the completely split beam stage where the crack length and the beam length are the same.

The force-displacement relationship for the initial loading stage is given by (see Appendix A)

$$v = P\left(\frac{3a_0^3 + L^3}{24EI}\right). \tag{B.1}$$

During the crack propagation stage the crack length is increasing but the strain energy release rate remains constant at the critical value (see Section 1.5.5 for crack growth conditions). For the end loaded split specimen the strain energy release rate is given by (see Section 1.5.1)

$$G_{II} = \frac{9P^2a^2}{4EB^2h^3} \tag{B.2}$$

and the force-displacement relationship is given by (see Appendix A)

$$v = P\left(\frac{3a^3 + L^3}{24EI}\right). \tag{B.3}$$

Therefore the force-displacement relationship for the crack propagation stage is solved by rearranging equation (B.2) for $a$, and substituting into equation (B.3), and hence is given by

$$v = \frac{P}{24EI}\left[3\left(\frac{16BEIG_{IIC}}{3P^2}\right)^{\frac{3}{2}} + L^3\right]. \tag{B.4}$$

When the crack has grown to the fixed end of the beam, the completely split beam force-displacement relationship is solved by considering two identical beams stacked on top of one another without shear transfer (assuming no friction). The force-displacement relationship for a cantilever beam is given by

$$v = P\left(\frac{L^3}{3EI^*}\right)$$

where in the case of the completely split beam

$$I^* = 2\left(\frac{Bh^3}{12}\right) = 2I.$$

Therefore the force-displacement relationship for the completely split beam stage is given by

$$v = P\left(\frac{L^3}{6EI}\right). \tag{B.5}$$

## Appendix C

# TWO-DIMENSIONAL ELASTICITY AND THE AIRY STRESS FUNCTIONS

The Airy stress function is defined by

$$\begin{aligned} \sigma_x &= \frac{\partial^2 \Phi}{\partial y^2}, \\ \sigma_y &= \frac{\partial^2 \Phi}{\partial x^2}, \\ \tau_{xy} &= -\frac{\partial^2 \Phi}{\partial x \partial y}. \end{aligned}$$

These stress definitions satisfy equilibrium in two dimensions under the plane stress condition as follows

$$\begin{aligned} \Sigma F_x &= \frac{\partial \sigma_x}{\partial x} + \frac{\partial \tau_{xy}}{\partial y} = \frac{\partial^3 \Phi}{\partial y^2 \partial x} + \left( -\frac{\partial^3 \Phi}{\partial x \partial y \partial y} \right) = 0, \\ \Sigma F_y &= \frac{\partial \sigma_y}{\partial y} + \frac{\partial \tau_{xy}}{\partial x} = \frac{\partial^3 \Phi}{\partial x^2 \partial y} + \left( -\frac{\partial^3 \Phi}{\partial x \partial y \partial x} \right) = 0. \end{aligned}$$

The strain-displacement relations are

$$\begin{aligned} \varepsilon_x &= \frac{\partial u}{\partial x}, \\ \varepsilon_y &= \frac{\partial v}{\partial y}, \\ \gamma_{xy} &= 2\varepsilon_{xy} = \frac{\partial u}{\partial y} + \frac{\partial v}{\partial x} \end{aligned}$$

where $u$ is displacement in the $x$-direction and $v$ is displacement in the $y$-direction. From these strain-displacement relations, compatibility in two dimensions is

$$2\frac{\partial^2 \varepsilon_{xy}}{\partial x \partial y} = \frac{\partial^2 \varepsilon_x}{\partial y^2} + \frac{\partial^2 \varepsilon_y}{\partial x^2}. \tag{C.1}$$

The three-dimensional linear elastic constitutive laws simplified for two dimensions and the plane stress condition are given by

$$\varepsilon_x = \frac{\sigma_x}{E} - \frac{\nu \sigma_y}{E}, \tag{C.2}$$

$$\varepsilon_y = -\frac{\nu \sigma_x}{E} + \frac{\sigma_y}{E}, \tag{C.3}$$

$$\varepsilon_{xy} = \frac{\tau_{xy}}{2\mu} \tag{C.4}$$

where $\nu$ is Poisson's ratio, $E$ is Young's modulus, and $\mu$ is the shear modulus.

Now that equilibrium, constitutive laws, and compatibility have been defined, the governing equation can be established. Differentiating twice with respect to $y$ of equation (C.2), differentiating twice with respect to $x$ of equation (C.3), differentiating with respect to $x$ and $y$ of equation (C.4), and plugging them into equation (C.1) gives

$$\frac{1}{\mu}\frac{\partial^2 \tau_{xy}}{\partial x \partial y} = \frac{1}{E}\frac{\partial^2 \sigma_x}{\partial y^2} - \frac{\nu}{E}\frac{\partial^2 \sigma_y}{\partial y^2} - \frac{\nu}{E}\frac{\partial^2 \sigma_x}{\partial x^2} + \frac{1}{E}\frac{\partial^2 \sigma_y}{\partial x^2}. \tag{C.5}$$

Recall the equilibrium equations from above, and differentiate once with respect to $x$ of equilibrium in the $x$-direction, differentiate once with respect to $y$ of equilibrium in the $y$-direction, and combine the equations to develop an expression for $\tau_{xy}$ in terms of $\sigma_x$ and $\sigma_y$, given by

$$\frac{\partial^2 \tau_{xy}}{\partial x \partial y} = -\frac{1}{2}\left(\frac{\partial^2 \sigma_x}{\partial x^2} + \frac{\partial^2 \sigma_y}{\partial y^2}\right). \tag{C.6}$$

Substituting equation (C.6) into equation (C.5) and recalling that $E = 2\mu(1+\nu)$ for an isotropic material gives

$$\frac{\partial^2 \sigma_x}{\partial x^2} + \frac{\partial^2 \sigma_x}{\partial y^2} + \frac{\partial^2 \sigma_y}{\partial x^2} + \frac{\partial^2 \sigma_y}{\partial y^2} = 0, \tag{C.7}$$

$$\nabla^2(\sigma_x + \sigma_y) = 0. \tag{C.8}$$

Substituting the Airy stress function definitions into equation (C.8) gives the governing equation

$$\nabla^2(\sigma_x + \sigma_y) = \nabla^2\left(\frac{\partial^2 \Phi}{\partial y^2} + \frac{\partial^2 \Phi}{\partial x^2}\right) = \nabla^2(\nabla^2 \Phi) = \nabla^4 \Phi = 0.$$

The Airy stress function satisfies both equilibrium and compatibility and is biharmonic.

# Appendix D

## PATH INDEPENDENCE OF THE J-INTEGRAL

To prove that $J$ is path independent, consider any closed curve $\Gamma^*$ which encloses the area $A^*$. To relate $\Gamma^*$ to $A^*$ consider Green's theorem

$$\oint_{\Gamma^*} P(x,y)dx + Q(x,y)dy \;=\; \iint_{A^*} \left(\frac{\partial Q}{\partial x} - \frac{\partial P}{\partial y}\right) dxdy.$$

The $Q(x,y)dy$ term in the line integral relates directly to $Wdy$ in equation (1.13), therefore $\partial Q/\partial x$ in the surface integral is $\partial W/\partial x$. The infinitesimal strain is

$$\varepsilon_{ij} = \frac{1}{2}\left(\frac{\partial u_i}{\partial x_j} + \frac{\partial u_j}{\partial x_i}\right).$$

Expansion of $\partial W/\partial x$ using the chain rule, the definition of $\varepsilon_{ij}$, and symmetry ($\varepsilon_{ij} = \varepsilon_{ji}$) gives

$$\frac{\partial W}{\partial x} \;=\; \frac{\partial W}{\partial \varepsilon_{ij}}\frac{\partial \varepsilon_{ij}}{\partial x} \;=\; \sigma_{ij}\frac{\partial^2 u_i}{\partial x_j \partial x} \;=\; \frac{\partial}{\partial x_j}\left(\sigma_{ij}\frac{\partial u_i}{\partial x}\right). \tag{D.1}$$

The $P$ terms in Green's theorem requires use of the divergence theorem

$$\iiint_V \nabla \cdot \mathbf{v} dV \;=\; \oint\!\!\oint_A \mathbf{v} \cdot \mathbf{n} dA.$$

The other term in equation (1.13) can be written as

$$\mathbf{T} \cdot \frac{\partial \mathbf{u}}{\partial x} \;=\; (u_{i,1}\mathbf{e_i}) \cdot (\sigma_{jk}\mathbf{e_j} \otimes \mathbf{e_k}) \cdot (n_l \mathbf{e_l}) \;=\; (u_{i,1}\sigma_{ik}\mathbf{e_k}) \cdot (n_l \mathbf{e_l}),$$

and using the divergence theorem

$$\begin{aligned} \oint_{\Gamma^*} \mathbf{T}\cdot\frac{\partial \mathbf{u}}{\partial x}ds \;&=\; \oint_{\Gamma^*} (u_{i,1}\sigma_{ij}\mathbf{e_j})\cdot\mathbf{n}ds \\ = \iint_{A^*} \nabla\cdot(u_{i,1}\sigma_{ij}\mathbf{e_j})dxdy \;&=\; \iint_{A^*} \frac{\partial}{\partial x_j}\left(\sigma_{ij}\frac{\partial u_i}{\partial x}\right)dxdy. \end{aligned} \tag{D.2}$$

Plugging the relations found in equations (D.1) and (D.2) into Green's theorem gives

$$\oint_{\Gamma^*}\left(Wdy - T_i\frac{\partial u_i}{\partial x}ds\right) \;=\; \iint_{A^*}\left[\frac{\partial}{\partial x_j}\left(\sigma_{ij}\frac{\partial u_i}{\partial x}\right) - \frac{\partial}{\partial x_j}\left(\sigma_{ij}\frac{\partial u_i}{\partial x}\right)\right]dxdy \;=\; 0,$$

and therefore, $J$ is equal to 0 for any closed curve.

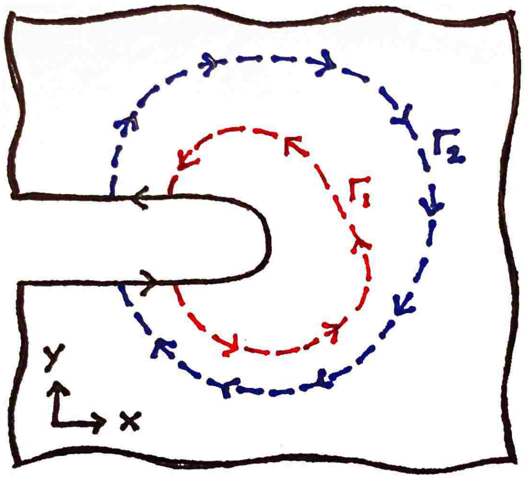

Figure D.1: Closed curve composed of $\Gamma_1$, $\Gamma_2$, and two segments of the flat surfaced notch

Consider any two paths surrounding a notch tip as in Figure D.1 where $\Gamma_1$, $\Gamma_2$, and the two segments of the flat surfaced notch form a closed curve. As proved earlier, the integral of $Wdy - \mathbf{T}\cdot(\partial\mathbf{u}/\partial x)$ on this closed curve is 0. Noting that for the surfaces of the notch $\mathbf{T}$ is 0 and $dy$ is 0, the counterclockwise integral along $\Gamma_1$ and the clockwise integral along $\Gamma_2$ must sum to zero, and therefore $J$ is path independent.

## Appendix E

# ADDITIONAL THROUGH-THICKNESS DISPLACEMENT FIELD ANALYSIS RESULTS

Additional pristine beam through-thickness displacement field analysis results are presented in this appendix to serve as a comparison to the results shown in Chapter 6. The shear force diagrams obtained from the through-thickness displacement field data for the approximately 8 mm thick, 100 mm long specimen 3 appeared to differ in magnitude from the theoretical shear force diagram obtained from the known load applied to the specimen by a factor of 2. This is suspicious due to the factor of 2 relating $\varepsilon_{xz}$ and $\gamma_{xz}$. The same analysis procedure outlined in Section 6.2 was used for all five ELS specimens tested for this thesis, using the small displacement assumption, polynomials of order 3 for the "smoothed" finite difference method, and the geometric and material parameters specific to each specimen. The shear force diagrams for the two 8 mm thick, 100 mm long specimens are shown in Figure E.1; the 4 mm thick, 100 mm long specimen is shown in Figure E.2; and the two 4 mm thick, 50 mm long specimens are shown in Figure E.3.

There are several observations that can be made from these pristine beam shear force diagrams. The first is that, despite the varying levels of noise depending on the strain calculation method, the shear force diagrams for all three strain calculation methods yield similar results and exhibit relatively flat, linear shapes which matches the theoretical shape for the shear force diagram of a cantilever beam, however the magnitudes do not match. Some of the shear force diagrams more closely match the expected theoretical result, however there does not appear to be any pattern with regard to which specimens had better or worse results. The factor of 2 for the 8 mm thick, 100 mm long specimen 3 seems to be a coincidence, as the factors for all other specimens are different from this specimen and from each other.

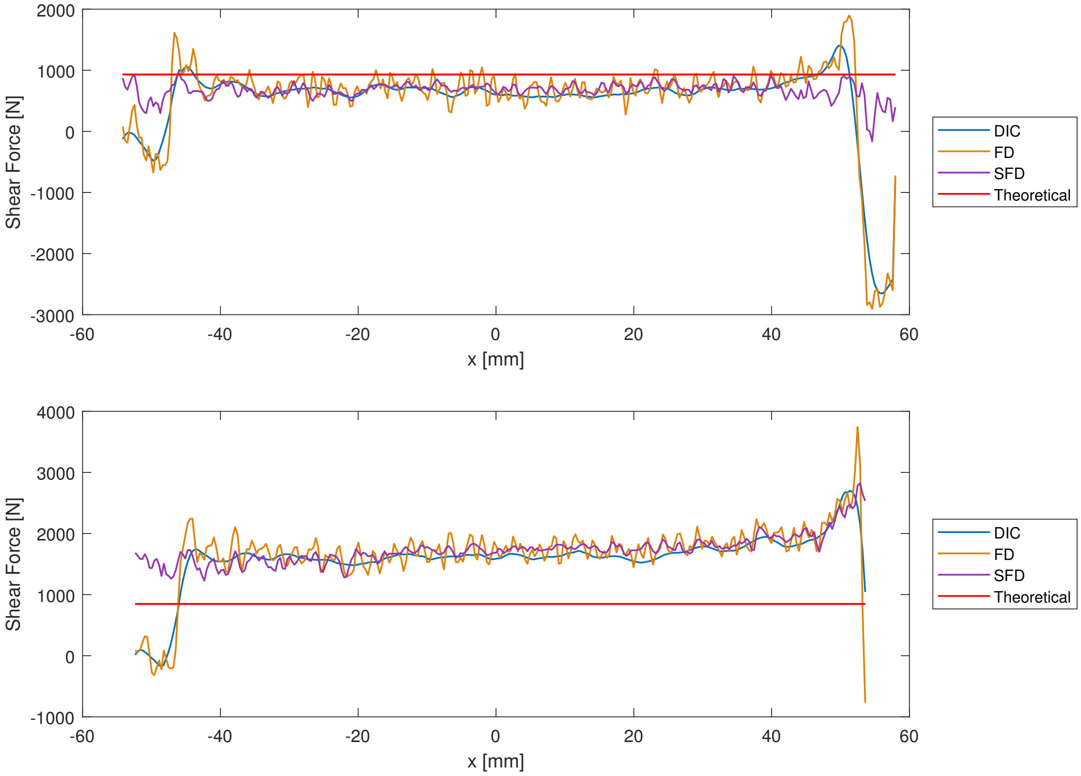

Figure E.1: Pristine beam shear force diagram using small displacement formulation for the 8 mm thick, 100 mm long ELS specimen 2 (top), and specimen 3 (bottom)

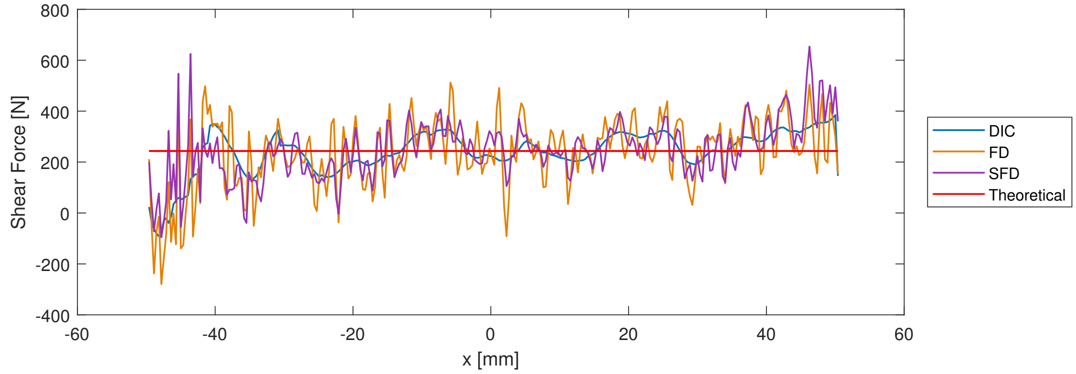

Figure E.2: Pristine beam shear force diagram using small displacement formulation for the 4 mm thick, 100 mm long ELS specimen 6

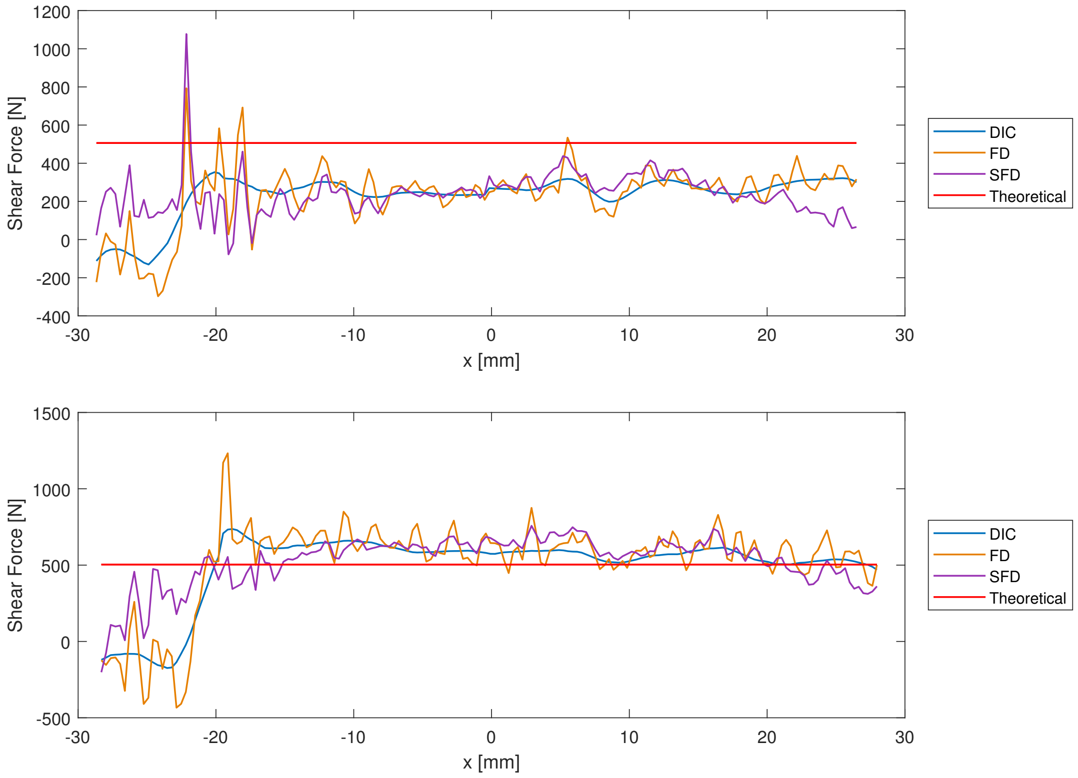

Figure E.3: Pristine beam shear force diagram using small displacement formulation for the 4 mm thick, 50 mm long ELS specimen 1 (top), and specimen 3 (bottom)

Furthermore, there does not seem to be a pattern as far as whether the through-thickness displacement field data yields shear force diagrams which overestimate or underestimate beam behavior. The portions of the beam which extend past the load application point and the fixed end are also visible in these figures.

This additional investigation into the through-thickness displacement field results conclusively determines that the errors in these results are not due to the analysis methodology since the three strain calculation methods show good agreement to each other, but rather that the DIC system itself is not capable of accurately capturing uncracked beam behavior for the specimen geometries used for this thesis. The errors in these results could be due to the quality of the beam speckle, an accidental adjustment to the positions of the DIC cameras and lights during testing, or a combination of these and other factors. The errors are likely also due in part to the assumed value for $G_{12}$, however the lack of any consistent overestimation or underestimation of beam behavior implies that this is not a primary influence on the error.